BULK SILICON-GERMANIUM HETEROJUNCTION BIPOLAR TRANSISTOR PROCESS FEATURE IMPLICATIONS FOR SINGLE-EVENT EFFECTS ANALYSIS AND CHARGE COLLECTION MECHANISMS

By

Jonathan Allen Pellish

Dissertation

Submitted to the Faculty of the

Graduate School of Vanderbilt University

in partial fulfillment of the requirements

for the degree of

DOCTOR OF PHILOSOPHY

in

Electrical Engineering

December, 2008

Nashville, Tennessee

Approved:

Professor Robert A. Weller

Professor Daniel M. Fleetwood

Professor Ronald D. Schrimpf

Professor Paul D. Sheldon

Professor Robert A. Reed

ACKNOWLEDGEMENTS

I would like to thank my committee for their support and encouragement throughout my graduate school career. They provided invaluable feedback, a wonderful perspective on the radiation effects community, and showed by example what it means to have scientific integrity. I owe a special debt to my advisors Bob Weller and Robert Reed for their time and guidance. I look forward to working with them in the coming years. Finally, would like to acknowledge the support of my family, my friends in the RER Group, and the 1106 Fatherland ST crew – you all made life and those late nights in the lab bearable and that much sweeter.

This work was supported in part by the NASA Goddard Space Flight Center under the NASA Electronic Parts and Packaging program, the Defense Threat Reduction Agency under the Radiation Hardened Microelectronics Program, the AFOSR Multidisciplinary Research Program of the University Research Initiative, an AFOSR Defense University Research Instrumentation Program grant, the NASA Radiation Hardened Electronics for Extreme Environments ETDP program, Sandia National Laboratories, the Naval Research Lab, and the Georgia Electronic Design Center at the Georgia Institute of Technology. I am grateful to K. LaBel, L. Cohn, and the SiGe teams at NASA, IBM, Jazz Semiconductor, BAE Systems, and National Semiconductor for their contributions.

Per aspera ad Astra

through hardships to the stars

TABLE OF CONTENTS

Page

LIST OF TABLES

Table Page

LIST OF FIGURES

CHAPTER I

INTRODUCTION

Overview

Since 1995, when IBM's commercial silicon-germanium (SiGe) BiCMOS process emerged at the Bipolar/BiCMOS Circuits and Technology Meeting [NHM+95, AFS+97], SiGe-based technology has been recognized for its potential to transform high-speed microelectronic applications by monolithic incorporation of low power CMOS logic with high-speed SiGe HBT building blocks. This BiCMOS approach reaps the benefits of standard silicon fabrication processes: low cost, large-scale integration, and high yield [Cre98, CN03, Cre05, Cre06a, Cre07]. As the costs of circuit development and deployment increase, the satellite industry stands to benefit both financially and technologically from the insertion of more COTS and ASIC parts built using SiGe BiCMOS processes where high-bandwidth data handling and low-bandwidth data processing requirements coexist.

Radiation effects engineers and physicists face three particle-induced threats when deploying microelectronic applications in the space environment: total ionizing dose (TID), displacement damage, and single-event effects (SEEs) [Bar05, Sum92, Dod99, SF04][1]. Studies have shown that SiGe heterojunction bipolar transistors (HBTs) are tolerant to both TID [BCV+95, VLT99, CHM+00, SHL+04, SGJ+06] and displacement damage effects [RAC+97, ZNC+99, Cre05, HML+05]. Though TID and displacement

[1]These points refer specifically to electrical system repercussions, neglecting other areas such as mechanical and thermal.

damage are important effects for long term space missions, due to the SiGe HBTs' inherent tolerance and the prevailing low dose rates throughout most of interplanetary space, they are second-order concerns for SiGe HBTs relative to SEEs like single-event upset (SEU).

The first ground-based broadbeam heavy ion single-event testing on high-speed SiGe HBT hardware was conducted in 1999 and 2000; it was reported by P. W. Marshall, *et al.* [MCC+00]. This work showed that high-speed SiGe HBT serial shift registers exhibited SEU sensitivity and that the SEU sensitivity increased at higher clock speeds. These trends were expected based on previous experience with GaAs technologies and other silicon logic families such as emitter coupled logic (ECL) [BKK+93, MDW+95, MWB+96, MWK+96, RCM+96, CMM+97]. Circuits fabricated in SiGe HBT processes not only show low threshold SEU sensitivity, but they also exhibit large event cross sections for highly ionizing particles. These event cross sections can be more than an order of magnitude larger than the active region of a single device in some cases [MCC+00, RMP+03, MCC+05, HCJ+06, KMN+06].

SiGe HBTs exhibit a low SEU threshold and a high saturated cross section, but these are not unique characteristics in the trade space of commercial technologies, most commercial technologies share these traits. However, the single-event response and contributing single-event upset mechanisms of SiGe HBTs are unique. The charge collection mechanisms and response, as well as the shape of the single-event cross section data, could be explained by neither classical charge collection processes [HMO81a, HMO81b, Hu82, HMO83, Dod96, Dod99] nor the traditional integrated rectangular parallelepiped (IRPP) and effective flux models [Bin88, PPAS92, Pet95,

PPM$^+$05]. Leveraging the benefits of SiGe HBTs in space applications requires new rate prediction techniques and examination of the dominant underlying charge collection processes driving the single-event response. This work describes how these goals were accomplished through both experiment and simulation.

Technology Description

SiGe HBTs are a vertical bipolar device technology. Recent processing advances have enabled silicon-on-insulator (SOI) SiGe HBTs, more advanced lateral devices, and pnp transistors, but the majority of technologies are vertical npn processes for bulk substrates [Cre06a]. The cross section of a first-generation bulk npn SiGe HBT is shown in Fig. 1. From a radiation effects perspective, the three critical features are the lightly doped p-type substrate, the n^+ subcollector, and the deep trench isolation. The devices examined in this work are identical to the SiGe HBT pictured in Fig. 1.

SiGe HBT technology generations can be classified by their minimum feature size, but this is tantamount to organizing them by their intrinsic speed characteristics, f_T and f_{max}, which are more descriptive characteristics. Fig. 2 shows a scatter plot of SiGe HBT maximum oscillation frequency as a function of the unity gain cutoff frequency [Cre05, Cre07]. The four current technology generations tend to fall along the $f_{max} = f_T$ line. Third generation SiGe HBT technologies, like IBM's 8HP [JKP$^+$02], are in commercial production and widely available. However, this work focuses on first generation technologies, specifically IBM's 5AM SiGe HBT. While there are lateral and vertical scaling differences between the first and third generations, particularly in the

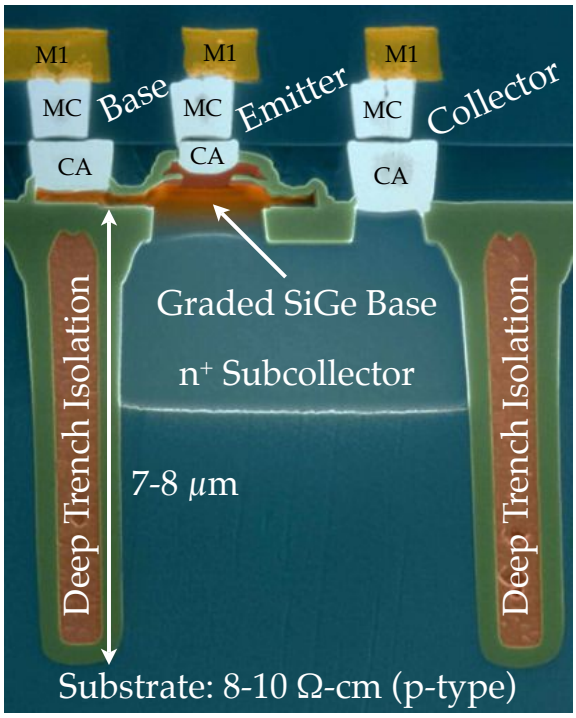

Fig. 1: Physical cross section of a first-generation IBM vertical npn SiGe HBT, fabricated in the 5HP process – with permission. The relevant features of the device are labeled. For radiation effects, the dominant features are the n^+ subcollector, the lightly doped p-type substrate, and the deep trench isolation. Courtesy of International Business Machines Corporation. Unauthorized use not permitted.

graded germanium profile in the base, the dominant charge collection mechanisms and single-event response for bulk processes are similar.

Figs. 3, 4, and 5 show typical DC and AC device characteristics for an IBM 5AM SiGe HBT with an emitter area (A_E) of 0.5×2.5 μm^2. The collector current, and thus the current gain of SiGe HBTs, is dominated by the concentration and location of germanium in the active region of the device. The presence of germanium in the base will enhance the collector current density (J_C) at a fixed V_{BE} regardless of the shape of the profile. The J_C enhancement depends exponentially on the emitter-base boundary value of germanium-induced band offset, and linearly on the germanium grading across the

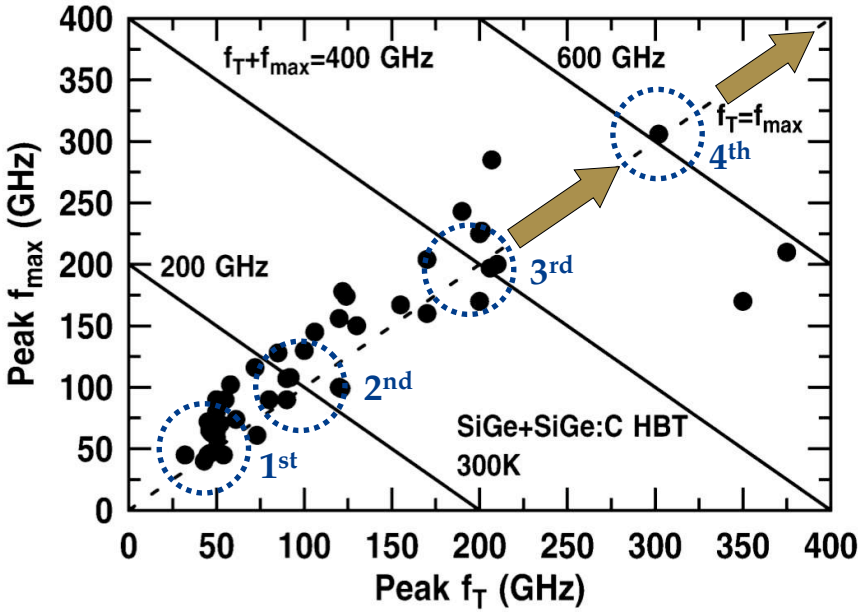

Fig. 2: $f_{\max}$ and f_t trends for the first four generations of SiGe HBT process technologies. The data tend to fall on the $f_{\max} = f_t$ line [Cre05, Cre07].

base. J_C enhancement, induced by germanium, also depends on reciprocal temperature, such that the enhancement effects are magnified at low temperature [Cre06a].

The high injection forced I_B characteristics, shown in Fig. 4, reveal a large Early voltage [PS91], which is characteristic of SiGe HBTs since both the current gain and Early voltage are decoupled from the base Ge-profile and can be tuned independently. This leads to a high "βV_A" product, which is a popular figure-of-merit for analog circuit design. Another important point regarding Fig. 4 is the onset of the Early effect [Ear52] and avalanche multiplication in the collector-base junction [NCZ+99]. This will be important for the discussion of radiation-induced current transients when the collector is biased to a large positive voltage near BV_{CE0}.

The unity-gain cutoff frequency (f_T) for a high-performance IBM 5AM SiGe HBT is shown in Fig. 5 [CN03]. This is an important figure-of-merit for operation under low

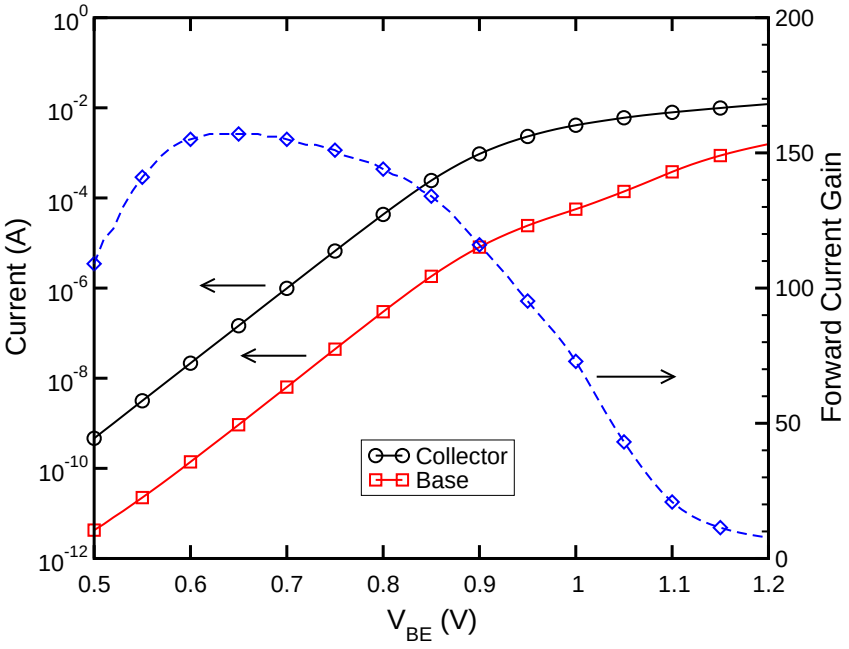

Fig. 3: Gummel curve and forward current gain (β) for an IBM 0.5×2.5 μm^2 5AM high-performance SiGe HBT. The spike in the forward current gain at $V_{\mathrm{BE}} = 0.4$ V is due to an oscillation in the base current at the measurement resolution of the parameter analyzer.

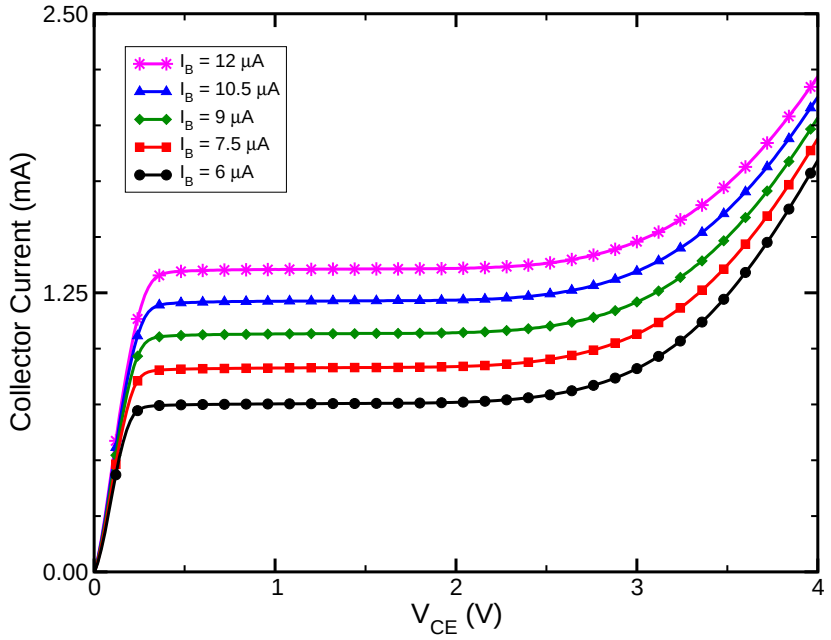

Fig. 4: Forced I_{B} output characteristic at high injection for an IBM 0.5×2.5 μm^2 5AM high-performance SiGe HBT

injection and one of the highlights of SiGe HBT process technology: the devices possess both large current gain and small transit times. When considering the ability of a SiGe HBT to drive a load, the figure-of-merit is the maximum oscillation frequency ($f_{\max}$) [Mas54, CN03], which is related to f_T by

$$f_{\max} = \sqrt{\frac{f_T}{8\pi C_{bc} r_b}}. \tag{1}$$

Neither of these figures-of-merit will be used in this work, but they are important characteristics of the technology and warrant a brief discussion.

SiGe HBTs are intricate from a device physics point of view and use some of the most advanced process technology deployed for large-scale commercial applications. Both the idea of bandgap engineered transistors and research on bandgap engineering with the SiGe material system has been in development since the mid-1950s. The original HBT concept belongs to William Shockley, John Bardeen, and Walter Brattain, described in their 1950-1951 patents [Sho50, BB50, Sho51]. Bandgap engineering theory and HBT device physics were developed a short time after, led by Herbert Kroemer's work [Kro57a, Kro57b, BMH58]. Despite this early development, it took thirty years before serious application development started [Peo86]. The first working SiGe HBT was demonstrated by Subramanian Iyer at the International Electron Devices Meeting in 1987 [IPD$^+$87]. Those first devices were manufactured using molecular beam epitaxy, but it was not an effective method. Bernard Meyerson of IBM developed a technique to manufacture SiGe HBTs using ultra-high vacuum chemical vapor deposition low-temperature epitaxy [Mey86]. Three years later this method led to a SiGe HBT with a peak f_T of 75 GHz [PCM$^+$90], which more than doubled the f_T performance of then-current state-of-the-art silicon bipolar junction transistors.

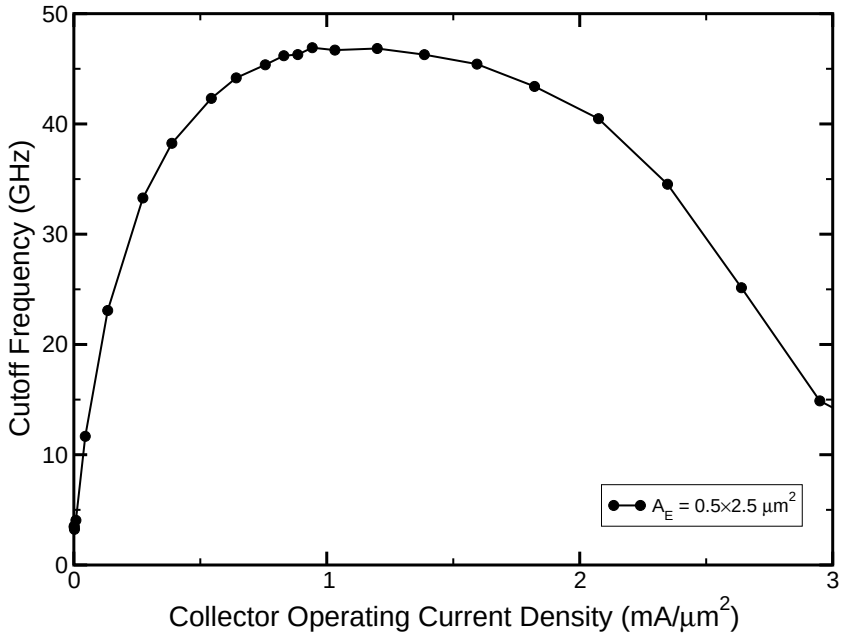

Fig. 5: Unity-gain cutoff frequency (f_T) versus collector operating current density for a 0.5 × 2.5 μm^2 IBM 5AM high-performance SiGe HBT. These data are courtesy of Prof. J. D. Cressler, The Georgia Institute of Technology, and the Georgia Electronic Design Center.

However, from a radiation effects viewpoint, these device performance benefits come with a cost. The two largest factors contributing to single-event effects are device area and the requirement for lightly doped substrates. Most bulk SiGe HBTs are surrounded by deep trench isolation, as shown in Fig. 1. The trenches have a high aspect ratio, which forces them to be thick. The other features of the device, like the subcollector, have lateral dimensions of several micrometers, yielding large device areas even for minimum geometry transistors. Minimum-geometry IBM 5AM SiGe HBTs have a subcollector area of approximately 10 μm^2, making them much larger than their CMOS counterparts. This large device area is manifested through large single-event cross sections for both heavy ions and protons. The lightly-doped substrate, necessary for electrical isolation and radio frequency performance, supports long minority carrier[2]

[2]Electron lifetimes in the case of p-type wafers

lifetimes and long-range potential modulation originating from free carrier interactions with the n^+-subcollector/p^--substrate junction. The subcollector junction serves as a large-area reverse-biased diode that is the primary junction and origin of the majority of single-event effects observed in SiGe HBTs.

This dissertation work is focused on the first-generation IBM 5HP[3] SiGe HBT BiCMOS process [NHM+95]. It has a planar, self-aligned structure with a conventional polysilicon emitter contact, silicided extrinsic base, as well as deep and shallow trench isolation. The process integrates a high-performance 0.5 μm emitter width, 3.3 V BV_{CE0} SiGe HBT with 3.3 V V_{DD}, 0.5 μm drawn CMOS technology. The SiGe HBT component has a peak f_{max} of 70 GHz and a peak f_T of 50 GHz. There is also a high-breakdown SiGe HBT in the process, 5HB[4], with a BV_{CE0} of 5.5 V, though its f_{max} and f_T are reduced. The standard process has five aluminum metal layers. However most of the work here uses the analog metal option, which has six levels of aluminum wiring. This process is known as 5HPAM, but is commonly referred to as 5AM knowing it uses the high-performance SiGe HBT. Marshall's paper from 2000 [MCC+00] used the IBM 5HP BiCMOS process, though at that time it was designated 5S0. Aside from that, all naming conventions are consistent with the previous descriptions.

[3]HP = high-performance
[4]HB = high-breakdown

CHAPTER II

SIGE HBT SINGLE-EVENT EFFECTS

Broadbeam Heavy Ion, Proton, and Laser Circuit Testing

SiGe HBTs are a new semiconductor process technology relative to conventional silicon bipolar junction transistors and metal oxide semiconductor field effect transistors. The first working SiGe HBT was not demonstrated until the late 1980s [IPD+87] and IBM's first commercial SiGe BiCMOS process was not released for another eight years [NHM+95]. While the radiation effects community is becoming more progressive due to the speed of commercical-off-the-shelf parts scaling, there is a lag between when a technology is released and when radiation effects and reliability studies begin. This is due in large part to intellectual property restrictions on the detailed technology information that is required for device and circuit analysis.

After SiGe HBTs were introduced, the first radiation tests completed were total dose [BCV+95, VLT99], dose rate [BNC+99], and displacement damage [RAC+97, RNA+98, NBC+98, ZNC+99] studies. By 2000, the NASA Goddard Space Flight Center, in cooperation with The Mayo Foundation, had fabricated single-event upset (SEU) test structures for high-speed bit error rate test (BERT) broadbeam heavy ion irradiations [MCC+00]. The devices under test (DUTs) were 32-stage serial shift registers composed of non-transparent master-slave rising edge-triggered D flip-flops; they were implemented using current mode logic [Tre89, Wil90]. The circuits were ideally suited for high-speed operation, the only delays being those required for switching currents in the differential emitter coupled logic (ECL) cells. A schematic diagram of the unhardened

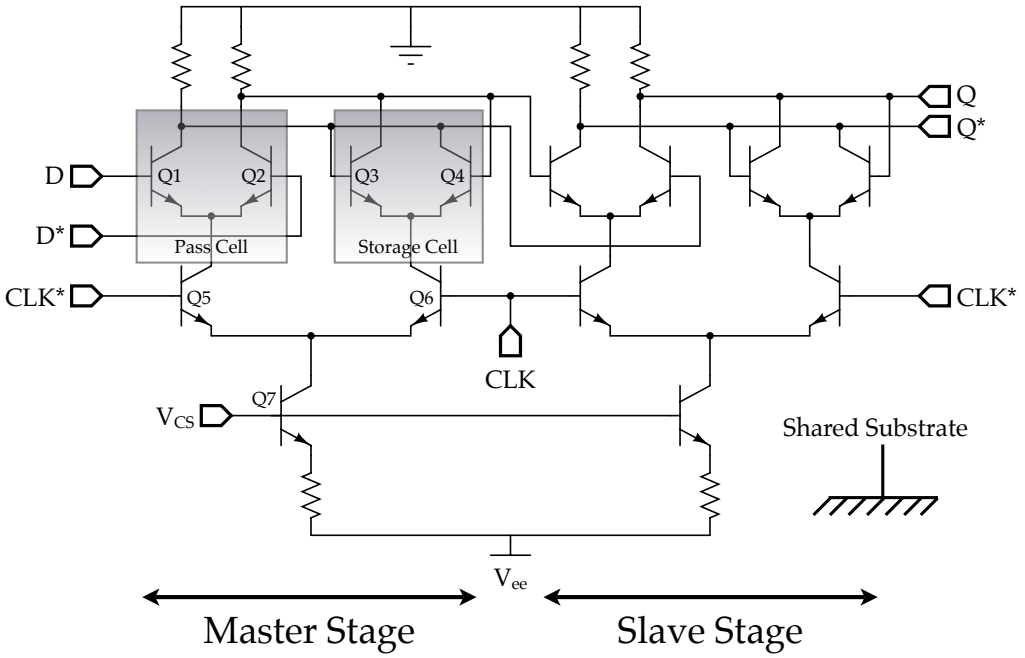

Fig. 6: Transistor-level schematic diagram of unhardened D flip-flop used as a baseline test structure in all SiGe HBT shift register testing [NKC$^+$02, KNC$^+$03, MCC$^+$05]. Each stage consists of two differential ECL cells (pass and storage), a clocking stage, and biasing control. Because the ECL cells are stacked above the clock and bias control stages, the clock and control stages have to be level shifted to ensure forward active operation.

D flip-flop used in the shift register testing is shown in Fig. 6. The master stage consists of a pass cell (Q1 and Q2), a storage cell (Q3 and Q4), a clocking stage (Q5 and Q6), and biasing control (Q7). Since the pass and storage cells are stacked over the clock and control transistors, the clock and control input levels need to be shifted in order to ensure that the transistors operate in forward active mode [NKC$^+$02, KNC$^+$03].

The data from the first high-speed SEU tests on SiGe HBTs are shown in Fig. 7. They show the archetypal low SEU threshold and large saturated SEU cross section common to SiGe HBTs. The low effective linear energy transfer (LET) data – carbon, fluorine, and silicon – show a cross section roll-off with increasing effective LET, which violates central

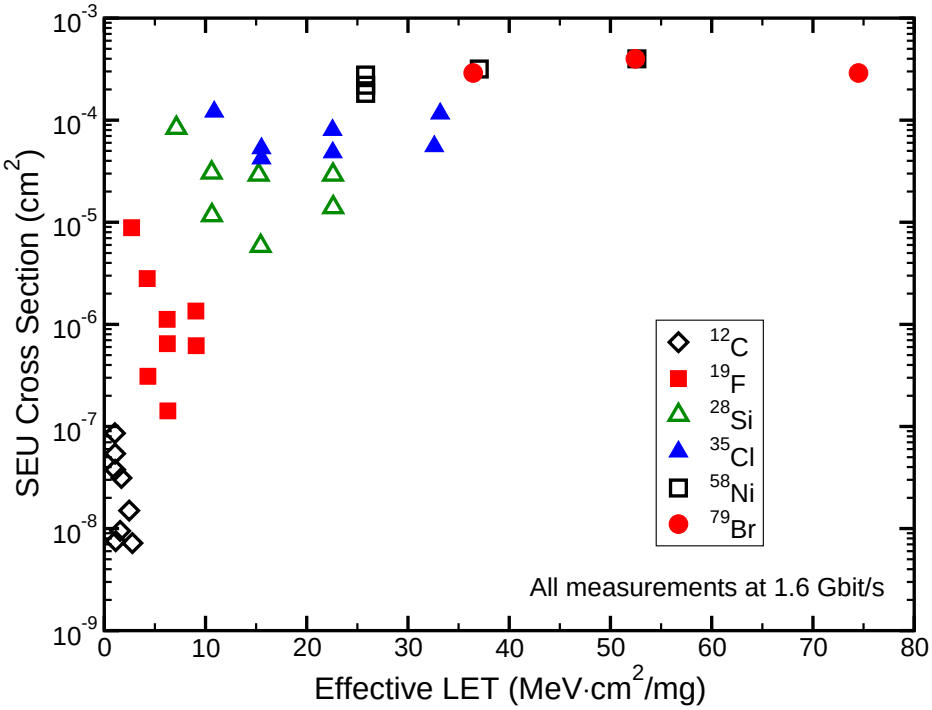

Fig. 7: First high-speed IBM 5S0 SiGe HBT serial shift register SEU data [MCC$^+$00]. These data show that the technology is very sensitive to heavy ion strikes at 1.6 Gbit/s. There is a low SEU threshold and a large saturated SEU cross section. This was the first evidence for the unique geometric effects at low effective LET, suggesting the presence of a vertical sensitive structure and that the IRPP model does not apply.

assumptions of the integrated rectangular parallelepiped (IRPP) model for thin sensitive volumes, suggesting a thick, vertical sensitive structure. These data form the basis for all subsequent SEU studies in SiGe HBTs and, to a large extent, this dissertation work. For a more detailed discussion of LET and RPP volumes, see Appendix A.

Because of Marshall's work in 2000 [MCC$^+$00], engineers spent the next several years developing circuit-level radiation hardness by design (RHBD) [Lac03] techniques to try and improve the single-event response of SiGe HBT applications. These efforts were focused on high-speed applications, based again on current-steering logic serial shift registers. In 2005, P. W. Marshall, *et al.* published one of the most cited papers on high-speed SiGe HBT single-event effects [MCC$^+$05]. The paper presented data

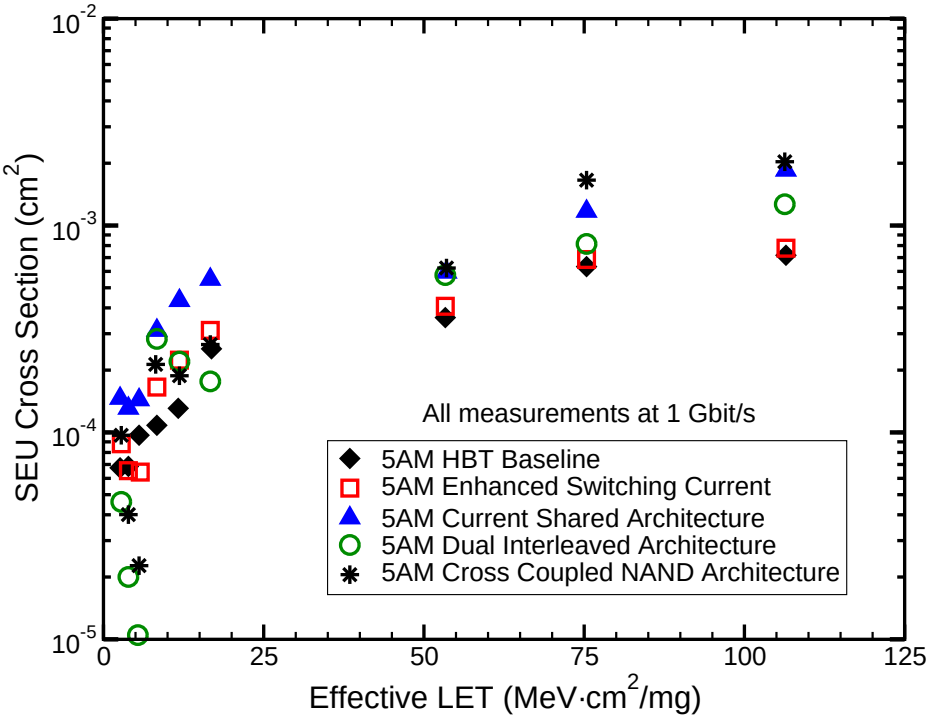

Fig. 8: IBM 5AM SiGe HBT serial shift register heavy ion SEU data for a baseline and initial RHBD architectures [MCC+05]. The DUTs were 127-stages in length and operated at a range of frequencies from 50 Mbit/s to over 7 Gbit/s. This figure shows data taken at 1 Gbit/s. As in Fig. 7, the cross section roll-off at low effective LET is present for all the RHBD designs, but not for the unhardened 5AM HBT baseline design. The data for all designs contain similar variations above threshold.

on five different 127-stage shift register architectures, four of which employed circuit-level RHBD techniques. The baseline design is the same as in Marshall's 2000 work [MCC+00]. The data are shown in Fig. 8.

The data in Fig. 8 are significant for several reasons. First, the data maintain the low SEU threshold and high saturated cross section seen in previous data sets. Second, cross section roll-off at low effective LET is present for hardened designs, supporting previous conclusions regarding violations of the IRPP model [MCC+00, MCC+05]. Finally, the data show that these four RHBD techniques have a negligible impact on SEU cross sections at high effective LET and none produce a limiting cross section, indicating

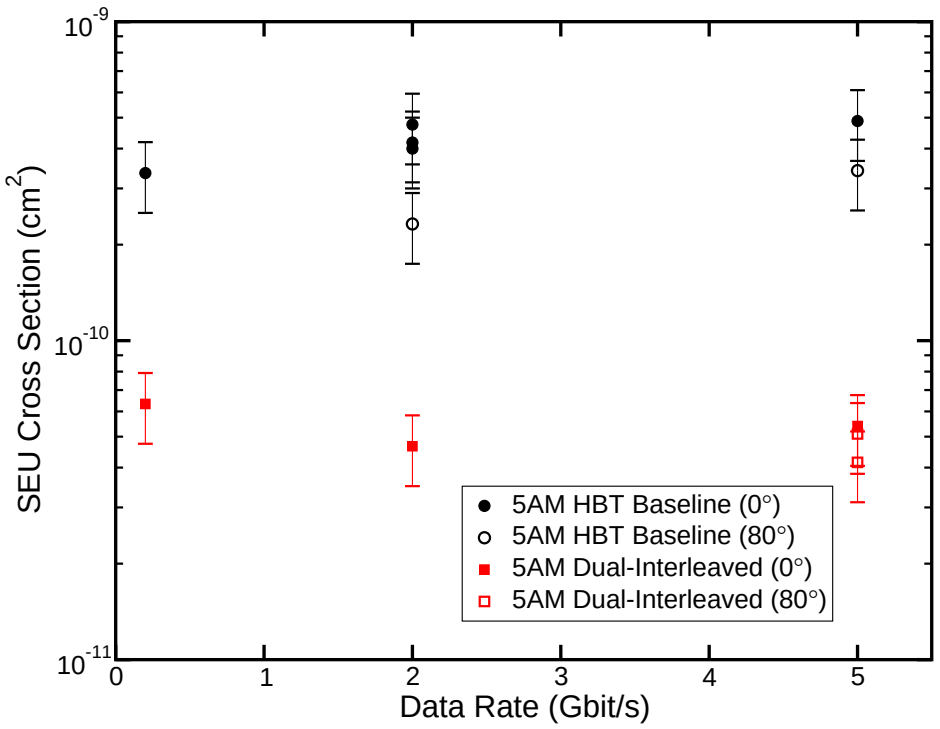

Fig. 9: IBM 5AM SiGe HBT serial shift register proton SEU data for baseline and dual-interleaved CREST architectures [PRS$^+$07]. The data were gathered at the UC Davis Crocker Nuclear Lab using 63 MeV protons at two angles of incidence. The proton cross section does not vary with data rate. The error bars are statistical, representing $\pm 1\sigma$ standard deviation Poisson statistics.

that the onset effective LET is below the lowest effective LET of 2.8 $(\text{MeV} \cdot \text{cm}^2)/\text{mg}$ produced with ^{22}Ne at 15 MeV/u.

In addition to the broadbeam heavy ion SEU testing conducted between 2000 and 2005, broadbeam proton SEU data were collected early in 2007 at the University of California at Davis Crocker Nuclear Laboratory. The DUT was the CREST chip [MCC$^+$05]. Testing examined the IBM 5AM baseline master-slave D flip-flop shift register as well as the 5AM RHBD dual-interleaved architecture. Testing was conducted using 63 MeV protons at normal incidence and 80° over several data rates. The data are shown in Fig. 9 [PRS$^+$07].

SiGe HBT circuits, even hardened architectures, are sensitive to direct ionization from heavy ions, but they are not sensitive to direct ionization from protons [PRS+07]. The SEU data shown in Fig. 9 are a result of indirect ionization from nuclear reactions. Consequently, the SEU cross section is much lower than the heavy ion cross section, since not every incident proton results in a nuclear reaction. Though the proton SEU sensitivity is low, the high trapped proton fluxes present in low earth orbit will contribute significantly to SEU rates in space.

The SEU data shown so far were gathered using BERT tests, which capture both events and bit errors. SEU cross section data are a measure of the number of events, not bit errors. In BERT terminology, events are represented by error intervals. An error interval is the minimum enclosing temporal interval that captures the beginning and end of the constituent bit errors. The SEU cross section is defined in terms of the number of error intervals per fluence, not the number of bit errors per fluence. That is,

$$\sigma_{\mathrm{SEU}} = \frac{\#\,\mathrm{Error\,Intervals}}{\Phi}, \tag{2}$$

where Φ is the beam fluence, usually in cm^{-2}. One way to present bit error data is to look at the average number of bit errors per event (error interval). An example of this for the IBM 5S0 SiGe HBT technology is shown in Fig. 10. Yet another way to view the data is looking at the scaled single bit error fraction versus data rate. This is shown in Fig. 11 [SKM+06].

In addition to examining the number of errors produced by a single event, BERT tests also yield information regarding error morphology and error duration. Marshall's work in 2005 [MCC+05] and Sutton's work in 2006 [SKM+06] include information relating these metrics for IBM 5AM SiGe HBT shift register designs. Sutton identified twelve

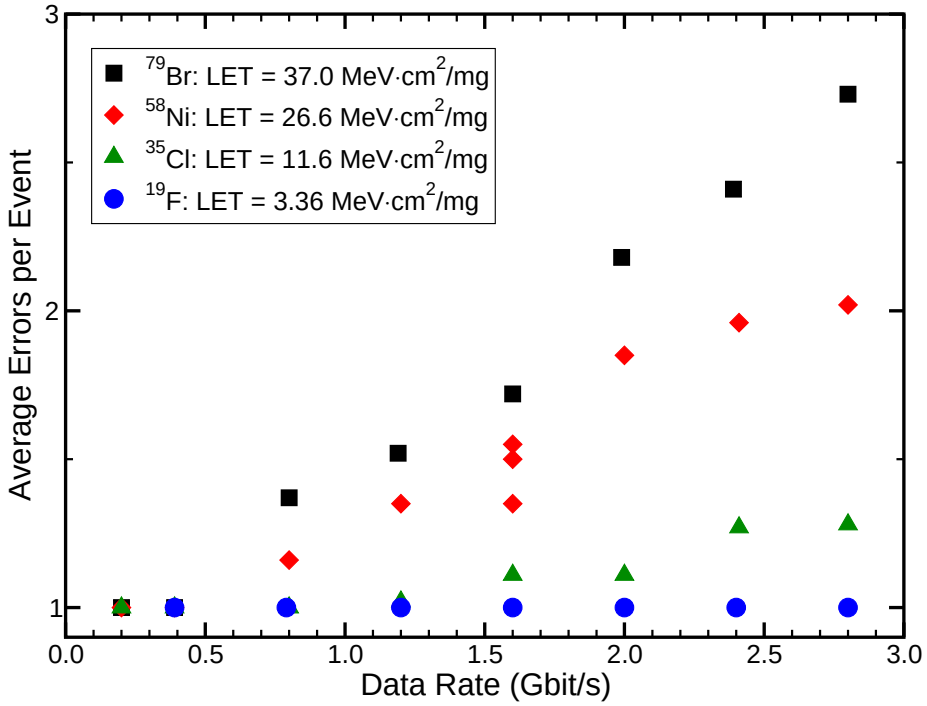

Fig. 10: IBM 5S0 average bit errors per event versus frequency [MCC+00]. For LETs above threshold, the average number of bit errors per event increases with data rate. The average number of errors per event also increases with increasing LET.

different error categories and Marshall recorded error lengths between 4.4 and 51 ns; the error categories are listed in Table 1. While insightful, BERT data sets are very complex and difficult to interpret from the standpoint of basic mechanisms. This dissertation work stepped away from the complexities of high-speed circuit data interpretation and instead constructed a new event rate prediction model for space applications based on charge collection measurements and simulations, and conducted the first experiments looking at single-event current transients in SiGe HBTs.

While broadbeam heavy ion testing is the de facto method for investigating space radiation effects, the test engineer foregoes any positional information regarding the heavy ion strike. Therefore, a particular event cannot be traced to a specific location within the DUT. This issue was overcome in the work published by Sutton, *et al.* in

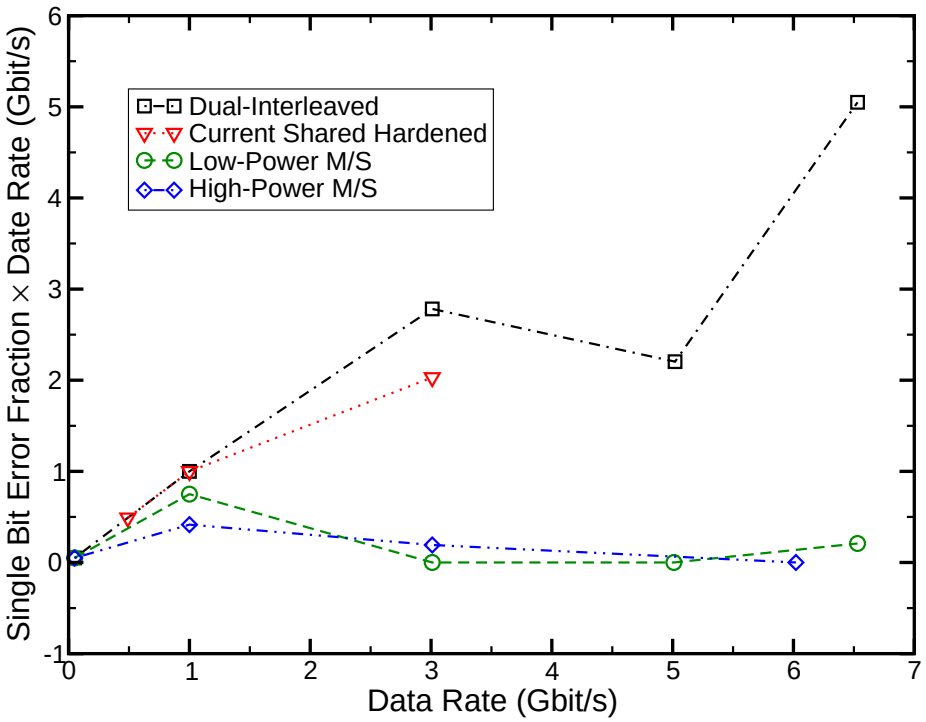

Fig. 11: Single-photon absorption pulsed laser data showing the data rate-scaled single bit error fraction $(0 \rightarrow 1)$ for IBM 5AM SiGe HBT designs [SKM+06]. The architectures with long burst errors at high data rates have an approximately constant scaled single bit error fraction. These data are from the same parts shown in Fig. 8.

2006 [SGJ+06] by using single-photon absorption laser-induced carrier generation. This method allows precise control over the position of the carrier generation as well as the density of carriers generated. That work examined clock buffer sensitivity and data path sensitivity by targeting specific transistors from the master-slave flip-flop designs discussed earlier [NKC+02, KNC+03, MCC+05]. It also examined bias and architecture dependence.

Laser strikes to root clock buffers, those supporting sixteen to sixty-four flip-flops, resulted in up to ten times more bits in error than strikes to local clock buffers, which support either eight or four flip-flops. There was no laser pulse energy dependence for strikes to the clock buffers above the threshold energy for inducing events. There was

Table 1: SiGe HBT SEU Error Categories and Their Descriptions [SGJ+06]

Error Type	Description
Misfire	BIE[1] = 0, a hit on error flag and/or clock circuitry
D0	BIE = 2 and EL[2] = 128, 2 single bit flips separated by 127 bits
Single-Bit	BIE = 1
XOR	A subset of Single-Bit
Flatten to 0	Errored bits were flattened from 1 to 0 and all correct bits 0
Flatten to 1	Errored bits were flattened from 0 to 1 and all correct bits 1
LTOT	$\geq$ 10% to $<$ 25% of bits are in error vs. expected 50%
MBD0	Multiple bit D0, similar to D0, just repeated
Single-Shift	Pattern changes and never changes back, PRNG[3] hit
Double-Shift	Patten changes, then changes back, deleted clock pulse
Multi-Shift	Best attempt to describe the error as multiple shifts
Mangle	Totally scrambled unintelligible errors

[1] bits in error
[2] error length
[3] pseudorandom number generator

no observed tail current dependence during laser testing, which was counterintuitive based on earlier broadbeam heavy ion testing. Strikes to the clock buffers resulted in an even distribution of $1 \rightarrow 0$ and $0 \rightarrow 1$ errors, whereas strikes to Q1 and Q2 in the capture cell of the last D flip-flop (see Fig. 6) produced an asymmetric distribution of errors that were all either flatten to 1 (strikes to Q1) or flatten to 0 (strikes to Q2) depending on which transistor was targeted and the present data state. Strikes to Q1 and Q2 produced a steadily increasing number of bits in error with increasing data rate, a trend not observed when striking transistors in the clock buffers.

Focused Heavy Ion Microbeam Device Testing

Since early 2005, SiGe HBT devices have been tested at Sandia National Laboratories' Ion Beams Materials Research Lab, which houses a High Voltage Engineering

Corporation 6 MV EN tandem Van de Graaff accelerator, which has four types of ion sources and eight beamlines. The purpose of the testing was to study spatially-correlated charge collection using a technique called ion beam induced charge (IBIC) microscopy [BVVS07]. This technique is discussed in detail in Appendix B. The test methodology and data reduction procedures follow the description given by Reed, *et al.* in 2003 [RMP$^+$03].

All of the SiGe HBTs underwent four-probe IBIC so that charge collection on all the terminals (emitter, base, collector, and substrate) could be monitored simultaneously. The emitter, base, and collector were held at 0 V while the substrate was biased to -5 V via the charge-sensitive preamplifier. These charge collection bias conditions are intended to replicate the "off-state" of the DUT, shown to be the most sensitive state in previous work [NKC$^+$02, KNC$^+$03, CHD$^+$06].

All four electrodes were connected to amplifier chains composed of Ortec 142A charge sensitive preamplifiers and Ortec 671 spectroscopy amplifiers. The signals were fed into individual single channel analyzers and then connected to a four-input OR logic unit. The output of the OR logic unit was connected to the gates of the analog-to-digital converters for the X-Y scan generator's output. A signal on any one of the four channels can trigger an event, which causes the position of the ion and charge collected on each device terminal to be recorded. Further information on radiation effects microscopy, including ion beam induced charge methods can be found in [DHWS92, HDS92, HDS$^+$93, VDP$^+$05, VRMP07, RVP$^+$07, BVVS07] and references therein.

All of the microbeam experiments were conducted using normally-incident 36 MeV $^{16}O^{6+}$ ions with a rectangular spot size of approximately 1 μm^2, the focus being achieved

with a quadrupole doublet lens. Due to the finite spot size, low beam current of around 1000 ions/s, and the mass-energy product (ME/q^2) of the oxygen ions, there is a positional uncertainty of order ± 0.5 μm in the x- and y-directions. The ions have a range of 25.5 μm in silicon, a surface incident LET of 5.2 $(\mathrm{MeV} \cdot \mathrm{cm}^2)/\mathrm{mg}$, and a Bragg peak of approximately 7.5 $(\mathrm{MeV} \cdot \mathrm{cm}^2)/\mathrm{mg}$. The penetration depth and LET were determined using Monte Carlo Radiative Energy Deposition (MRED) [HWR+05, KBW+05, WWM+05, BWW+06, RWS+06, WSW+07, WWS+07, RWM+07] calculations. This tool will be discussed in greater detail in the coming sections.

IBIC data are reported for six devices from three different vendors: IBM Corporation [NHM+95, AFS+97, CHM+00], Jazz Semiconductor [RK05], and National Semiconductor [HPC+06], with relevant parameters detailed in Table 2. All devices were subjected to the same ionizing radiation under identical bias conditions. The Jazz HRS and SOI SiGe HBT devices, as well as the NSC epi SiGe HBT device, supplied by BAE Systems, were from experimental hardware lots and are not standard commercial product offerings. All devices are npnn$^+$ with p-type substrates. The DTI in all six devices is approximately the same, being 1 μm wide, 8-9 μm deep, with 4-5 μm between the trench walls, as shown in Fig. 1.

The data sets shown in Figs. 12(a) through 12(c) display integrated charge collection on the collector terminal, since ion-induced collector current is the major cause of SEU in most standard SiGe HBT circuits [NKC+02, KNC+03, RMP+03, PRS+06]. All subsequent plots of charge collection will be for the collector terminal. While the data plots here focus on the collector terminal, the majority of the current sensed on the collector terminal also appears on the substrate terminal. The currents have opposite

Table 2: SiGe HBT Device List for IBIC Testing [PRS+06]

Device Name (Abbreviation)	**Emitter Area** A_E (μm)	**Substrate Resistivity** ($\Omega \cdot$ cm)
IBM 5HP (IBM 5HP)	0.5×10.0	8-10
Jazz SiGe-120 Bulk (Jazz bulk)	0.2×10.16	8-10
Jazz SiGe-120 SOI† (Jazz SOI)	0.2×10.16	8-10
Jazz SiGe-120 High Resistivity† (Jazz HRS)	0.2×10.16	1500
National SiGe-8iED Bulk (NSC bulk)	0.4×20.0	8-10
National SiGe-8iED epi† (NSC epi)	0.4×20.0	0.009

† Not standard commercial product offerings. Experimental hardware lots.

polarities since one current is traveling into the device and one is traveling out of the device.

The plots in the aforementioned figures are slices through what is actually three-dimensional data, though the third dimension has been collapsed against the xy-plane for these charts. The data clearly show the structure of the devices. The peak charge collection occurs for strikes within the DTI and the tails represent charge collection from events occurring outside the DTI. These two regions of data reveal separate charge collection characteristics, which are position dependent. Within the DTI, drift transport dominates due to the extension of the potential into the substrate from the bottom of the subcollector (collector-substrate) depletion region [VNK+03, PRS+06] (the subcollector is shown in Fig. 1). Normally-incident 36 MeV oxygen ions deposit about 26 MeV in the substrate of a typical device, which generates about 1 pC of charge.

The peak charge collection in Figs. 12(a) through 12(c) occurs for ions that cross the reverse-biased subcollector junction, which is contained within the DTI. Ions that pass through the DTI or regions of the device outside of the DTI do not result in maximum

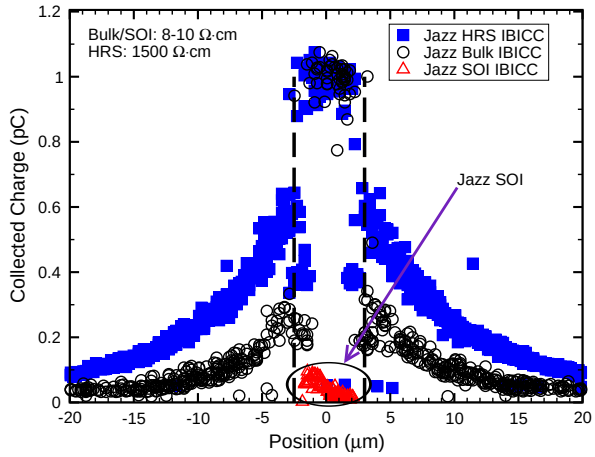

(a) Jazz SiGe HBT IBIC data

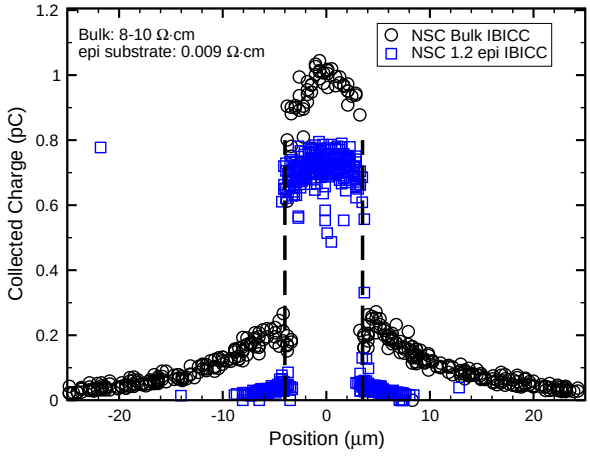

(b) NSC SiGe HBT IBIC data

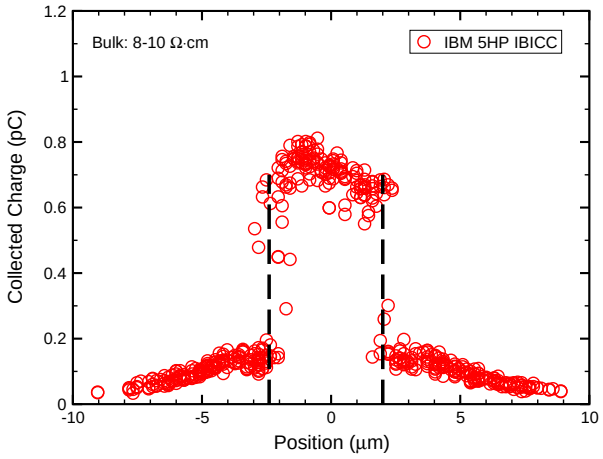

(c) IBM SiGe HBT IBIC data

Fig. 12: IBIC data for six SiGe HBT DUTs. These data sets display charge collection on the collector terminal [PRS+06]. *The Jazz HRS, Jazz SOI, and NSC epi SiGe HBT devices are experimental hardware lots and are not standard commercial product offerings*. In the above three figures, the deep trench isolation boundary is indicated by vertical dashed lines. The substrate resistivities are listed on the individual charts. The absence of a symbol occurring outside the DTI indicates no events were triggered there.

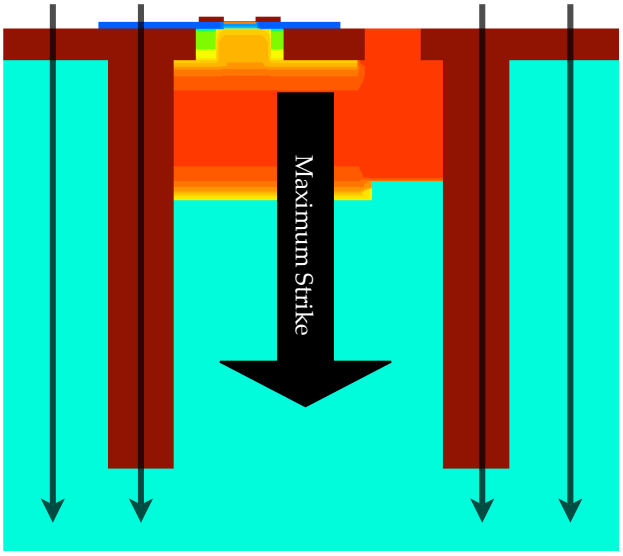

Fig. 13: TCAD cross section showing critical regions for single-event strikes in a bulk SiGe HBT. Peak charge collection occurs when ions cross the subcollector junction, which is contained within the deep trench isolation. Ions that pass through the deep trench or do not cross the subcollector junction – the four small, translucent arrows to the left and right – do not result in peak charge collection efficiency. The device features are fully labeled in Fig. 1.

charge collection efficiency. This is shown graphically in Fig. 13. The microbeam data show this peak to be about 1 pC, a charge collection efficiency of approximately 90%. Outside the DTI, there is no pre-existing electric field to move the charges once they separate from the ion track, so the charge collection is slower and less efficient since the electrons must diffuse to the subcollector junction to induce current on the collector terminal. The tails to either side of the DTI seen in all the figures are representative of this collection mechanism. They peak at about 200 fC and fall off to less than 50 fC in most cases.

TCAD Modeling

The IBM 5HP device was chosen for technology computer-aided design (TCAD) modeling since it represents a broad selection of SiGe HBT technologies and because

Table 3: Physics Models for DESSIS v10.0.6 IBIC Calibration Simulations

Physics	Effective Intrinsic Density SlotBoom bandgap narrowing Fermi statistics Phillips Unified Mobility High Field Saturation Doping Dependent SRH recombination Auger recombination
Math	Extrapolate Exact derivatives Iterations = 10 NotDamped = 15 RecBoxIntegr Relative error control Backward Euler transient solver

of access to calibrated TCAD models. The device model used in this work is based on the structure described in [VNK+03]. All of the TCAD simulations were three-dimensional single device simulations executed with ISE DESSIS v10.0.6[1]. The models used for simulation are listed in Table 3.

IBIC microbeam data, shown in Fig. 12(c), was used in order to both extend the work presented in [VNK+03] and to calibrate charge collection simulations for normally-incident 36 MeV ^{16}O ions, identical to the ones used in the microbeam experiments. The LET profile for the simulated oxygen ions was generated using MRED, which is similar to the profile used in [VNK+03]. Using an iterative process, the silicon model parameters for bulk electron lifetime were modified until reasonable agreement with experimental data was achieved. The calibrated charge collection simulation points are shown in

[1]ISE AG was purchased by Synopsys Inc. who now maintains their TCAD tool suite. DESSIS has been subsumed into the SDEVICE tool. DESSIS was the standard commercial TCAD device simulator when this work was done.

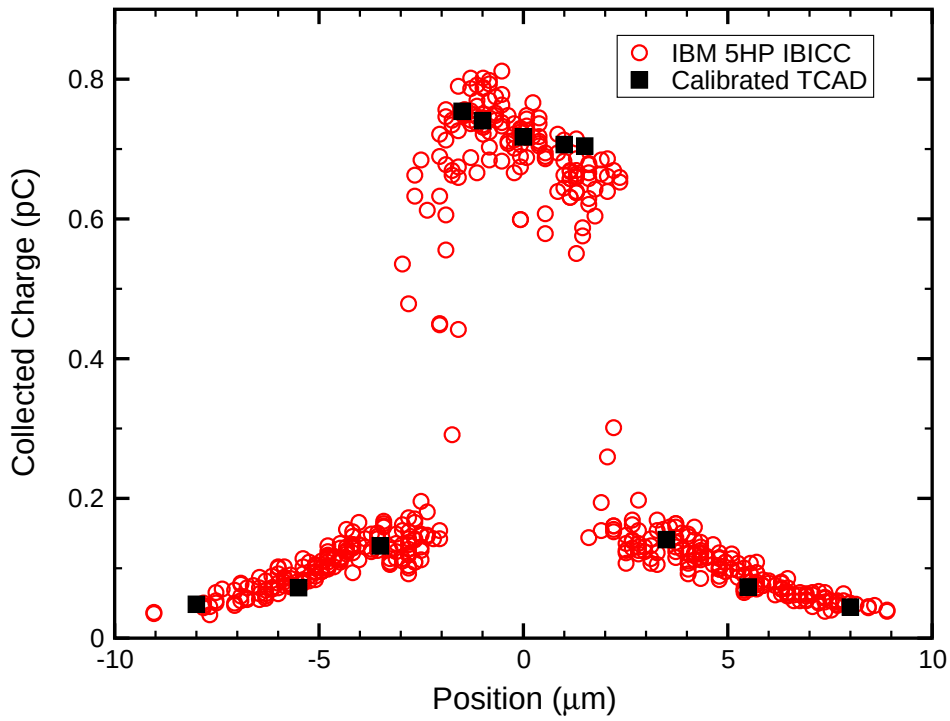

Fig. 14: Calibrated IBM 5HP TCAD IBIC simulation [PRS+06]. The calibration was achieved by iteratively adjusting the electron lifetime in the bulk silicon substrate. The simulation results are overlaid on the IBIC data from Fig. 12(c).

Fig. 14 as “Calibrated TCAD" points. These results are discussed in greater detail elsewhere [Pel06].

Bulk SiGe HBTs are built directly on 8-10 $\Omega \cdot$ cm p-type silicon, which has minority carrier diffusion lengths in excess of 100 μm. Isolated test structures, like the DUTs used for these charge collection experiments and simulations, essentially have infinite substrates. However, this cannot be modeled in TCAD due to reflective (ideal Neumann) boundary conditions. They are defined such that

$$\vec{F} \cdot \hat{n} = 0\,, \tag{3}$$

where the normal component of the electron and hole current density at the boundary

is equal to zero. In other words

$$\vec{J}_n \cdot \hat{n} = 0\,, \tag{4}$$

and

$$\vec{J}_p \cdot \hat{n} = 0\,. \tag{5}$$

Any boundary without an explicit contact definition is modeled this way, which creates problems for single-event TCAD simulations because it is impossible to create an infinite silicon slab.

Artificially manipulating the bulk minority carrier lifetime in the TCAD device substrate is a nonphysical solution to the problem of approximating an infinite substrate. The physically-accurate brute force solution to this problem is to make a very large 3-D TCAD device, perhaps 300 μm on a side. This is wasteful, inefficient, and can create an unmanageable physical memory footprint while executing. A better solution, first proposed by CFD Research Corp., is to create a low-lifetime wrapper layer encasing the original TCAD 3-D volume [TR07, SBC$^+$07]. The wrapper layer has short electron and hole lifetimes, of order 10 ps, with generation disabled. As soon as free carriers hit this wrapper layer, they undergo Shockley-Read-Hall recombination and are eliminated. This concept, in effect, creates absorptive boundary conditions for the substrate boundaries and is a viable alternative to the bulk carrier lifetime modification method published by Pellish, *et al.* in 2006 [PRS$^+$06]. The "wrapper-layer" technique is superior to modifying bulk lifetime because it alters free carrier device physics in a smaller, noncritical volume. However, it is still an approximation. The choice of bulk substrate size (not wrapper layer size) and the wrapper layer carrier lifetimes can still affect the carrier gradient in the substrate, which can impact the computed result. If

computationally possible, the best solution is still a large substrate that allows realistic carrier transport to unfold.

CHAPTER III

EVENT RATE PREDICTION MODEL AND METHOD

A generalized event rate prediction model is applied to two different D flip-flop shift register designs fabricated in the IBM 5AM SiGe BiCMOS (IBM 5AM) process: a baseline design and a radiation hardened by design (RHBD) variant. This process is characterized by a 0.5 μm drawn emitter width, a unity-gain cutoff frequency of 50 GHz, and a BV_{CE0} of 3.3 V [NHM+95, AFS+97, CHM+00].

Of the two IBM 5AM designs considered here, one was a baseline, nominal switching current, D flip-flop shift register design [MCC+05] and the other employed a RHBD dual-interleaving technique that included duplicated pass and storage cells, which effectively decoupled the differential inputs and outputs in the storage cell [KNC+03, MCC+05]. This input/output decoupling increased the critical charge (Q_{crit}) of this design[1]. For the sake of simplicity, these designs are referred to as "baseline design" and "RHBD design" throughout this chapter. Both shift register designs are 127-bits long and were fabricated solely out of IBM 5AM SiGe HBTs; no complementary metal-oxide semiconductor transistors were used.

Context and Motivation

It is important to understand the basic physical structure of a typical bulk SiGe HBT since the single-event response is driven mostly by structural processing geometry

[1]Critical charge is the amount of charge that must be collected at the terminal of a circuit to cause a single-event effect, such as a single-event upset. The author recognizes that critical charge becomes an anomalous quantity under certain circumstances. The use of critical charge in this context is necessary will be made clear.

[MRP+08]. A colorized scanning electron micrscope cross section of the IBM 5AM process is shown in Fig. 1. Three features dominate single-event charge collection: the deep trench isolation (DTI), the lightly doped substrate, and the large area of the reverse-biased subcollector junction that is a minimum of approximately 10 μm^2.

Microbeam data sets [VNK+03, PRS+06, CHD+06, RVP+07, SBC+07, VRMP07, MRP+08] of several different bulk SiGe HBT process generations have shown that individual devices exhibit significant charge collection from lateral distances on the order of 10 μm from the active region and significant vertical collection to depths of approximately 15 μm under the active region of the device. These lateral and vertical charge collection distances are governed by the lightly doped substrate and the 3-5 V dropped across the subcollector space charge region (SCR). While the microbeam data sets provide unique insight into charge collection mechanisms [RMP+03, VNK+03, PRS+06, CHD+06, RVP+07, VRMP07, SBC+07], it is difficult to obtain reliable angular microbeam data sets, so broadbeam experiments must be used. A limited amount of small-angle microbeam data were presented by Montes, *et al.* [MRP+08].

The primary broadbeam heavy ion data set [MCC+05] upon which this work is based is shown in Fig. 15. It is apparent that with the low linear energy transfer (LET) neon ion, the cross section of the RHDB design does not increase with increasing angle, but instead *decreases* with *increasing* angle—*i.e.*, decreasing cross section with increasing effective LET. This behavior is not consistent with the behavior of the integrated rectangular parallelepiped (IRPP) model for thin volumes, which yields increasing cross sections with increasing effective LET [PPAS92, PPS+93, PPM+05]. This lack of agreement between the IRPP model and data was discussed in detail in [MRP+08]. Since these

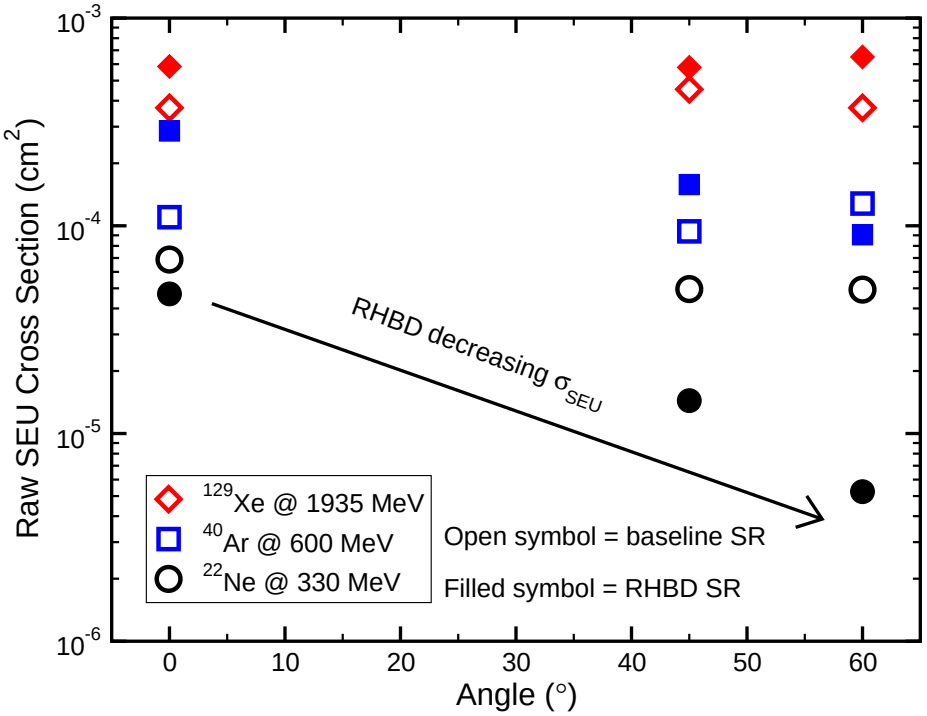

Fig. 15: Broadbeam heavy ion data for the baseline and RHBD 127-stage shift register designs after [MCC+05, PRS+07]. The important feature is the cross section decrease with increasing angle for the RHBD device with a higher critical charge. This roll-off behavior violates IRPP model assumptions, so all RPP and linear charge deposition cosine corrections have been removed. The data are plotted with respect to angle and the cross section was scaled by $\cos(\theta)$ to remove the effective fluence correction.

data are not described adequately by the default IRPP model, they have been re-plotted with the cosine corrections removed. The data are plotted as a function of angle instead of effective LET and the cross section is scaled by $\cos(\theta)$ to remove the effective fluence correction; it is the raw cross section value. All subsequent data sets in this chapter are plotted in this manner to avoid confusion.[2] For the sake of reference, the normally-incident LETs for the ions in Fig. 15 are: $^{22}\text{Ne} = 2.8\ (\text{MeV}\cdot\text{cm}^2)/\text{mg}$, $^{40}\text{Ar} = 8.3\ (\text{MeV}\cdot\text{cm}^2)/\text{mg}$, and $^{129}\text{Xe} = 53\ (\text{MeV}\cdot\text{cm}^2)/\text{mg}$.

[2]Many test facilities incorporate the IRPP cosine corrections into their beam management software, so LET and fluence are often effective values by default, which is something experimentalists need to recognize.

While the microbeam data presented in Chapter II provide adequate information to develop an energy deposition response model for normally-incident particles, most of the particles in an isotropic environment, like geosynchronous orbit, are incident at large angles. The solid angle of a cone, shown below in Eq. 6,

$$\Omega = 2\pi \left[1 - \cos\left(\frac{a}{2}\right)\right], \tag{6}$$

can be used to approximate a plane of sensitive volumes. When the apex, a, is equal to 120°, $\Omega = \pi$, which is half the solid angle subtended by the surface of a hemisphere. This means that half of the particles in an isotropic environment will be incident at angles below 60° and the other half at angles above 60°. Since a large number of particles are incident at oblique angles, understanding the angular response of bulk SiGe HBTs is critical to developing a representative rate prediction model.

Device Modeling

The two types of ion-device interactions considered are normally-incident and large-angle heavy ion strikes with stopping powers of 2.8 $(\text{MeV} \cdot \text{cm}^2)/\text{mg}$, consistent with the 330 MeV ^{22}Ne used in [MCC$^+$05], where the large cross section deviations occurred. The large angle strike is at 60° relative to the surface normal of the device in order to maintain consistency with the broadbeam data set shown in Fig. 15.

Position-dependent, normally-incident heavy ion data for the IBM 5AM process are available through the microbeam data sets in Fig. 7 in [VNK$^+$03], Fig. 2(c) in [PRS$^+$06], and Fig. 3(a) in [MRP$^+$08]. These data show that 36 MeV ^{16}O strikes within the region bounded by the deep trench isolation result in a charge collection efficiency

of approximately 80%, assuming that about 1 pC of charge is liberated during the range of the oxygen ion, which is approximately 25 μm in pure silicon.

Normally-incident 36 MeV ^{16}O strikes outside the DTI have a maximum charge collection efficiency of approximately 20%. That efficiency falls off to a few percent at $\geq$ 8 μm outside the DTI. Though the IBM 5AM microbeam data sets only report a measurable charge collection signal up to 8 μm outside the DTI, other microbeam data sets with the same substrate resistivity and deep trench isolation geometry [PRS$^+$06], most notably the bulk SiGe HBTs in Figs. 2(a) and 2(b) therein, show measurable charge collection in excess of 15 μm outside the DTI.

Reliable position-dependent charge collection data gathered at a specific angle, even small angles less than 20°, are difficult to obtain with the microbeam due to spatial and mounting constraints within the beamline vacuum chamber. Therefore, angular effects need to be inferred from broadbeam data and confirmed with 3-D TCAD simulations. The two heavy ion broadbeam conditions of interest were simulated in the IBM 5AM TCAD model described in [VNK$^+$03, PRS$^+$06, MRP$^+$08] using a particle track with $dQ/dx = 0.028$ pC/μm. The device was biased in the off-state: $V_{\mathrm{E,B,C}} = 0$ V and $V_{\mathrm{Sub}} = -4$ V. The substrate voltage was taken from the test conditions for the D flip-flop shift registers [MCC$^+$05]. The off-state was previously determined to be the most sensitive operating condition [KNC$^+$03, HCJ$^+$06, CHD$^+$06]. The simulations were carried out using the Synopsys TCAD tool suite and version X-2005.10 of Sentarus Device. The simulation models used are listed in Table 3. Note that this is a newer version of the device simulator than ISE's DESSIS, which was described in conjunction with Table 3. The results of the simulations are shown in Figs. 16(a) and 16(b).

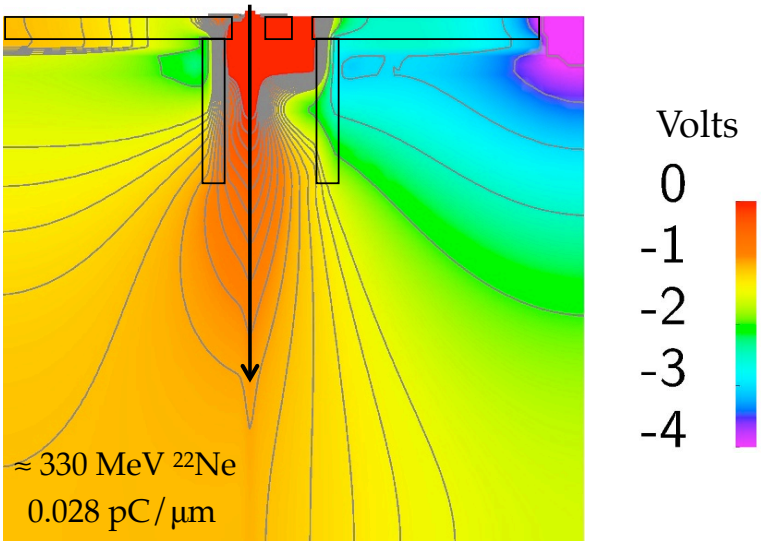

(a) 330 MeV ^{22}Ne strike at 0° through the emitter of an IBM 5AM SiGe HBT

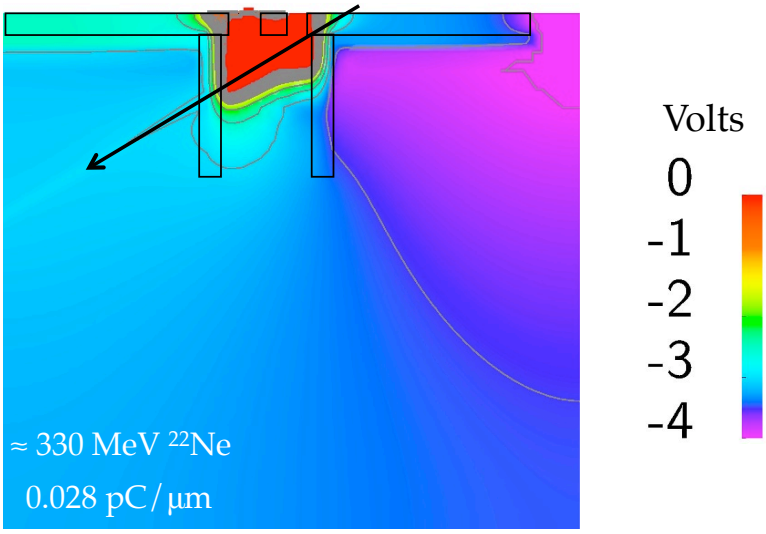

(b) 330 MeV ^{22}Ne strike at 60° from right-to-left through an IBM 5AM SiGe HBT

Fig. 16: 3-D TCAD simulations of 330 MeV ^{22}Ne strikes through a 0.5×2.5 μm^2 IBM 5AM SiGe HBT showing the electrostatic equipotential contour lines at the peak of the temporal-Gaussian ion strike, $t = 10$ ps, which is centered at $t_0 = 10$ ps and has a half-width of 2 ps. In both images, 16(a) and 16(b), the substrate p-tap is located on the right side of the figure, where the potential is pinned at -4 V. The normally-incident strike through the emitter produces potential warping, or push-out, into the substrate, down to a depth of approximately 18 μm in Fig. 16(a). In contrast, the 60° strike shown in Fig. 16(b) exhibits none of the potential warping seen in 16(a). The ion-deep trench isolaton interaction essentially cuts off any subcollector junction response that could affect the electrostatic potential in the substrate.

Comparing Figs. 16(a) and 16(b) is a straightforward, visual explanation of the cross section roll-off observed in the heavy ion broadbeam data plotted in Fig. 15. For normally-incident strikes, the potential dropped across the subcollector SCR will often push-out into the substrate resulting in a large amount of collected charge. This push-out is very similar to the funneling mechanism described by Hsieh [HMO81b, HMO81a, HMO83], Hu [Hu82], and McLean [MO82]. This topic, in the context of SiGe HBTs, has been discussed [PRS$^+$06, MRP$^+$08, PRM$^+$08]. At large angles though, the potential push-out into the substrate is mitigated by the ion passing through the deep trench isolation. In this case, since a large portion of the charge liberated by the ion appears outside of the deep trench and far away from the SCR of the subcollector junction, a sufficiently large potential-compensating charge density cannot be maintained in the SCR, resulting in no potential push-out.

This same mechanism occurs in both the baseline and RHBD IBM 5AM D flip-flop shift register designs. However, the difference in Q_{crit} between each design, $Q_{\text{crit}}(\text{baseline}) < Q_{\text{crit}}(\text{RHBD})$, means that each will have a different response. At normal incidence, each design behaves in the conventional manner – larger amounts of charge liberated in the substrate result in higher cross sections. However, at oblique angles, though approximately the same amount of charge is liberated, the collection efficiency of that charge is much lower since the device response is different, and less dramatic.

At low LETs, as in the case of 330 MeV ^{22}Ne, which is close to the designed SEU threshold, the angular response of the RHBD design makes a large difference in the cross section trend since the amount of charge collected drops with increasing angle, approaching the value of Q_{crit}. The baseline design, though it experiences the same

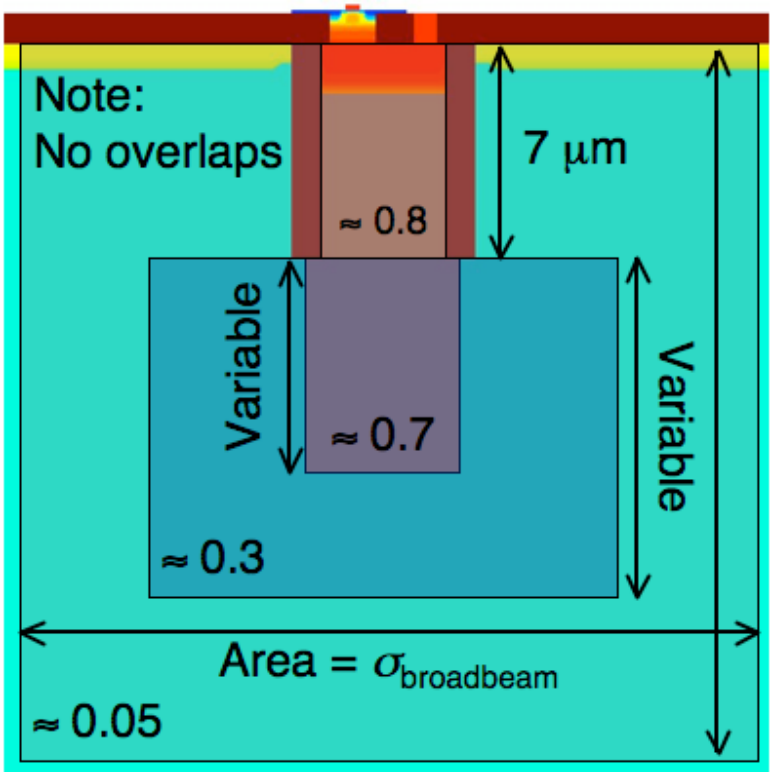

Fig. 17: This is the basic weighted fiducial volume ensemble used to model the radiation response of the IBM 5AM SiGe HBT process. The top-down area is estimated from the normal-incidence cross section of each ion in the broadbeam heavy ion data set – three estimations in this case. The weights (efficiencies) of each of the volumes were derived from microbeam data and previous TCAD simulations [PRS+06, MRP+08].

angular response as the RHBD design, still collects enough charge to sufficiently exceed its lower Q_{crit}, which maintains the normal-incidence cross section.

A heavy ion threshold LET has never been measured for a first-generation SiGe HBT circuit design [MCC+00, MCC+05]. The laser testing in 2006 was able to find threshold energies for single-photon absorption [SKM+06], but its equivalence to heavy ion testing is debatable for devices fabricated on lightly-doped substrates. In 2003, Reed, *et al.* measured the SEU cross section of a second-generation IBM SiGe HBT shift register design with 40 MeV/u ^{22}Ne, which has an LET of approximately 1 $(\text{MeV} \cdot \text{cm}^2)/\text{mg}$; this still resulted in measured events. In 2006, Krithivasan, *et al.* presented limiting

cross sections for three different third-generation IBM (8HP) master-slave D flip-flop shift register designs for LETs of 2.8, 5.8, and 12 $(\mathrm{MeV} \cdot \mathrm{cm}^2)/\mathrm{mg}$ [KMN+06].

The fact that a threshold LET has never been experimentally determined for IBM 5AM SiGe HBT applications makes assigning a critical charge to a particular circuit design an engineering judgement, though it can be a well-grounded and educated judgement. In the following sections, a sensitive volume model will be developed for event rate simulations. This sensitive volume model is used to fit heavy ion and proton simulations to data. This fitting process produces a self-consistent critical charge that is used to evaluate event rate calculations for each of the two designs considered. The critical charges determined through broadbeam heavy ion simulation compare well to unpublished values of critical charge derived through Cadence Spectre circuit simulations.

Energy Deposition Response Model

This work relies on the energy transport and calorimetry capabilities of the Monte Carlo Radiative Energy Deposition (MRED) tool set, which are described in [How05, HWR+05, KBW+05, WWM+05, RWS+06, Pel06, RWM+07, WSW+07, WWS+07]. Using this tool, it is possible to compute the energy deposited in one or more sensitive (fiducial) volumes due to impinging ions. Furthermore, these fiducial volumes can have weights. The volumes and their weights function in an ensemble to form a linear combination that approximates the total collected charge. This idea was first reported by Warren, *et al.* in *IEEE Electron Device Letters* [WSW+07], and subsequently in *IEEE Transactions on Nuclear Science* [WWS+07]. The approach is described by Eq. 7. The total

collected charge is the sum over all fiducial volumes of the product of the weight and total charge liberated.

$$Q_{\text{coll}} = \sum_i \alpha_i Q_{L_i} \tag{7}$$

The total charge liberated (Q) is related to the total energy deposited (ED) through the relationship $Q = (1 \text{ pC}/22.5 \text{ MeV}) \times ED$. This linear combination of weighted fiducial volumes is the construct that will be used to model the energy deposition response of the SiGe HBTs considered in this work. Once calibrated to heavy ion broadbeam cross section data, this modeling method provides a suitable high-speed approximation to the initial conditions and ensuing temporal evolution of charge transport and collection.

A 2-D projection of the basic energy deposition response model is shown in Fig. 17. The fiducial volumes have been overlaid on a TCAD cross section [VNK+03, PRS+06, PRS+07, MRP+08]. The top-down area of each volume is determined by the normally-incident cross section of the broadbeam heavy ion data, which includes ^{22}Ne, ^{40}Ar, and ^{129}Xe. The weights and depths of each of the volumes are calculated by correlating microbeam data to TCAD simulations, both of which have been discussed previously [VNK+03, PRS+06, MRP+08]. This model was used in a fully-reconstructed 3-D model of a shift register stage for all subsequent simulations, including the calibration steps. An image of this 3-D model is shown in Fig. 18. The response model shown in Fig. 17 is sufficient to model one stage of the shift register chain previously described [MCC+05].

An important feature of the model shown in Fig. 17 is that it is scalable within the limits evaluated here. The transistors in the baseline and RHBD designs are different sizes. The RHBD transistors are 0.5×2.5 μm^2, whereas the baseline transistors are

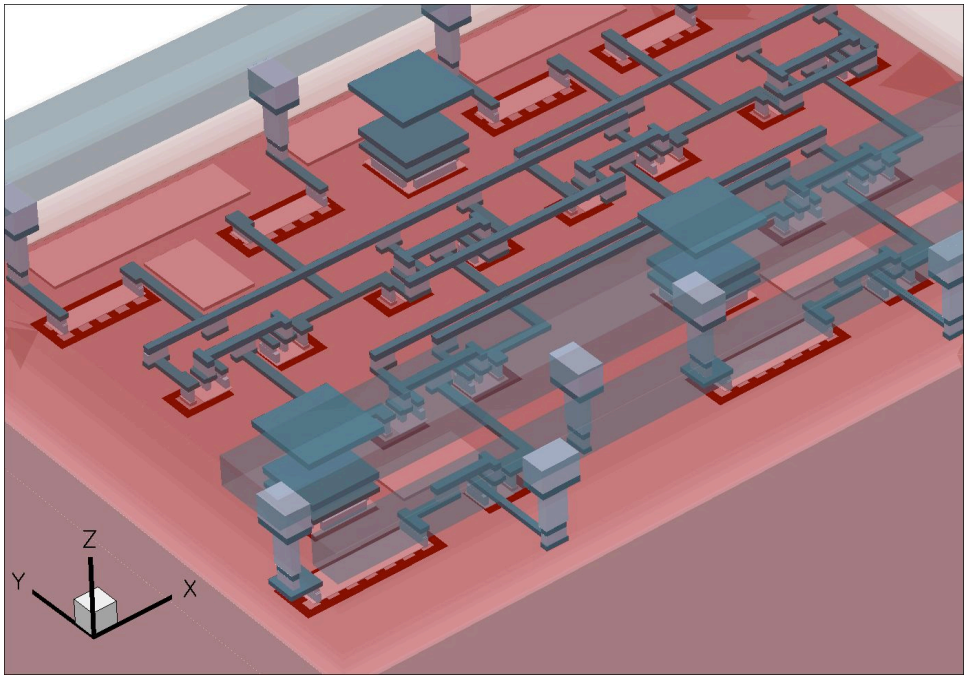

Fig. 18: Full 3-D solid geometry model of the baseline shift register design. The interlevel dielectric and metal have been made transparent. This model, and the one for the RHBD design, were used for the radiation transport simulations. The models themselves are quite large – 110 μm $\times$ 85 μm $\times$ 75 μm in the case of the baseline design and 217 μm $\times$ 85 μm $\times$ 75 μm for the RHBD design.

0.5×1.0 μm^2. The difference in transistor size accounts for some of the cross section difference between the baseline and RHBD designs for the argon and xenon data in Fig. 15. The model dimensions can be adjusted within reason to account for the size difference without making drastic geometrical or phenomenological changes. The top-down areal cross section is dictated by the data and does not require modification.

The volume depth and weight need to be modified for different transistor sizes because the geometry of the subcollector junction changes with the emitter length. A larger junction presents a larger solid angle to free carriers in the substrate, which results in higher collection efficiency. A larger junction also results in deeper potential push-out, though this only occurs to a point, plateauing around 18-20 μm below the base-collector junction.

Recalling the ion strikes highlighted in Figs. 16(a) and 16(b), the linear combination of fiducial volumes shown in Fig. 17 approximates both ion strike conditions. It is clear that the most collected charge will result from normally-incident strikes within the region bounded by the deep trench isolation. Since the broadbeam data in Fig. 15 show nearly constant cross sections over angle, with the exception of the RHBD data for neon and argon, the larger fiducial volumes have an aspect ratio close to unity.

Response Model Calibration

Before computing on-orbit event rates, the model was verified against data sets that covered enough of the possible response-parameter space to ensure predictable behavior in a more diverse environment such as geosynchronous or low-earth orbit. The model described in Chapter III was calibrated to the heavy ion datasets for the baseline and RHBD designs shown in Fig. 15.

In each of the two cases, the calibration scheme is the same and follows this general procedure:

1. Size top-down area of all three fiducial volumes corresponding to their counterpart heavy ion cross section at normal incidence – neon, argon, and xenon in this case.
    (a) This step excludes the volume contained entirely within the deep trench isolation, labeled with a weight of 0.8 in Fig. 17. The normal-incident neon cross section is slightly larger than the in-trench silicon area in both the baseline and RHBD design data.
2. Infer the thickness and weight of each volume from microbeam or laser test data

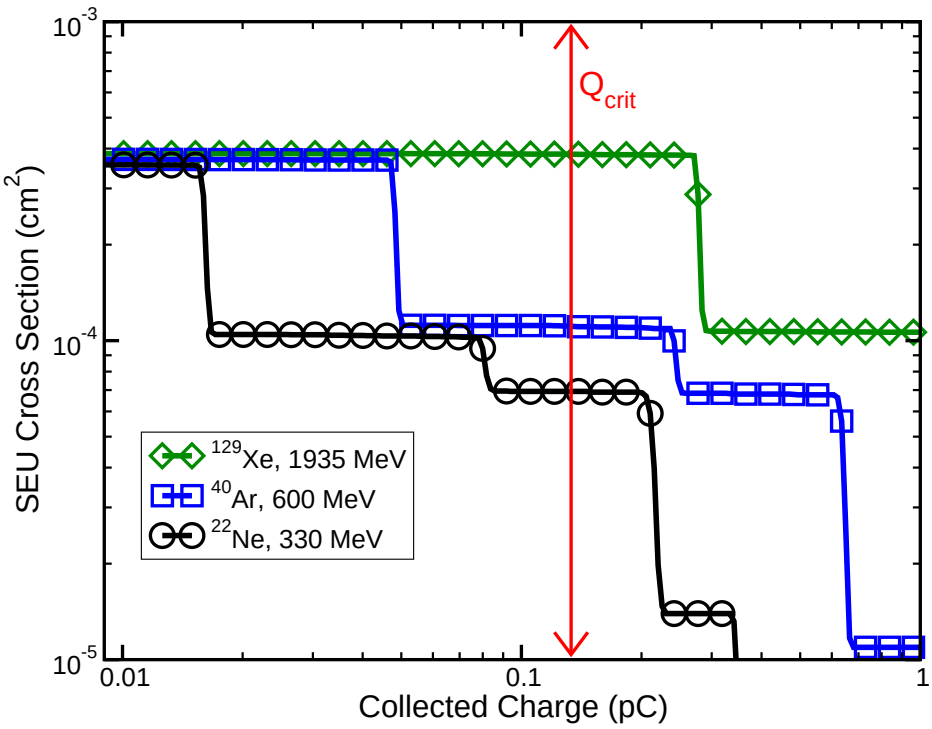

Fig. 19: This figure shows simulated MRED charge collection cross sections at normal-incidence for the baseline shift register design. The Q_{crit} is chosen so that the extracted cross section most closely matches the dataset in question. Data markers are sparse to aid viewing – every 5th point.

and TCAD simulations. The numbers listed in Fig. 17 are appropriate starting values.

3. Simulate all ions in the dataset at normal incidence to check that this simplest case returns the correct result.

   (a) At this point, a critical charge must be determined so that the cross section can be evaluated with consistency for all ion species and angles. An example cross-section collected charge curve is shown in Fig. 19.

4. Simulate each set of ion angles individually and make minor adjustments to the thickness and weight of the appropriate fiducial volumes.

5. Finally, in order to gain a self-consistent solution, all data points must be simulated,

the results evaluated using the same critical charge value, and an accurate match to all data achieved.

At this point it is important to mention a feature of the simulation results displayed in Fig. 19: the device sensitivity is dominated by direct ionization from the primary incident particle. This fact could also be derived from the low SEU threshold in combination with the knowledge of large charge collection volumes. Regardless of this fact, all simulations were carried out with complete physics lists, including the Geant4 binary intra-nuclear collision cascade [FIW04] to determine the final state for ion-ion nuclear reactions. In addition to the binary cascade model, the rest of the Vanderbilt physics list was used. This includes the Standard Screened electromagnetic model [MW91, MW05], both Pi-K elastic and inelastic models, and the alternative ion inelastic model. The calibrated heavy ion results for both the baseline and RHBD circuit designs are shown in Figs. 20(a) and 20(b). The Q_{crit} for each of the calibrations is displayed on the individual figures – 0.13 pC for the baseline design and 0.26 pC for the RHBD design. Considering the sizes of the sensitive volume structures, this is a very achievable charge collection value for many ions in the space environment.

The experimental data shown in Fig. 15 were gathered and published in 2005 [MCC$^+$05] and only included heavy ion cross sections. Proton data were collected during a set of experiments in March 2007 on the CREST chip [MCC$^+$05] at the Crocker Nuclear Laboratory (CNL) at the University of California at Davis using 63 MeV protons [PRS$^+$07]. As with other high-speed bit error rate tests, all the cross sections reported refer to the event cross section and not the error cross section.

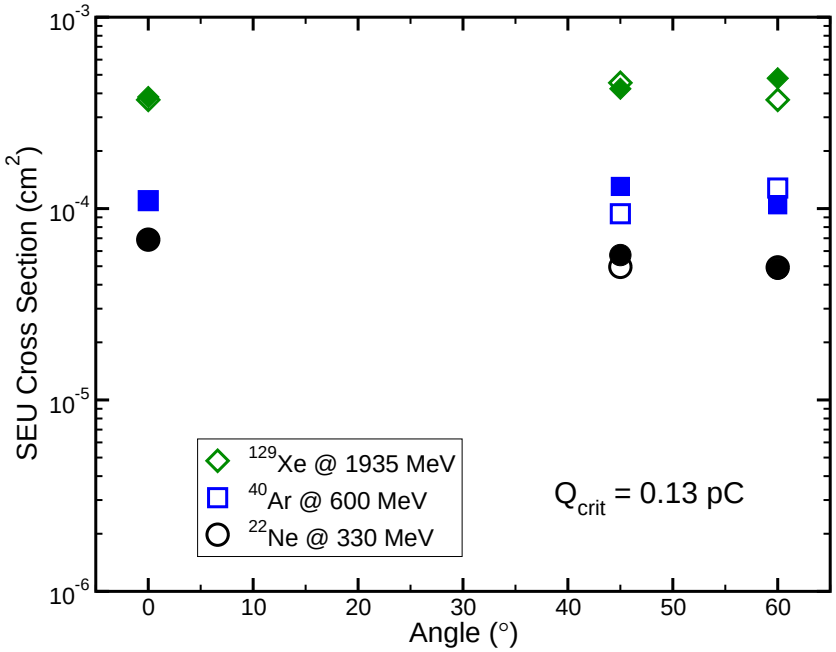

(a) IBM 5AM Baseline SR Data and Simulations

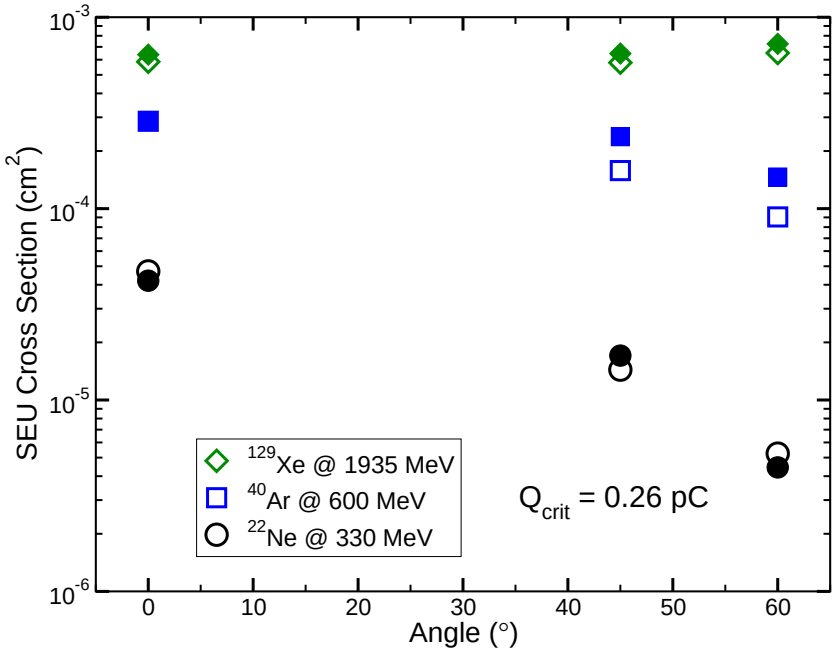

(b) IBM 5AM RHBD SR Data and Simulations

Fig. 20: Plots 20(a) and 20(b) show the calibrated results of the MRED simulations for the entire 127-stage shift register [MCC$^+$05, PRS$^+$07], the data for which is shown in Fig. 15. In each case the open symbols are the data from Fig. 15 and the closed symbols are the derived simulation results from output similar to that shown in Fig. 19.

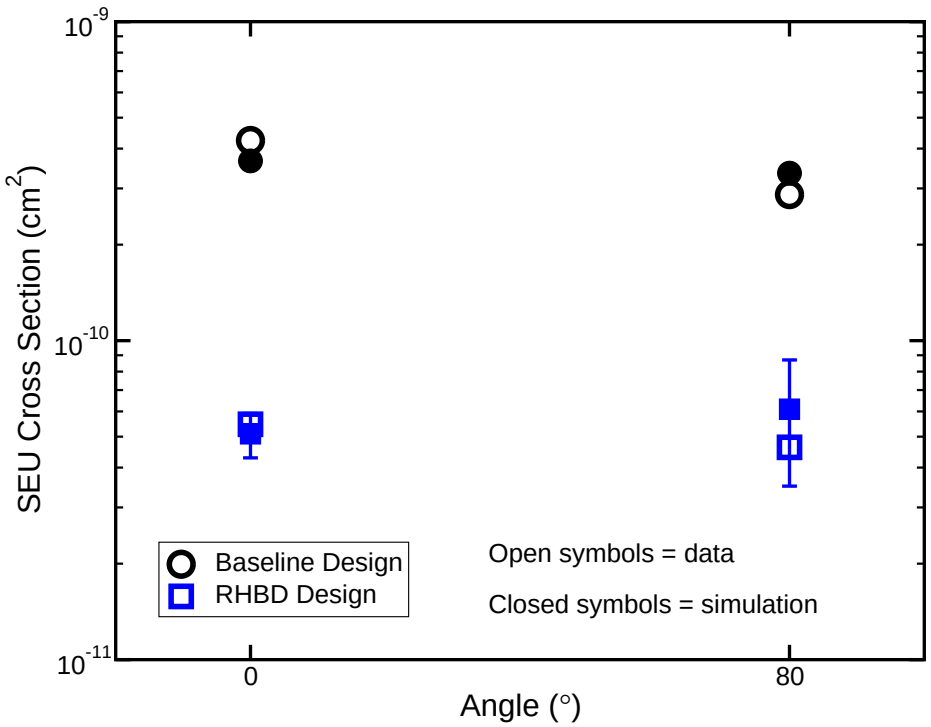

Fig. 21: A comparison between the proton data from Fig. 9 and simulation results based on the model described in Chapter III, which was calibrated to heavy ion data. The strong agreement shown above was obtained by simply changing the particle and energy in the simulation; no further adjustments were made. The open symbols are data based on the average across data rate from Fig. 9 and the solid symbols are simulation results using the response model. Error bars, shown if they are bigger than the data marker, are $\pm 1\sigma$ statistical errors.

These data were taken on the baseline and RHBD shift register designs at several different data rates at normal incidence and a grazing angle. The full data set is plotted in Fig. 9. For reference, the baseline design is the nominal switching architecture from [MCC+05] and the RHBD design is the dual-interleaved architecture from [MCC+05]. The test was conducted using the CREST on-board data and clock generation, but the events were recorded using an external Anritsu MP1764C error detector, which is part of a bit error rate test system. This data set is consistent with other SiGe HBT high-speed proton tests [RMP+03, HCJ+06]. The cross section is approximately constant across different data rates. This data set can now be used to check the proton response

of the model developed in the previous section. These modeling results are shown in Fig. 21. The data shown in Fig. 21 are the average cross section across data rate since the simulation model cannot take data rate into account, something that is the subject of current investigations.

As in previous modeling scenarios [WWS$^+$07], the calibrated heavy ion model was validated against proton data by only a change of particle and energy in the simulation environment. The strong match between simulation and data validates a larger portion of the model's acceptable parameter space, making it usable for environments with large proton fluxes. These simulation results were obtained from the model calibrated with heavy ion data only; no further adjustment was required.

Event Rate Calculations

MRED, used for the modeling throughout Chapter III, has the ability to import and sample across pre-defined particle flux spectra [RWS$^+$06, RWM$^+$07]. CREME96 environment models [TAJB$^+$97b, TAJB$^+$97a] were used to generate the particle flux spectra for the geosynchronous (GEO) and low-earth orbit (LEO) environments, but the IRPP model implemented on the CREME96 website was not used to perform the rate calculations. Both of the environments were solar minimum/quiet conditions, included available ion species from $1 \leq Z \leq 92$, and assumed 100 mil of aluminum shielding. The LEO spectra were for the space station orbit, which, according to CREME96, is at an inclination of 51.6° and an orbital radius of 500 km. The rate prediction methodology used to carry out the computations is described in [RWS$^+$06, RWM$^+$07, PRS$^+$07].

The environment computations for the baseline and RHBD designs used the simulated energy deposition from approximately 5×10^8 individual events with a hadronic cross section bias factor of 75. The bias factor serves to reduce the variance for very rare events by increasing their occurrence in a statistically well-defined manner. In previous cases [RWS+06], the bias factor was set to 200. However, if the bias factor is set too high, too many primary particles are consumed in nuclear reactions, artificially depleting the transmitted flux on the backside of the target, which is non-physical. The target, shown in Fig. 18, is large and quite thick, about 110 μm $\times$ 85 μm $\times$ 75 μm, so backside flux depletion is an issue. All ions simulated were incident on the target uniformly over 4π steradians for both GEO and LEO environments.

The event rates for both GEO and LEO environments are plotted in Figs. 22(a) and 22(b). The rates shown for each ion in the environmental spectrum have been reverse integrated, from right-to-left, so that the total event rate for each design, at a particular critical charge, is that rate or less.

There is a $1.6x$ to $6.2x$ difference between the total rate for the baseline and RHBD designs due to the higher critical charge of the RHBD design. Simulations suggest, though do not prove, that the dominant contribution to each of the four rate curves shown comes from $25 \leq Z \leq 30$, which are the elements manganese, iron, cobalt, copper, and zinc. This large contribution occurs because many of these impinging ions will stop within the sensitive volumes, giving up all their energy in critical regions. This is compounded by the significant iron flux. The contributions of these five ions approach the contributions from the other 81 ions that were simulated; this is true for both GCR

and LEO event rates. However, in LEO orbits, the flux of these key ions is much lower due to natural magnetic shielding, leading to the lower event rate.

The baseline and RHBD curves shown in Figs. 22(a) and 22(b) appear in a counterintuitive way since the rate curve for the RHBD device is above the baseline device. However, the RHBD device has a larger subcollector junction area by a factor of approximately 1.6 since it is a bigger device relative to the baseline design. The rate curve of the RHBD design is higher since the area of the subcollector junction plays a significant role in the device's response to charge liberated from ionizing radiation.

The environment-based SEU rates presented are to be interpreted as event rates, not bit error rates. The energy deposition response model developed in Chapter III makes no attempt to derive temporal or event-composition information—*i.e.*, zero-to-one, one-to-zero, flatten-to-one, flatten-to-zero, mangle, or any of the other error types defined in Table 1 [SKM$^+$06]. The model neither calculates the number of upset bits in the event nor yields any information regarding preferences for burst error modes. However, the model makes the most accurate representation to date by providing an energy deposition response behavior consistent with device geometry and the charge collection mechanisms present in this type of process technology.

The present modeling approach is the first and necessary step towards solving the more intricate, time-dependent problem, which requires the energy deposition model to adapt its properties and volume-to-volume logic dynamically. Such a model would also have to be tied to a circuit-level or TCAD simulator with compact models in order to produce burst error information reliably. In addition to those non-trivial steps, there is a great need for experimentally measured radiation-induced current transients

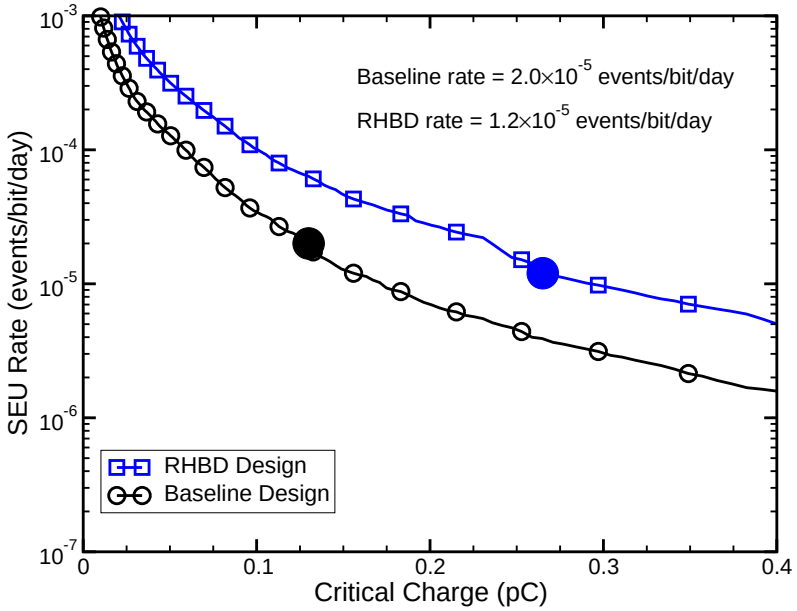

(a) Geosynchronous event rate calculation

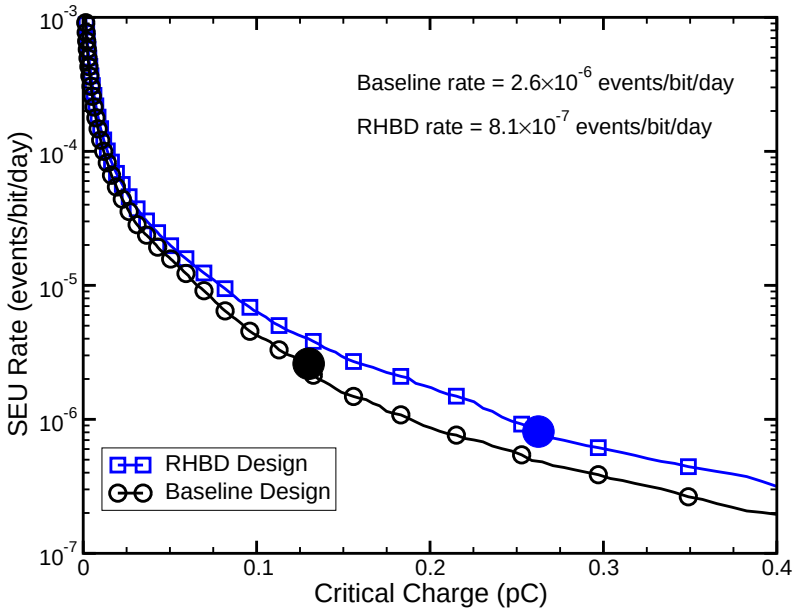

(b) Low-earth orbit rate calculation

Fig. 22: These figures show the simulated event rates for the baseline and RHBD shift register designs. The LEO event rate is approximately one order of magnitude below the GCR event rate due to sensitivity dominated by direct ionization and the reduced flux of many significant contributors. There is a 1.6x to 6.2x difference between the event rates for the baseline and RHBD designs. The data markers have been thinned to aid viewing. The large markers show where the rate was evaluated based on the critical charge derived from the fit shown in Figs. 20(a) and 20(b)—0.13 pC and 0.26 pC.

in SiGe HBT BiCMOS process technology. Current commercial TCAD simulators have been successful at modeling the total collected charge from radiation events [VNK+03, CKS+06, PRS+06, SBC+07, MRP+08], but there are no experimental data with which to compare the induced current transients. It is believed that the present TCAD radiation-induced transients are inaccurate in some regimes.

CHAPTER IV

TRANSIENT MEASUREMENT EXPERIMENTS

Introduction

All of the Single-Event Effects (SEE) that people are studying today can be traced back to the generation and collection of radiation-induced charge at the transistor level. For the past twenty-six years, people have been measuring radiation-induced charge collection at the device level – see, for example [MO82, CKM$^+$89, HWJP91, HJWH92, MWK$^+$93, HDS$^+$93, MWB$^+$96, SWS$^+$98, LHO$^+$02, RMP$^+$03, VNK$^+$03, PRS$^+$06]. These data provide useful quantities, like total collected charge (Q_{coll}), which are also often accompanied by positional data. With the exception of a few practitioners, most of these measurements examined total collected charge, not the radiation-induced current transient itself. However, a small group of people undertook the challenge of measuring single-event, radiation-induced current and voltage transients [WBM$^+$86, WBB$^+$87, WBB$^+$88, MWK$^+$93, MWB$^+$96, MWK$^+$96, HION01, FCGM$^+$02, MBK$^+$04, LHO$^+$05, LHOI05, OHL$^+$05, FCPM$^+$06, FCPG$^+$06].

These measurements have been possible through the use of high-bandwidth, possibly superconducting, sampling oscilloscopes [HS83, GOSO84, HS84, Fle85, SMD$^+$85, WBM$^+$86, WBB$^+$87, WBB$^+$88, HEF$^+$89, MWK$^+$93, SWS$^+$98, SWS$^+$99], with analog front-ends up to 70 GHz – note particularly the work of Wagner and McMorrow. These time-domain transient measurements are a superset of the time-integrated charge collection measurements and have traditionally been made with pulsed laser irradiation sources or focused heavy ion microbeams.

In recent years, with the advent of advanced triggering technology, high-resolution and high-bandwidth real-time digital storage oscilloscopes (DSO) have begun to make possible the time-domain measurement of non-repeating, picosecond current and voltage transients [LHOI05, FCPM+05, FCPM+06, FCPG+06, MFCA+06, LSV+07, LCS+08]. Sampling oscilloscopes are no longer required for most applications, but their higher bandwidth is sometimes an advantage for applications where they can be used. Since real-time DSOs do not require a repeatable, phase-stable signal and an external triggering source, transient measurements have now progressed beyond the limitations of pulsed laser sources and heavy ion microbeams – it is now possible to measure radiation-induced transients at broadbeam heavy ion, proton, and neutron facilities, though not all of these experiments have been demonstrated to date [FCPG+06, MBM+07].

In the past, all these types of time-domain measurements were extremely difficult, if not impossible, and were largely unneeded or ignored, leading to deficiencies in this type of testing. With the advent of high-speed digital, analog, and mixed-signal circuits being deployed in extreme radiation environments or situations that require high reliability, and the pervasive use of device- and circuit-level simulation, much more work has to be done to tackle time-domain single-event measurements. Nowhere is this more true than for SiGe HBTs.

In the late 1990s, the NASA Goddard Space Flight Center, the Georgia Institute of Technology, and Auburn University began to study the single-event response of IBM's Silicon-Germanium Heterojunction Bipolar Transistor (SiGe HBT) BiCMOS process technology [MCC+00]. This technology study included an extensive battery of heavy

ion microbeam tests to characterize charge collection mechanisms [VNK+03, RMP+03, PRS+06, SBC+07, MRP+08]. These tests were performed across all available IBM technology nodes, which, as of 2007, included 5HP/AM, 7HP and 8HP SiGe BiCMOS technologies[1]. While these previous time-integrated charge collection measurements have provided valuable position-dependent charge collection information useful for determining sensitive volume structures for simulation analysis of complex radiation interactions, they fail to capture temporal information that is vital to circuit and system analysis.

Single-event upsets in high-speed ($\geq$ 1 GHz) SiGe HBT current mode logic shift registers present one of the most obvious reasons to pursue time-domain charge collection measurements [MCC+05, SKM+06]. The bit error experimental data acquired over the past seven years [MCC+00, RMP+03, MCC+04, MCC+05, SKM+06, PRS+07] contain detailed information about not only bit error cross sections, but also error length and composition – *i.e.*, reveals flatten to 0, flatten to 1, single and multiple pattern shifts, etc., as shown in Table 1. This same argument could be applied to any CMOS or SOI technology utilized for clocked binary applications.

Present time-integrated charge collection measurements, via laser or microbeam testing, have been useful for developing event rate models [PRS+07] – where an event is defined as one or more bit errors induced by a single event. These models can predict the number of events that will occur, but they make no assertions about error length or composition. Time-domain experimental data are needed to advance this work.

[1]Other SiGe HBT process technologies have been investigated, including Jazz, National Semiconductor, and IHP.

Another shortcoming of time-integrated charge collection measurements is their lack of applicability in calibrating single-event technology computer-aided design (TCAD) simulations. Charge collection data can be compared to the integrated terminal current in a TCAD simulation to verify the model [VNK+03, PRS+06], but again, time-domain information is lost, marginalized, or ignored. However, since no better solution exists, current pulses derived from mixed-mode TCAD continue to be the best way to obtain calibrated current sources for SPICE simulations [AWM+06, AMB+07].

Using this derived temporal information in circuits with time constants much larger than the time constant of a representative radiation-induced current or voltage transient is an appropriate approximation, but many circuits operate on time scales comparable or faster than the radiation-induced transients, making the time profile of the transient one of the most critical components in any simulation. The breakpoint for this occurs when clock speeds approach 1 GHz, which is shown in linear bit error scaling in the data of Figs. 10 and 11.

Semiconductor process scaling has resulted in devices that are now much smaller than the characteristic size of radiation events. This development has led to many non-linear and proximal SEEs including electrostatic potential modification at-a-distance and charge sharing between neighboring transistors [AWM+06, AMB+07]. While time-integrated charge collection measurements can provide qualitative assessments of such effects, propagating these effects from the device to the circuit or system level requires time-domain information for either direct substitution into SPICE simulations or calibration of the actual current transient predicted by mixed-mode TCAD simulations.

High-Speed Packaging

One of the most critical aspects of high-speed transient measurement experiments is the ability to get the high-speed signal from the device under test (DUT) into the oscilloscope; Wagner, *et al.* were the first to master this skill [WBM+86]. The DUT is placed on a ground plane, the pads bonded to microstrip transmission lines, and then connected to coaxial launchers at the edge of the ground plane. The dominant parasitics of the system are contained within the die pads, the bondwire, and the coaxial launcher. These parasitics must be understood in order to obtain accurate results. For further information on this topic and other related topics, see, for example [JG03, Poz05].

Many experiments have copied Wagner's original high-speed package design because of its simplicity and effectiveness [MWK+93, FCPG+06, PRM+08]. It allows the bondwires to be short, on the order of 1 mm, and the microstrip transmission lines and coaxial launchers provide a matched impedance environment to prevent excessive power loss. The high-speed package used in this work is shown in Figs. 23(a) and 23(b). There were a few design modifications made to the package to accommodate DUT and microstrip line constraints, but the design is largely unchanged from Wagner's original. The design blueprint used here came from Sandia National Laboratories and the Naval Research Laboratory.

This design used approximately 0.7 mm, 1 mil gold bondwires, which have an inductance of approximately 0.5 nH[2]. The bondwires were connected to 50 Ω microstrip transmission lines. The microstrips are 500 mil long, 100 mil wide with a 9.57 mil gold trace, and a 10 mil alumina substrate plated with gold. The microstrips were connected

[2]The inductance rule of thumb for 1 mil gold bondwire is 1 nH/mm.

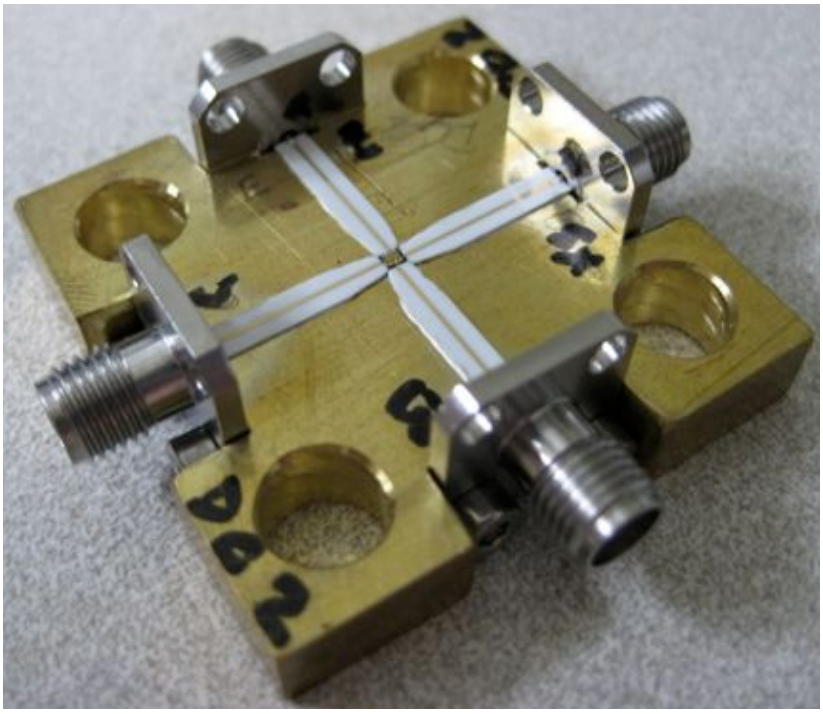

(a) Top-view of high-speed package

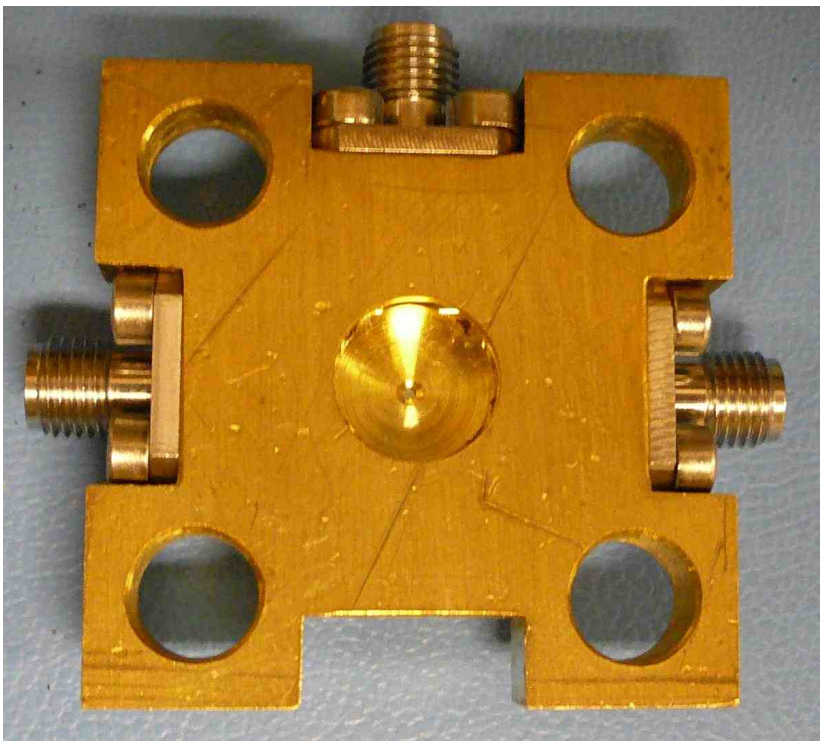

(b) Backside-view of high-speed package

Fig. 23: Topside and backside views of Vanderbilt's implementation of R. Wagner's high-speed package. This basic design has been used in the past [WBM+86, MWK+93, FCPG+06], but several modifications were made to this design to accommodate DUT and microstrip line constraints.

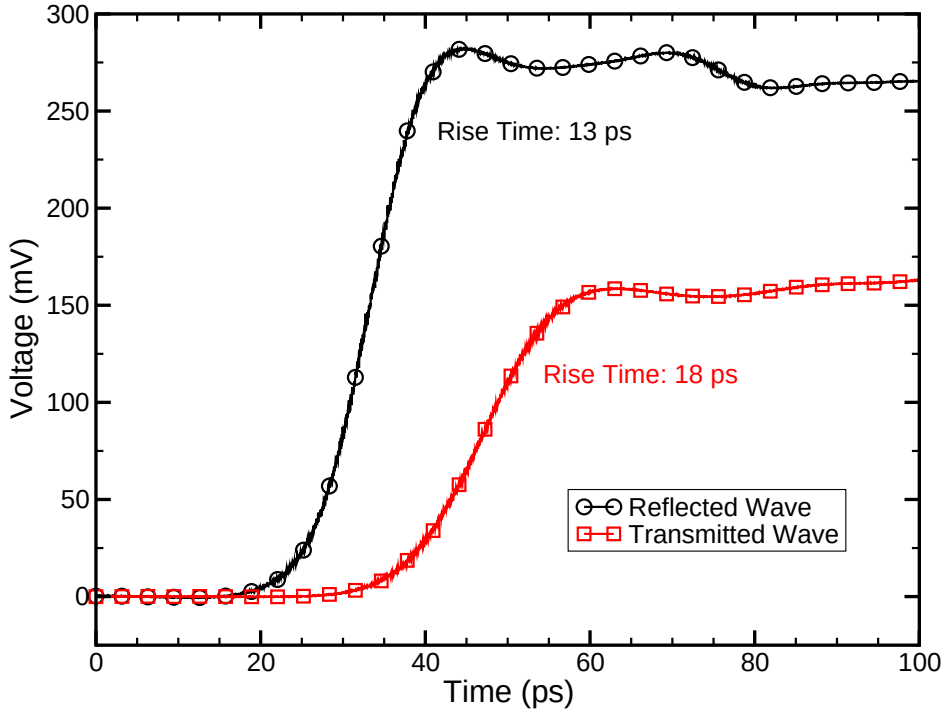

Fig. 24: Incident and transmitted step responses for an IBM 5AM AC-thru test structure using a Tektronix DSA8200 sampling oscilloscope with the 80E10 50 GHz TDR/Sampling module. The incident step is 250 mV speced at 12 ps, measured to be 13 ps. The transmitted response had a risetime of 18 ps and underwent an attenuation of -2.3 dB. The real response characteristic of interest is the risetime difference. While the transmitted step shows an attenuation of -2.3 dB, the actual attenuation value is dependent on the placement of the RF ground-signal-ground probe tips. This value is an average of sorts and could be smaller or larger depending on the experimental setup.

to the coaxial launchers via stress relief tab contacts that mated to the inner conductor of the launcher. The launchers themselves were 2.9 mm coaxial designs, which are rated to 40 GHz.

To test the parasitics of the DUT and package, a set of time domain reflectometry (TDR) measurements were performed on the high-speed package connections and an AC-thru DUT structure. The AC-thru DUT is designed to characterize the in-situ parasitics of AC characterization test structures for deembedding purposes – see, for example [Kol00, Cre06b, CLP+08]. However, here it is being used to characterize the

effect of process features on the transmission of a fast edge, intended to replicate a radiation-induced current transient. Since the AC-thru DUT has a 150 μm pitch ground-signal-ground pad configuration, an RF probe station was used to make the required measurements. The results of the AC-thru measurements are shown in Fig. 24. Based on the data in Fig. 24, the estimated bandwidth of the AC-thru DUT is 19 GHz using Eq. 8, where BW is the bandwidth and t_{r} is the 10%-90% risetime. This formula is derived from $H(\omega) = e^{-\frac{\omega^2}{\sigma^2}}$, which is the frequency response of a Gaussian system.

$$BW \cdot t_{\mathrm{r}} \approx 0.34\,. \tag{8}$$

The impedance matching of the high-speed package components – microstrips, stress relief contacts, and launchers – is important to ensure minimal power loss and efficient signal coupling into the coaxial transmission lines. The impedance of the system can be measured using TDR. TDR is commonly used to measure the characteristic impedance of a transmission line or to quantify reflections caused by discontinuities along or at the termination of a transmission line. TDR has the advantage that it can measure impedance mismatches as well as parasitic inductances and capacitances as they reside in the circuit; an LCR meter cannot do this.

The high-speed package underwent TDR testing to measure any impedance mismatches along the transmission route from the oscilloscope, through the 2.9 mm (40 GHz) coaxial cable, the high-speed package launcher, the microstrip, and finally the bondwire. If the impedance is matched, the TDR waveform rises and then maintains a constant value at the characteristic impedance of the transmission line, which is 50 Ω in this case. Excess series inductance appears as a positive spike and excess shunt

capacitance appears as a negative spike. In Cartesian form, impedance is defined by

$$Z = R + jX\,, \tag{9}$$

where the real part of the impedance is the resistance, R, and the imaginary part, X, is the reactance. The term impedance was coined by Oliver Heavyside in the late 1880s. If $X \geq 0$, then the reactance is said to be inductive; if $X = 0$, then the impedance is purely resistive; and, if $X < 0$, then the reactance is said to be capacitive. Inductive reactance, X_{L}, is defined by

$$X_{\mathrm{L}} = 2\pi f L\,, \tag{10}$$

where f is the signal frequency and L is the inductance. Capacitive reactance, X_{C}, is defined by

$$X_{\mathrm{C}} = -\frac{1}{2\pi f C}\,. \tag{11}$$

The TDR characterization of the base and collector terminals of a fully-built package is shown in Fig. 25. The incident step is shown on the left at 0.4 ns. The flat section after the incident step is the 36 in transmission line, which has a constant impedance that lasts for approximately 3.5 ns. This measured length matches the $0.87c$ velocity of propagation for this particular transmission line. The positive spike after 4 ns is the bondwire inductance and the negative spike immediately following it is the DUT pad capacitance. Note that the collector capacitance is larger due to the fact that the collector pad is tied to the collector-substrate junction, which has a much larger area than the base-collector junction. The overshoot at 0.4 ns and subsequent steady-state impedance of 47 Ω, instead of the predicted 50 Ω, is likely caused by the superposition of multiple reflections from the TDR step-generator and the 2.9 mm coaxial cable interface, which

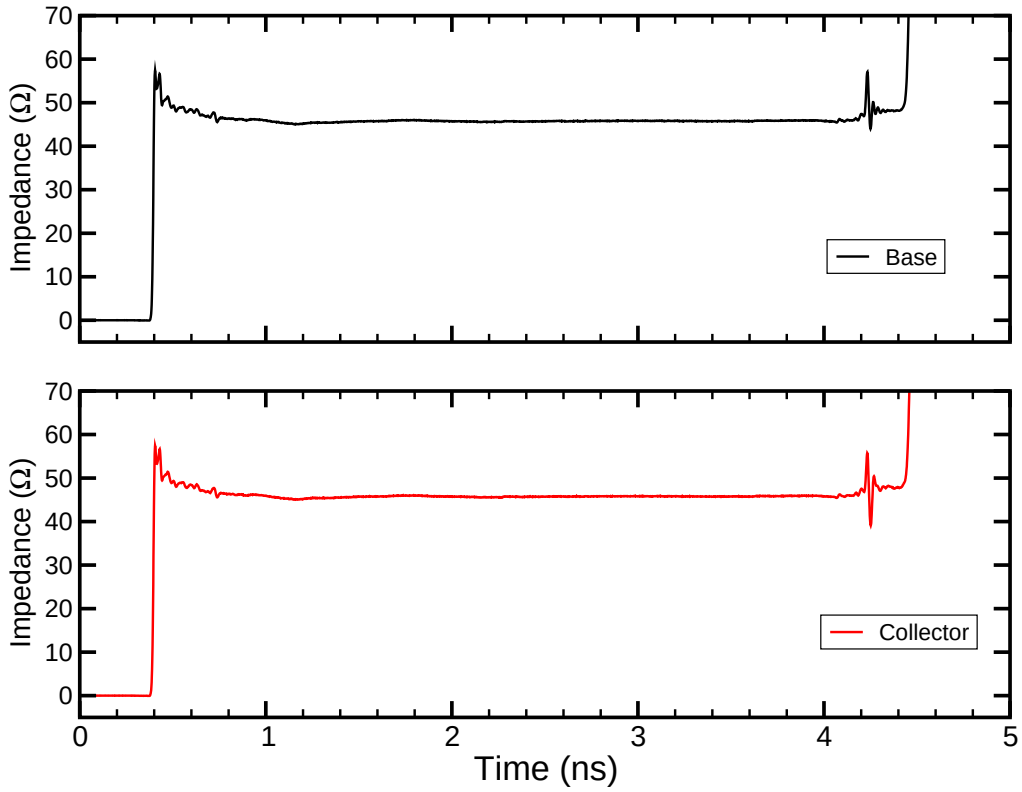

Fig. 25: TDR characterization of the base and collector terminals of the Vanderbilt high-speed package. The positive spike after 4 ns is the bondwire inductance and the negative spike immediately following it is the DUT pad capacitance. The 0.5×2.5 μm^2 IBM 5AM SiGe HBT was unbiased during this experiment.

includes a 1.85 mm-to-2.9 mm adapter. The true impedance algorithm can be calculated using an impedance peeling algorithm, also known as an inverse scattering algorithm [OL99]. However, this was not necessary for the present analysis. Since the reactance of the package is minimal, device loading can be assumed to be purely resistive as a first approximation.

TDR can be used to calculate the shunt capacitance and series inductance between two transmission lines. The reflected TDR waveform has to be scaled so that it has an incident step height of 1, often plotted as the quantity ρ. Then the area of the impedance discontinuity is determined by integration. The total area is then scaled by

the characteristic impedance of the target system. For capacitance, the equation is

$$C = -\frac{2}{Z_0} \int_0^{+\infty} \text{Reflected\_Wave}\, \mathrm{d}t\,, \tag{12}$$

where Z_0 is the characteristic impedance of the transmission lines. The form for inductance is similar, but the scaling factor is different. Instead,

$$L = 2Z_0 \int_0^{+\infty} \text{Reflected\_Wave}\, \mathrm{d}t\,. \tag{13}$$

The only caveat of this procedure is that the impedance mismatches must be sufficiently far apart so that they can be cleanly integrated. The voltage step travels at a finite speed down and back the transmission system. The 2.9 mm coaxial cables used here have a velocity of propagation of $0.87c$, which means that signals travel at 0.26 mm/ps. The minimum reflected risetime is 15 ps, so the discontinuities have to be about 5 mm apart to be completely distinguishable. The discontinuities in Fig. 25 are not far enough apart to permit an ideal computation, but the approximate solutions to Eqs. 12 and 13 suggest a die pad capacitance of 60 fF and a bondwire inductance of 0.2 nH. Both of these values are consistent with the dimensions, electrical characteristics of the physical system, and engineering approximations.

Two-Photon Laser-Induced Radiation Transients

SiGe HBTs are often employed in high-speed applications, so knowledge of radiation-induced current-transient characteristics is a prerequisite for accurate modeling of circuit- and system-level effects, such as burst errors. The lack of advanced bipolar compact model support in commercial technology computer-aided design (TCAD) tools makes actively-loaded mixed-mode simulations unnecessarily complex. Furthermore, it

is difficult to measure current transients within a circuit, whereas irradiating a single SiGe HBT is feasible. Sutton's work in 2006 showed that hitting a single SiGe HBT in a high-speed IBM 5AM SiGe HBT shift register chain using single-photon absorption was sufficient to produce burst errors [SKM+06]. The experiments described here examine two-photon absorption current transients from a passively-loaded single SiGe HBT with the intent of accurately measuring single-event current transients.

To date, commercially-available, mixed-mode, drift-diffusion based TCAD simulations with passive loading were the only means to calculate SiGe HBT current transients due to the lack of bipolar compact model support beyond SPICE Gummel-Poon [NCS+00, NKC+01, NKC+02, VNK+03, PRS+06]. These simulation results predicted collector current transients in excess of a nanosecond with fast risetimes and long tails, which present a SEU hazard for applications operating at Gbit/s data rates where the bit period is less than 1 ns. The existence of such nanosecond transients was confirmed by experimental bit error rate testing with broadbeam heavy ions [MCC+05], single-photon absorption [SKM+06], and, to some extent, protons [PRS+07].

TCAD simulations need to be calibrated with experimental data to ensure that extrapolated calculations are valid [VNK+03, PRS+06]. Before this work, there were no published examples of experimentally-measured SiGe HBT current transients. Therefore, many TCAD results were presented in terms of integrated charge vs. time because spatially correlated heavy ion microbeam charge collection data were available [VNK+03, PRS+06, SBC+07, MRP+08]. The IBM 5AM SiGe HBT two-photon absorption current transients presented here confirm and explain important charge collection and transient generation mechanisms in SiGe HBTs. Neither broadbeam particle testing nor

pulsed laser testing reproduce the space environment; they are approximations to on-orbit conditions. Laser testing is less expensive than broadbeam heavy ion and proton testing and offers more control over the radiation source and the device under test (DUT) during the experiment. As such, it is a desirable screening method for single-event effects.

Two-photon absorption (TPA) carrier generation is a recent pulsed laser technique ideally suited to study single-event effects in SiGe HBTs [MLM+02, JPF+08]; it uses sub-bandgap optical wavelengths. TPA is closely related to the original technique of single-photon absorption (SPA) carrier generation [MBM+94, MMB+00, PFL+00], which uses above-bandgap optical wavelengths. In either case, the technique is based on the excitation and generation of free carriers in the semiconductor lattice using a micrometer-sized pulsed optical beam. However, the fundamental absorption mechanism is different for SPA and TPA.

Carrier generation for SPA laser irradiation is governed primarily by Beer-Lambert absorption, such that each absorbed photon generates a single electron-hole pair, and the injected carrier density decreases exponentially from the laser interface with the semiconductor surface. In equation form, Beer-Lambert absorption has the following form

$$I(z) = I_0 \exp(-\alpha z)\,, \tag{14}$$

where I_0 is the intensity entering the material and α is the linear absorption coefficient [MBM+94]. Fig. 26 shows the room temperature absorption spectrum of silicon in the visible and near-infrared regions. 590 and 800 nm are common wavelengths for SPA experiments.

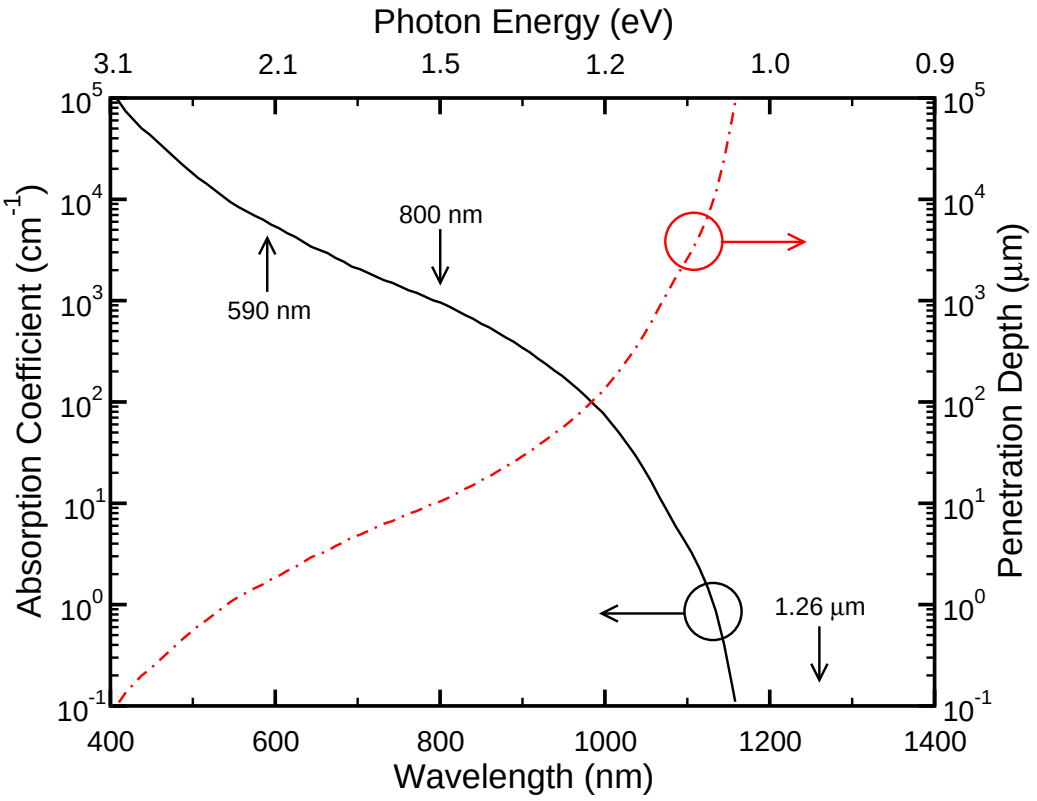

Fig. 26: Room temperature absorption spectrum of silicon in the visible and near-infrared regions [MMQR59, Sch81, MLM+02]. Common laser wavelengths for experiments are marked. The red dashed line shows the penetration depth of the photons neglecting higher-order processes, which is the inverse of the absorption coefficient. Photon energy is related to wavelength via $E = (hc)/\lambda$, where $hc = 1240$ eV $\cdot$ nm.

The intensity of the beam as it passes through the material has a radial and temporal dependence in addition to the longitudinal dependence expressed in Eq. 14. The beam radius is given by

$$w^2(z) = w_0^2 \left[1 + \left(\frac{\lambda z}{\pi w_0^2 n} \right)^2 \right], \tag{15}$$

where z is the propagation distance into the material, w_0 is the the $1/e$ radius of the laser spot at the surface, λ is the wavelength, and n is the index of refraction of the target material [Yar75]. The temporal dependence does not have a set form, but is usually modeled as a Gaussian.

In TPA, the laser wavelength is chosen to be less than the bandgap of the target semiconductor. For the experiments discussed here, the wavelength is 1260 nm, shown in Fig. 26. The photons are generated and dumped in high peak power femtosecond pulses. Because they have wavelengths less than the bandgap, no carriers are generated via optical absorption at low light intensities. This means that the penetration depth of the optical beam is very large. However, a sufficiently high intensities, the material can absorb two photons simultaneously to generate a single electron-hole pair [GM31].

Since the material is transparent to the incident optical radiation in the linear absorption regime, the exponential attenuation described in Eq. 14 does not occur. TPA carrier generation is proportional to the square of the laser pulse irradiance, so carrier generation is only significant in the focal region of the laser beam, where the intensity is sufficient. This is the key characteristic of TPA. It enables the deterministic injection of charge at any depth in the material, in addition to lateral positioning, by simply changing the focal location. Circuits and devices are usually irradiated through the backside, with the beam penetrating the polished backside of the semiconductor wafer. This eliminates one of the roadblocks of SPA pulsed laser irradiation, which has to be done through the topside of the DUT and therefore has to contend with metal in the back-end-of-line, which photons cannot penetrate.

TPA is governed by three coupled differential equations that relate pulse irradiance, phase, and free carrier density as a function of position and time. The equations are generally applicable to pulse propagation and carrier generation in semiconductors – *i.e.*, they also apply to SPA [VVW$^+$85, BBM$^+$86, SSH$^+$91]. These relations are given in

Eqs. 16, 17, and 18.

$$\frac{\mathrm{d}I(r,z)}{\mathrm{d}z} = -\alpha I(r,z) - \beta_2 I^2(r,z) - \sigma_{\mathrm{ex}} N I(r,z)\,, \tag{16}$$

$$\frac{\mathrm{d}\Phi(r,z)}{\mathrm{d}z} = \beta_1 I(r,z) - \gamma_1 N(r,z)\,, \tag{17}$$

$$\frac{\mathrm{d}N(r,z)}{\mathrm{d}t} = \frac{\alpha I(r,z)}{\hbar\omega} + \frac{\beta_2 I^2(r,z)}{2\hbar\omega}\,. \tag{18}$$

In Eqs. 16-18, $I(r,z)$ is the pulse irradiance with units of $\mathrm{W/m^2}$, $\Phi(r,z)$ is the phase, $N(r,z)$ is the density of free carriers with units of $(\mathrm{eh\,pairs})/m^3$, α is the linear absorption coefficient with units of meters shown in Fig. 26, β_2 is the two-photon absorption coefficient that is proportional to the imaginary part of the third-order nonlinear susceptibility $\chi^{(3)}$, σ_{ex} is the absorptivity of laser-generated free carriers, β_1 is proportional to the real part of $\chi^{(3)}$, γ_1 describes the refraction due to free carriers, and r and z are the coordinates for three-space position [MLM$^+$02].

While Eqs. 16 and 17 are important considerations, basic insight to the TPA process lies within Eq. 18, which is enough to carry out simple calculations. Since TPA is a nonlinear process and linear absorption is neglected, α is therefore equal to 0, eliminating the first term on the right-hand side of Eq. 18. The $2\hbar\omega$ term in the remaining denominator accounts for the fact that each electron-hole pair requires the absorption of two photons simultaneously, where $\hbar\omega$ is the photon energy. The value of the nonlinear absorption coefficient has to be measured. It depends on wavelength and the dopant density of the semiconductor material. Values for β_2 with the laser system used in these experiments were recently determined and are plotted in Fig. 27 [LMM07]. The point of interest is for p-type silicon, doped to 1×10^{15} $\mathrm{cm^{-3}}$ with boron, at 1260 nm. This value is 0.27 cm/GW.

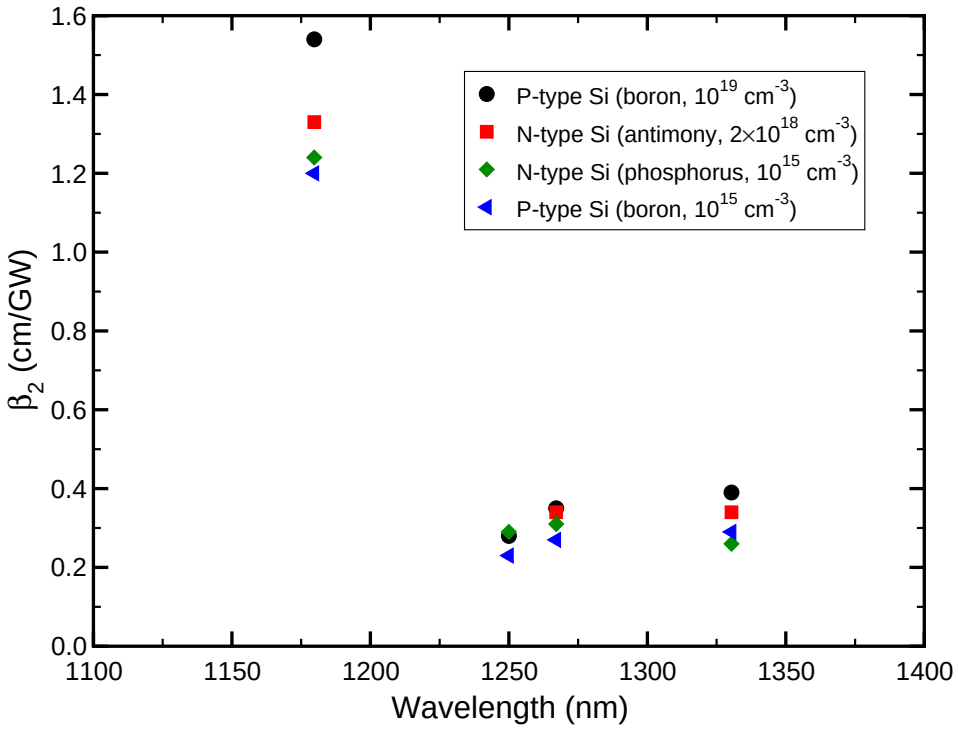

Fig. 27: Two-photon absorption coefficient extracted from Z-scan data, after Lotshaw, *et al.* [LMM07]. The value of interest for these experiments is at 1260 nm for boron-doped p-type silicon at 1×10^{15} cm^{-3}.

The laser beam is taken to be Gaussian, where the pulse irradiance has a radial dependence given by

$$I(r,z) = \frac{2P}{\pi w^2} \exp\left(-2r^2/w^2\right) , \tag{19}$$

where the z-dependence of the radius is given by Eq. 15. z is the longitudinal position relative to w_0, which is the beam radius at the waist (focal point). When nonlinear absorption is the only irradiance loss mechanism in the material, the irradiance as a function of z is given by

$$I(z) = \frac{I_0}{1 + \beta_2 I_0 z} . \tag{20}$$

Therefore, the TPA carrier generation density is given by integration of Eq. 18 assuming

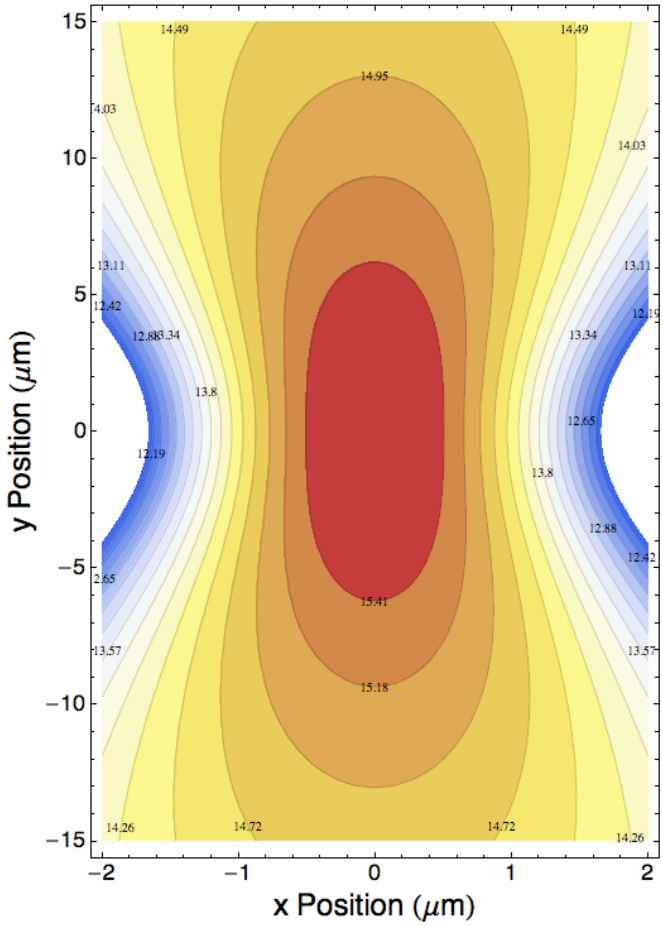

Fig. 28: TPA pulse irradiance for a 120 fs, 1 nJ pulse at 1260 nm in silicon focused to a beam waist diameter of 1.6 μm. The contours are logarithmic in units of W/m^2 with a peak above 2×10^{15} W/m^2. y-position is depth in the sample and x-position is the transverse position. The distribution is ellipsoidal and so is cylindrically symmetric. Note the scale difference in ordinate and abscissa. The true aspect ratio is more than 7:1.

$\alpha = 0$:

$$N_{\mathrm{TPA}}(z,t) = \frac{\beta_2}{2\hbar\omega} \int_{-\infty}^{+\infty} I^2(z,t)\, \mathrm{d}t\,, \tag{21}$$

where $I(z,t)$ is from Eq. 20, including the longitudinal and radial dependencies from Eqs. 15 and 19.

Assuming typical pulse parameters – $\lambda = 1260$ nm, a pulse energy of 1 nJ, a pulse width (FWHM) of 120 fs, a focal size of 1.6 μm, and a 3.51 index of refraction for silicon – the pulse irradiance and carrier generation distributions can be calculated. The

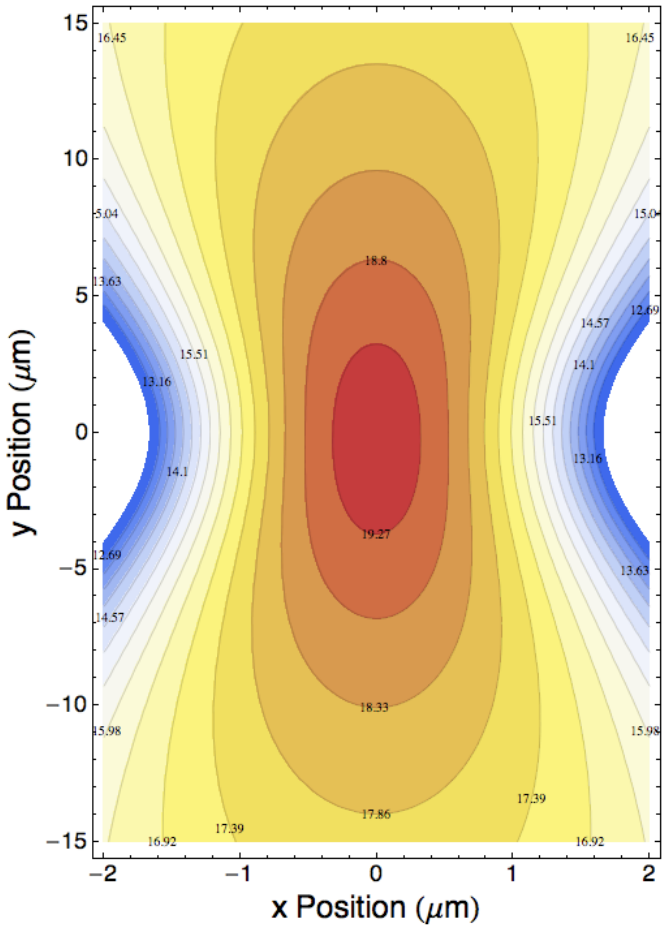

Fig. 29: Photogenerated carrier distribution for TPA laser irradiation in silicon. The contour plot is in units of $\#/(\mathrm{cm}^3)$, with a peak above 1.9×10^{19} cm^{-3}. y-position is depth in the sample and x-position is the transverse position. The distribution is ellipsoidal and so is cylindrically symmetric. Note the scale difference in ordinate and abscissa. The true aspect ratio is more than 7:1.

irradiance for this pulse is shown in Fig. 28, where the contours are logarithmic with units of $\mathrm{W/m}^2$. The peak irradiance is above 2×10^{15} $\mathrm{W/m}^2$. Using the nonlinear absorption coefficient, β_2, the irradiance can be converted into a distribution of generated electron-hole pairs after incorporating time-dependence.

Eq. 18 describes a position-dependent carrier generation rate with units of $\#/(\mathrm{m}^3 \cdot \mathrm{s})$. This rate is converted to a density by evaluating the integral in Eq. 21 from $-\infty$ to $+\infty$. This integration is done numerically over $\pm 3\sigma$ to produce the logarithmic contour

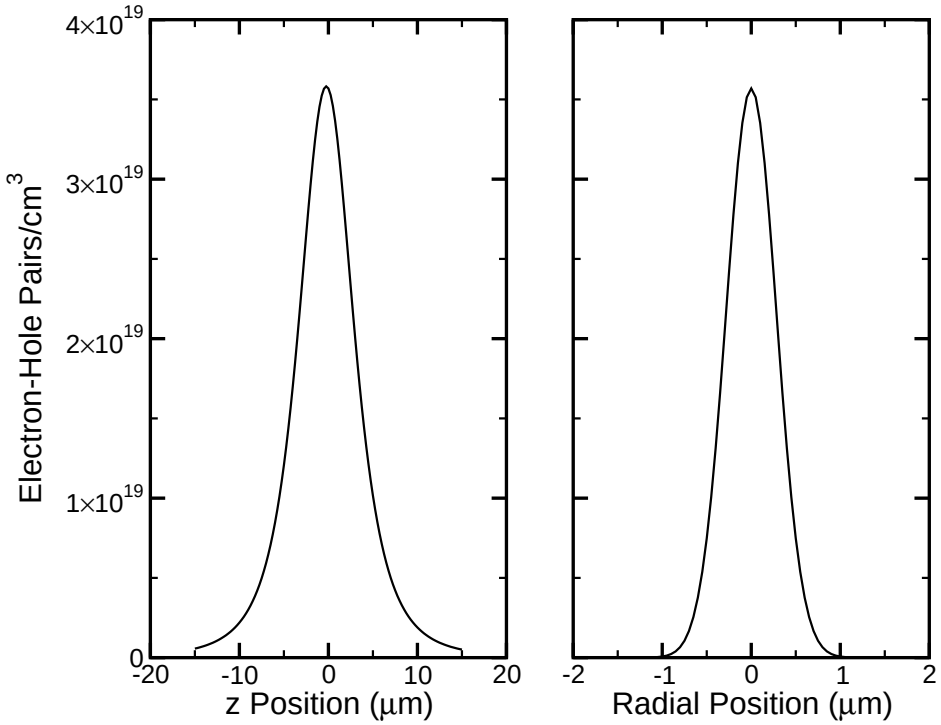

Fig. 30: 2-D plots in z and r for the photogenerated carrier distribution for TPA laser irradiation in silicon. These plots are orthogonal cuts through the center of the contour plot shown in Fig. 29. z-position is depth in the sample and radial position is a slice through the center of the ellipsoid. Note the $10x$ difference in the abscissa scales.

plot in Fig. 29, which is in units of cm^{-3}. 2-D plots of the generated carrier density are shown in Fig. 30. One of the main advantages of TPA pulsed laser irradiation is that this packet of charge can be moved deterministically in three dimensions, a limitation of SPA, which can only be positioned in two dimensions with the depth of penetration controlled by the linear absorption coefficient, α. Since the generated carrier density goes as the square of the laser pulse irradiance, doubling the irradiance quadruples the generated carrier density, enabling a wide range of stimulation.

However, TPA does present issues that can cause problems for certain experiments. The previous calculations neglected nonlinear refraction related to β_1, self-focusing and self-defocusing, free carrier absorption, and optical absorption in heavily

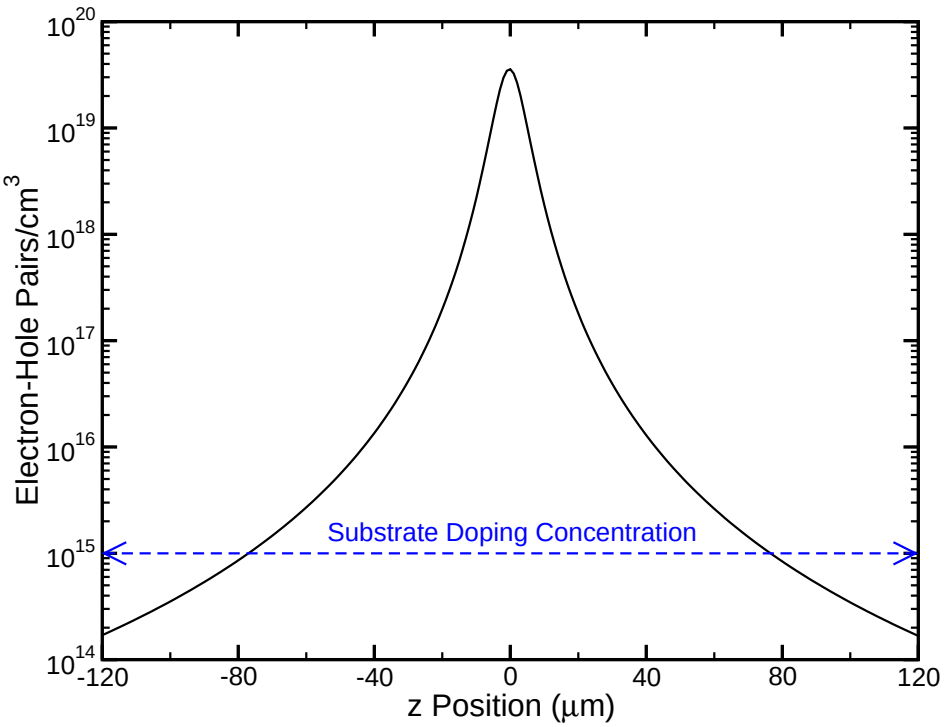

Fig. 31: 2-D plot of the longitudinal TPA carrier density on a logarithmic scale showing that TPA can induce a response from large distances in devices with lightly doped substrates. The IBM 5AM SiGe HBT has a substrate boron doping concentration of approximately 1×10^{15} cm^{-3}. Generated carrier densities above this level will induce a device response. If the pulse irradiance is increased, this effect is exaggerated further.

doped regions. They depended only on the material index of refraction and the focal spot size. Since SiGe HBTs are built on lightly doped p-type substrates and there is nothing to impede carrier generation or current induction, long range current induction is possible. Fig. 31 shows the left chart in Fig. 30 on a log scale. To create a measurable effect, the free carrier density just has to exceed the background doping by a sufficient amount. For the conditions already discussed, this is approximately ± 80 μm vertically from the focal spot. It has already been shown that SiGe HBTs have a sensitive volume structure that extends at least 15 μm into the substrate away from the active junctions. This makes 3-D response mapping difficult since moving further into the substrate does not mitigate device response.

The experimental results presented here were obtained from an IBM 5AM SiGe HBT test structure in the IBM 5AM BiCMOS process technology [CHM$^+$00, NHM$^+$95, AFS$^+$97, CN03]. This technology was chosen due to the large body of published data and simulation results [MCC$^+$00, VNK$^+$03, MCC$^+$05, SKM$^+$06, PRS$^+$06, PRS$^+$07, MRP$^+$08]. The device has a single emitter stripe with dimensions of 0.5 μm by 2.5 μm. The deep trench isolation surrounding the active device has outer dimensions of 6.2 μm by 6.4 μm and inner dimensions of 4.1 μm by 4.3 μm. The depth of the deep trench isolation is between 7 and 8 μm. The n^+/p^- subcollector-substrate junction resides in the area enclosed by the deep trench isolation. There are three p^+ substrate taps for this device, located approximately 9 μm from the outside of the deep trench. All four of the device terminals were connected to individual pads on the die. The major device features are shown in the TCAD cross section of Fig. 1.

The device under test was mounted in a custom broadband 40 GHz package designed for topside and backside laser irradiation as well as heavy ion microbeam irradiation; it is shown in Figs. 23(a) and 23(b). All four device terminals were connected to 40 GHz bias tees with the AC+DC connection facing the device and the AC-only connection facing the oscilloscope. The experiments used a Tektronix 12 GHz TDS6124C real-time digital storage oscilloscope. All transmission lines were 50 Ω, 2.9 mm (40 GHz) coaxial assemblies. The die pads were bonded to the microstrip transmission lines with 1 mil gold bond wires less than 1 mm in length. Each component, including the bulkhead launchers and microstrip lines on the package, were impedance matched and free from most sources of parasitic inductance in order to eliminate measurable capacitive filtering and ringing in the output signal – see Figs. 24 and 25 as well as the associated discussion.

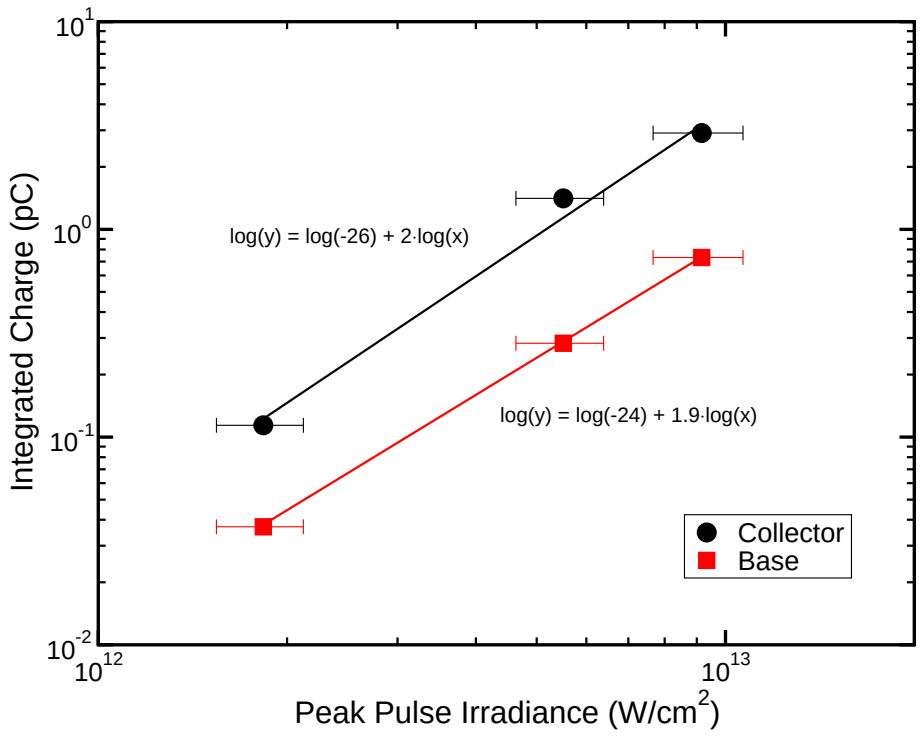

Fig. 32: Verification of the two-photon absorption process in a 0.5×2.5 μm^2 IBM 5AM SiGe HBT. The data are from experimental Case 1, with -4 V on the substrate and all other terminals grounded. In the ideal case, each line would have a slope of two since the number of generated carriers depends on the square of the pulse irradiance. There is a $\pm$6% fractional error in the pulse power and a $\pm$10% fractional error in the focal spot size, which produces an irradiance error of $\pm$16% and a charge collection error of $\pm$6%. The errors in charge collection are smaller than the data point.

The device was characterized by injecting carriers using TPA from a subbandgap pulsed laser [MLM$^+$02]. This technique generates significant densities of electron-hole pairs in proximity of the beam focal point, which can be deterministically positioned in three dimensions. A laptop computer running Python [Pyt] and additional peripheral hardware were used to control the xy-scans of the device at a specific depth and laser pulse energy and then download the location-specific transients from the TDS6124C. The xy-scans for all data sets were 15 μm by 15 μm, yielding 256 unique data points. The data were stored to disk as Python class objects for post-processing with SEEM Reader [PFL07].

Experiments were centered around three bias conditions: Case 1 had a bias of -4 V on the substrate with all other terminals grounded (V_{Sub} = -4 V, V_{EBC} = 0 V), Case 2 had a bias of 3 V on the collector with all other terminals grounded (V_C = 3 V, V_{EBSub} = 0 V), and finally, Case 3 had a bias of -3 V on the substrate with all other terminals grounded (V_{Sub} = -3 V, V_{EBC} = 0 V). Previous broadbeam and single-photon absorption pulsed-laser experiments on pure bipolar applications were conducted with a substrate bias of -4 V [MCC+05, SKM+06]. However, BiCMOS applications call for the substrate to be grounded, which means the device isolation bias must be applied through a positive voltage on the collector. The bias condition of -3 V on the substrate was included to highlight any differences observed when placing 3 V on the collector terminal.

The data shown in Fig. 32 are from experimental Case 1, with a bias of -4 V on the substrate. The plot shows the maximum measured total integrated charge vs. peak pulse irradiance on a log-log scale. This is a quadratic relationship, and since the slopes are approximately equal to two, two-photon absorption is confirmed for the collector and for the base. The base is a more narrow region, so charge collection is less efficient and some charge will be lost, making the trend subquadratic.

The data shown in Figs. 33(a)-(d) show maps of the peak transient magnitude for the emitter, collector, base, and substrate for the bias conditions of Case 1 (V_{Sub} = -4 V). The peak irradiance is approximately 5×10^{12} W/cm^2 including the 31% reflective loss at the air-silicon interface. The emitter and collector transients are negative; the base and substrate transients are positive. A schematic diagram of the deep trench isolation layout is overlaid on the data. The substrate taps for these devices are located 9 μm in the negative y-direction from the bottom of the deep trench isolation. The laser spot

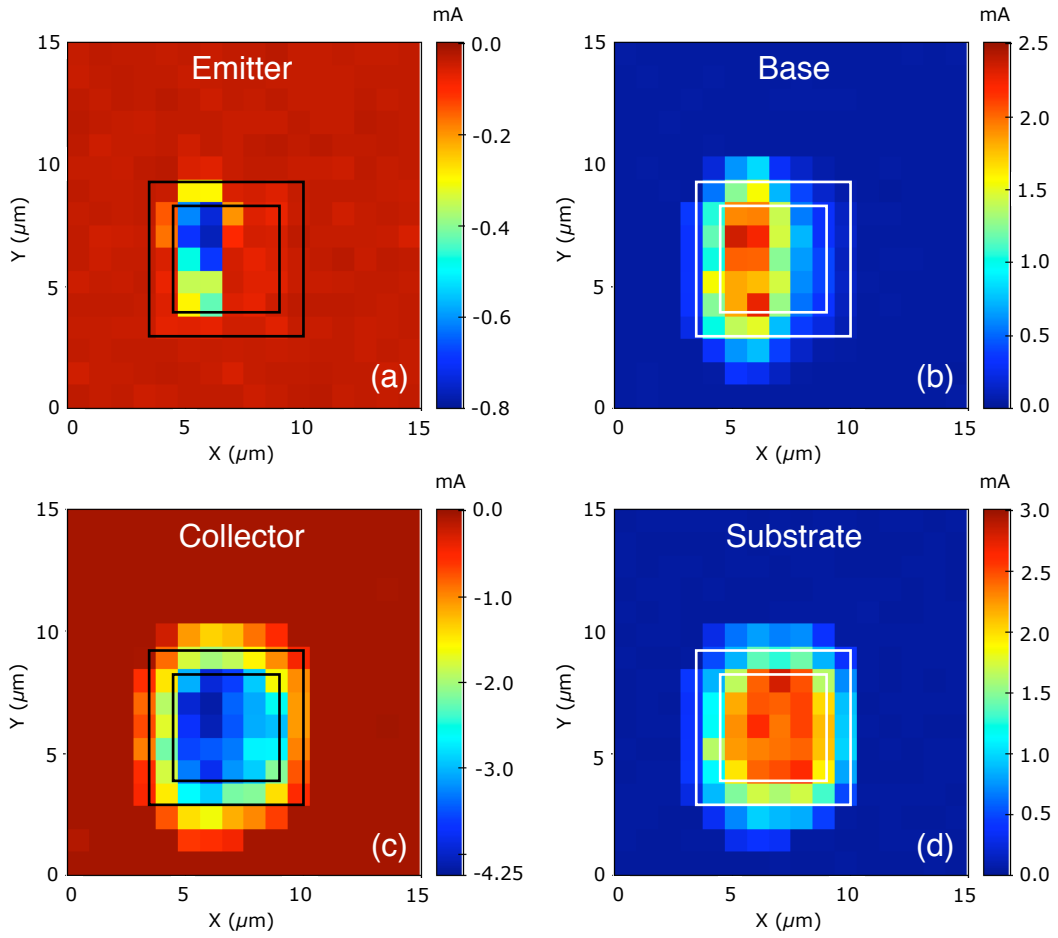

Fig. 33: These maps show the maximum current-transient magnitude for a 5×10^{12} W/cm^2 peak irradiance laser pulse on an IBM 5AM SiGe HBT with bias conditions of Case 1 (V_{Sub} = -4 V). The laser was focused at the device surface in the z-dimension to a diameter of approximately 1.6 μm. The geometry of the deep trench isolation is overlaid on all four images for reference. The substrate taps for this device are 9 μm in the negative y-direction from the outside of the deep trench isolation.

size is approximately 1.6 μm in diameter and focused at the device surface in the z-dimension. The plots shown in Figs. 33(a)-(d) were generated using SEEM Reader [PFL07].

The emitter data in Fig. 33(a) support the two-photon absorption mechanism justified in Fig. 32. The nonzero data points are well confined to the emitter stripe, which could not occur if a significant amount of linear absorption was present. If linear absorption

were present, the spatial distribution would be smeared out after the beam passed through almost 300 μm of silicon from the backside of the wafer to the surface of the device. The peak response of the base and collector terminals is coincident with the emitter-base and base-collector junctions. The peak response is not located at the base and collector contacts.

Recalling the microbeam data shown in Fig. 12 in Chapter II, charge collection inside the active region of the device is approximately constant. Therefore the difference in peak current magnitude in Fig. 33 is made up in the current transient width. Moving outside of the active junctions, to the right inside the deep trench, places the TPA charge packet under the collector sinker. Since the peak current magnitude is lower here, the pulses are wider, greater than 1 ns, to conserve charge.

The data in Figs. 34(a) through 34(d), again produced using SEEM Reader [PFL07], show maps of the peak transient magnitude for the base and collector for the bias conditions of Case 2 (V_C = 3 V) and Case 3 (V_{Sub} = -3 V) with a peak pulse irradiance of 5×10^{12} W/cm^2. The collector transients produced by the bias conditions in Case 2 are larger than the transients in Case 3 for hits to the active device region, defined by the emitter-base and base-collector junctions. While the base transients in Case 2 are slightly larger than those produced by Case 3, by up to 25% for the peak response, the difference is much less than the possible $2x$ increase in peak response for the collector in Case 2 at a peak pulse irradiance of 9×10^{12} W/cm^2. The profile associated with the base-collector junction in Case 2 is also better resolved than in Case 3 where the response is smoother

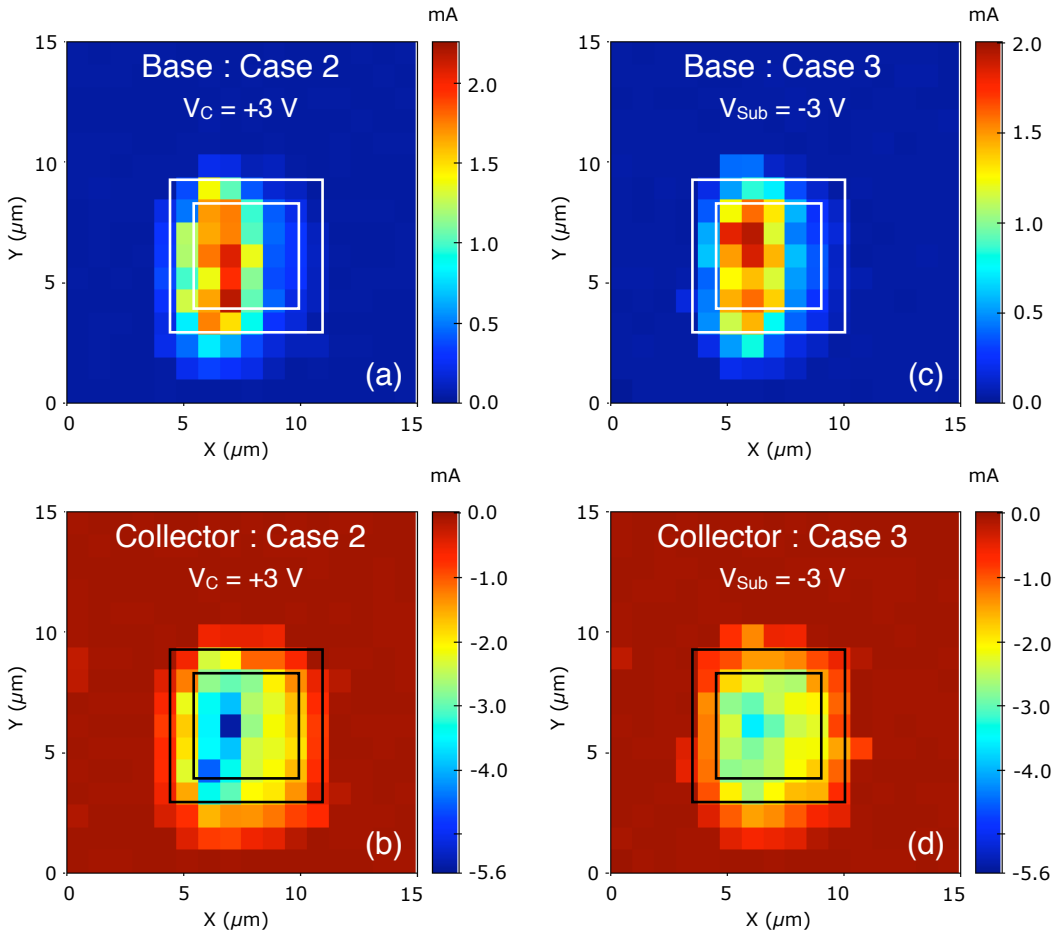

Fig. 34: These maps show the maximum current-transient magnitude for a 5×10^{12} W/cm^2 peak irradiance laser pulse on an IBM 5AM SiGe HBT with bias conditions of Case 2 (V_C = 3 V) and Case 3 (V_{Sub} = -3 V). The laser was focused at the device surface in the z-dimension to a diameter of approximately 1.6 μm. The geometry of the deep trench isolation is overlaid in all four images for reference. The substrate taps for this device are 9 μm in the negative y-direction from the outside of the deep trench isolation. These transients are measured at 50 mV/div for Case 2 and 20 mV/div for Case 3. Note the scales and resolution of the base-collector junction in Figs. 34(b) and 34(d).

across the active region of the device. As in the case for the data shown in Figs. 33(a)-33(d), the laser was focused at the surface of the device to a diameter of approximately 1.6 μm.

The data shown in Figs. 35(a) and 35(b) display current transient waveforms for Case 2 (V_C = 3 V) and Case 3 (V_{Sub} = -3 V) at different pulse irradiance values: 2×10^{12} W/cm^2

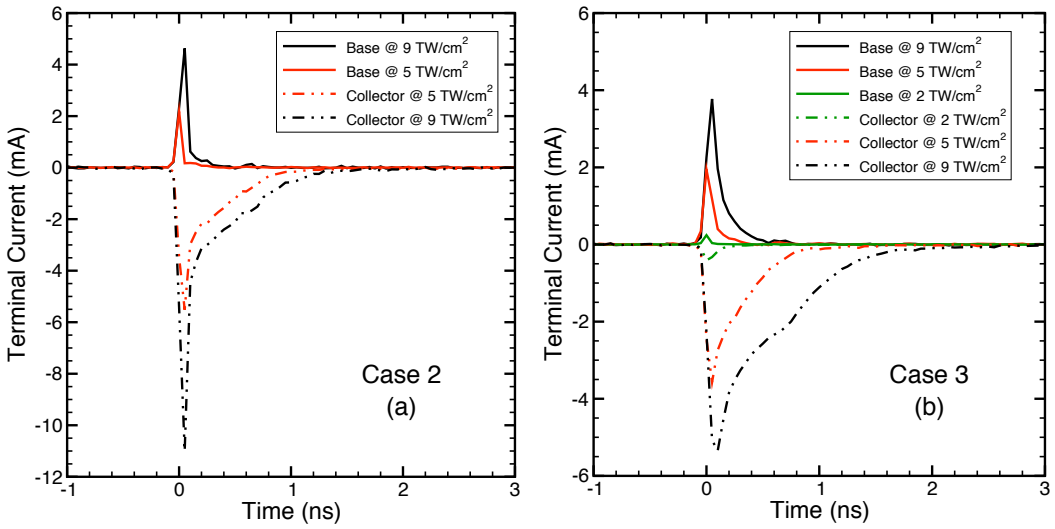

Fig. 35: Base and collector current transients for (a) Case 2 (V_C = 3 V) and (b) Case 3 (V_{Sub} = -3 V). In all cases the beam focal point was at the device surface and focused to a diameter of 1.6 μm. Note the different y-axes on each of the charts. In each case, the base transients are largely unaffected. The Case 2 collector transients are up to 2x larger than their Case 3 counterparts. Note the drastic slope change in the fall time of the Case 2 collector transients. The lengths of the transients are comparable.

(20 kW $\approx$ 3 nJ), 5×10^{12} W/cm^2 (50 kW $\approx$ 8 nJ), and 9×10^{12} W/cm^2 (90 kW $\approx$ 10 nJ). As with the previous data sets, the laser was focused at the surface of the device to a diameter of 1.6 μm. As shown in the spatially correlated maps, there is a small difference between the base transients, but the Case 2 collector transients are up to 2x larger for the 5×10^{12} W/cm^2 and 9×10^{12} W/cm^2 traces for hits to the base-collector junction. In all cases, the pulse lengths are approximately the same.

Finally, the data presented in Fig. 36 show collector transients when the focus of the laser is moved 20 μm below the surface and scanned in the usual 15 μm by 15 μm square. The data are for a 5×10^{12} W/cm^2 peak pulse irradiance and a 1.6 μm diameter focal spot size. The only difference in the data is that the response inside the deep trench isolation has to be measured on a 50 mV/div vertical scale and the other two traces were

measured on a 5 mV/div scale. This difference explains the noise floor discrepancy in the data.

The most important things about these data are the three distinct responses depending on transverse location relative to the deep trench isolation. When far outside the deep trench isolation, a low-magnitude, long-duration diffusion pulse is observed, lasting about 25 ns. When inside the deep trench isolation, the response is similar in magnitude and length to pulses measured at the surface despite moving into the substrate by 20 μm. The pulse measured at approximately 1 μm outside the deep trench isolation shows two response modes, a prompt collapse of the substrate potential (rapid current induction) and a delayed diffusion component, in other words a superposition of the response from inside the deep trench isolation and from far outside the deep trench isolation.

In pure IBM 5AM bipolar applications [MCC$^+$05, SKM$^+$06], the substrate is held at a common negative potential, which is between -3 and -5 V. -4 V has been the popular choice for robust device-to-device isolation, so there is a large body of heavy ion and single-photon pulsed-laser data for this condition. This potential, applied at the substrate taps, reverse biases the n^+/p^- subcollector-substrate junction. However, in BiCMOS applications the substrate must accommodate CMOS transistors in addition to the SiGe HBTs, which means that the substrate has to be held at ground. Therefore, the device isolation bias is applied at the collector terminal. Again, this potential is dropped across the subcollector-substrate junction reverse biasing it.

The difference in the collector isolation bias case, and the reason the collector current transients are up to $2x$ larger, is because of base width modulation related to the Early

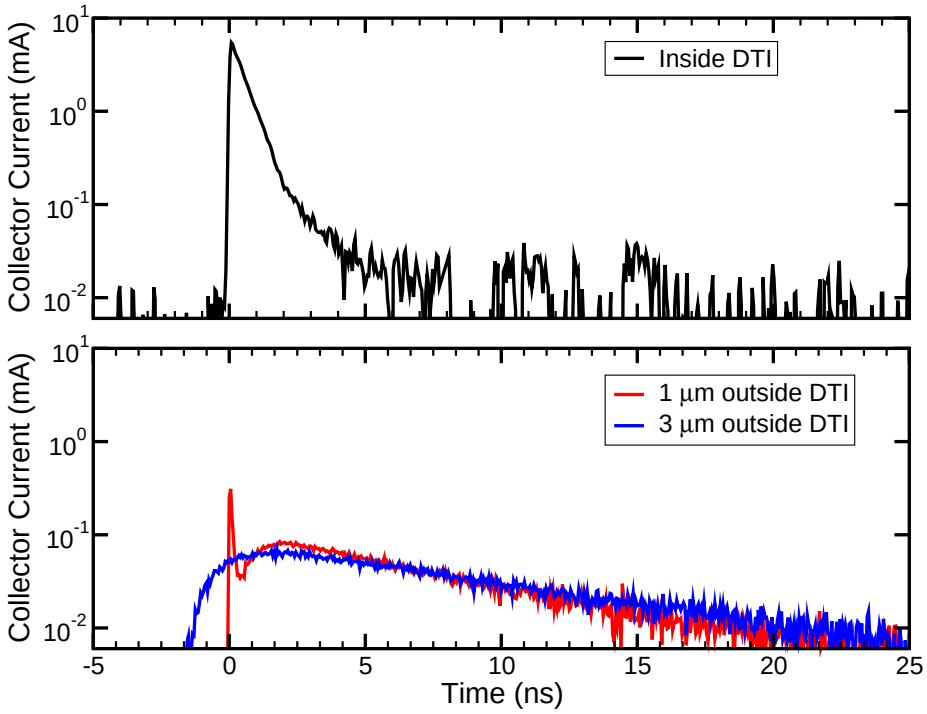

Fig. 36: Collector current transients for a 5×10^{12} W/cm^2 peak irradiance laser pulse 20 μm below the device surface of an IBM 5AM SiGe HBT. The three waveforms were taken from the 15 μm by 15 μm scan at depth. The response inside the trench is similar to the response at the surface. The 1 μm response shows direct evidence of substrate potential modulation that is both location and laser-power dependent. The collector current has been scaled by -1 for plotting on a log scale.

effect [PS91] and the onset of avalanche multiplication [NCZ+99]. In modern SiGe HBTs, the output current is independent of V_{CE} over most of the operating range. However, at high values of V_{CE}, around 3 V for the IBM 5AM process, and high collector current densities, the base-collector depletion region modulates the base width and avalanche multiplication overtakes the output current increase due to the Early effect. The output current data shown in Fig. 37 show that Case 2 (V_C = 3 V) supplies the conditions necessary for collector current enhancement through a combination of the Early effect and avalanche multiplication, which explains the large-magnitude transients originating from pulses focused on the the base-collector junction in Fig. 34(b). The laser testing was

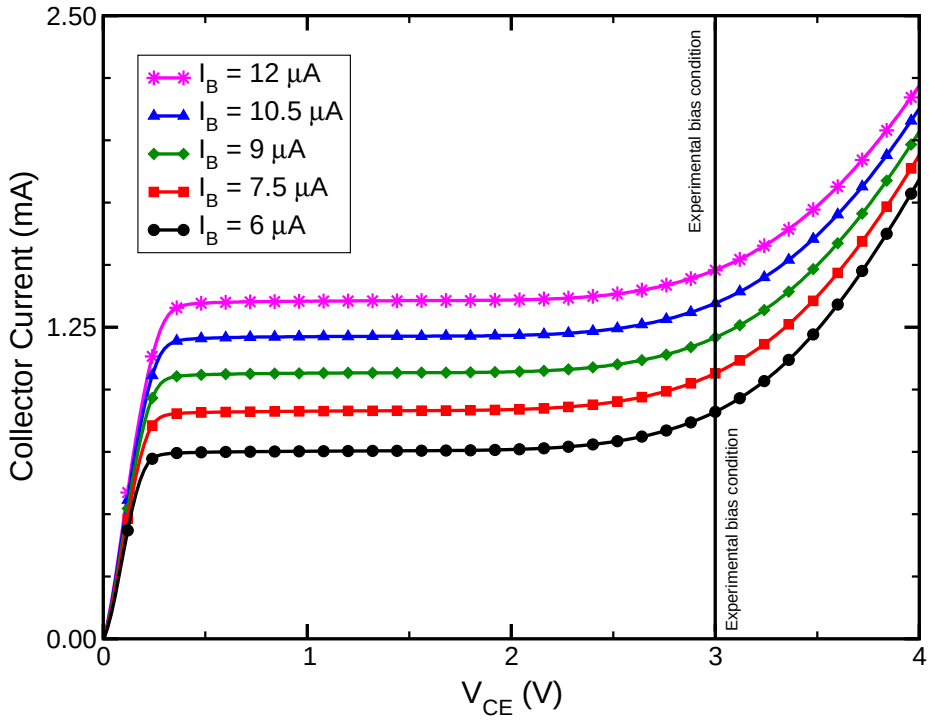

Fig. 37: Forced I_B output characteristics for a 0.5×2.5 μm IBM 5AM SiGe HBT under high injection. The experimental bias condition of Case 2 (V_C = 3 V) is marked. This point occurs at the voltage where the output current becomes a strong function of the collector bias, which helps explain the large transient magnitudes observed in Fig. 34(b). The data markers are sparse, every 5 points, for clarity.

nondestructive; the device under test still retained normal DC operating characteristics following the experiments.

Previous broadbeam heavy ion data sets [MCC+05] from irradiating shift register chains implied that sensitive device cross sections were approximately an order of magnitude larger than the active device area. This pointed to the fact that upsets occurred for events originating outside the deep trench isolation, even for normally incident ions. However, whether or not events outside the deep trench isolation could be responsible for upsets has been debated. These data should help settle that discussion concerning specific circuit applications considering the abundance of events measured in excess of 1 mA for pulses located outside the deep trench isolation.

Thirdly, and perhaps most important for device physics and upset mechanism perspectives, is the issue of diffusion-induced potential modulation. Charge funneling, as conceived in the early 1980s [HMO81b, Hu82, MO82, HMO83], successfully described localized potential deformation, where the transverse area disturbed by the incident particle was much smaller than either the junction crossed or the affected device. However, most bulk SiGe HBTs, like the IBM 5AM process, are manufactured on lightly doped p-type substrates, typically around 1×10^{15} cm^{-3}, which means that when potentials deform into the substrate of these devices, the potential modulation covers a very large area in order to maintain the potential drop fixed by the applied voltage at either the substrate or collector contact. The potential modulation is no longer a localized phenomenon, but a delocalized effect that does not require the ion to cross the active junction and can easily span lateral and vertical distances in excess of 10 μm [PRS$^+$06]. For this reason, potential modulation effects in SiGe HBTs should not be confused with classical funneling processes.

This substrate potential modulation effect can be observed in SiGe HBTs with a pulsed laser when the focal point is below the surface of the device. When the carriers are generated in the field-free region deep in the substrate, outside the deep trench isolation, they diffuse isotropically. If a sufficient density of carriers can reach the subcollector-substrate junction, they will compensate the ionized dopants and force the potential contour surfaces to expand into the substrate, initially limited by the deep trench isolation, until the density of free carriers becomes low enough that the equilibrium position of the potential contours can support the applied bias. The number of carriers that reach the junction is determined by the amount of solid angle the junction

occupies. This also means that the effect is both location and pulse power dependent. The expansion of equipotential surfaces from the subcollector depletion region into the substrate induces currents on the device terminals based on Gunn's theorem [Gun64], the details of which are described in Appendix B. The bimodal collector transient response in Fig. 36 is the first direct evidence of diffusion-initiated potential modulation in SiGe HBTs. Since the carriers are generated a long distance from the critical junction, the potential expands and collapses before all the charge is collected, so there is a secondary diffusion current that is realized after the prompt potential expansion and collapse, which yields the resulting superposition of potential collapse and diffusion responses.

This effect is illustrated qualitatively by the TCAD simulations in Figs. 38(a)-38(b). These are 2-D cuts through 3-D simulations based on the models described in Table 3. A large amount of charge is deposited in the substrate of the device, 1 μm outside the deep trench isolation and 5 μm in the other case. Aside from that difference, the two simulations are identical. The temporal snapshots are taken at the point of maximum potential deformation. The stripe of charge close to the deep trench is able to initiate diffusion-triggered potential collapse, while the stripe of charge farther away cannot. This effect depends on both charge generation location and total energy deposition.

The main issue with pulsed-laser testing, even in the case of two-photon absorption, is the length over which carriers are generated. Though the canonical $1/e$ contour for two-photon absorption is an ellipse with a long axis length of 10 μm [MLM$^+$02], high-energy heavy ions can penetrate hundreds of micrometers into the substrate. This

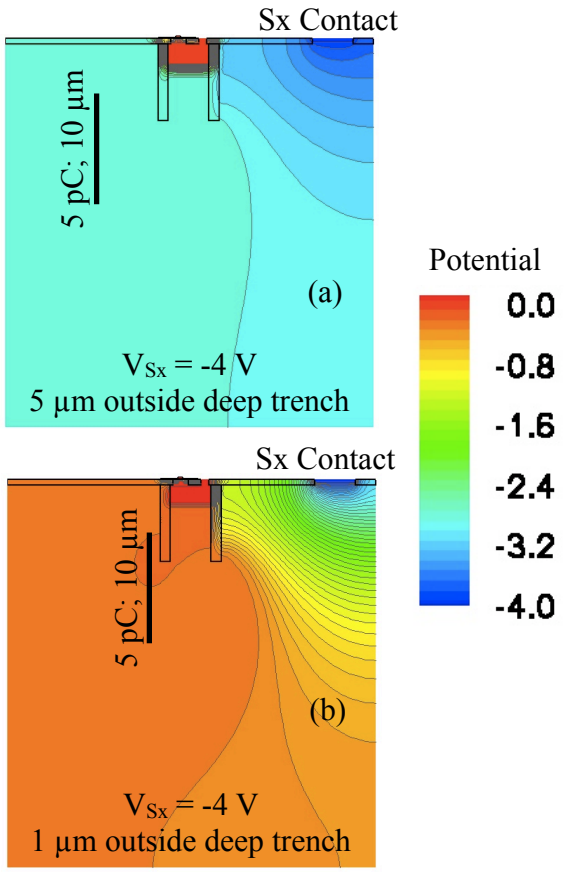

Fig. 38: TCAD simulations showing the effects of charge generation location on diffusion-induced potential modulation in the substrate of a SiGe HBT. The 1 μm result shows potential collapse; the 5 μm result does not. While this is not an exact replication of the carrier generation processes in two-photon absorption, it is qualitatively correct. The two simulations are exactly the same, generating 5 pC of charge over 10 μm, with the exception of the charge generation location. Each temporal snapshot shows the maximum potential deformation in the substrate.

means that the distance and depth over which all of these effects occur for events outside the deep trench isolation increase substantially. Since the initiation of charge collection mechanisms for carrier generation outside of the deep trench isolation depend on solid angle, this explains why heavy ions have such a significant impact on bulk SiGe HBTs. The total solid angle from an ion strike has to be integrated along the whole trajectory out to a diffusion length. This would lead to an increase in the area over which critical SEEs can occur, which is consistent with the IBM 5AM SiGe HBT broadbeam heavy ion results [MCC$^+$05]. The mechanisms and general characteristics of heavy ion

transients are not expected to differ from those observed with two-photon pulse-laser testing.

The results presented here confirm the presence of nonlocal potential modulation in IBM 5AM SiGe HBTs. While this effect has demonstrable consequences for bulk SiGe HBTs in general, it is also expected to apply to many critical situations in CMOS, such as well potential collapse and recovery. This work has also established that the isolation bias terminal could be a critical aspect when considering the peak magnitude of collector current transients and that certain applications may suffer larger collector current transients for events that strike the active device regions directly.

Current-transient measurements on bulk SiGe HBTs should include both heavy ion microbeam and broadbeam experiments in order to quantify the differences between a small packet of laser-generated carriers and the much longer and more consequential heavy ion trajectories. Further two-photon absorption work should also be done in order to investigate the more generally applicable consequences of deep three-dimensional response mapping in lightly doped substrates. The next section covers the former.

Heavy Ion Microbeam Current Transients

The final two sections cover SiGe HBT current transients induced by a focused heavy ion microbeam and by heavy ion broadbeam irradiation. This is the first time these data have ever been measured. The microbeam results are based on techniques described in Appendix B and first introduced in Chapter II. However, in this case, instead of just recording the total collected charge for a particular xy-position, the entire ion beam

induced current waveform is recorded. This is called time-resolved ion beam induced charge (TRIBIC) microscopy [SWS+98, SWS+99, LHOI05, FCPG+06, BVVS07].

The experimental setup is exactly the same as the one used to measure the pulsed laser-induced current transients in the previous section with the exception of the fact that the oscilloscope is different. These microbeam experiments used a Tektronix DPO72004 real-time digital phosphor oscilloscope with 16 GHz of hardware analog bandwidth and 50 GS/s on all four input channels. The previous oscilloscope used for the pulsed laser-induced transients, a Tektronix TDS6124C, had 12 GHz of hardware analog bandwidth and 40 GS/s on two input channels or 20 GS/s on four input channels. The microbeam experiments also used the same high-speed packages and IBM 5AM SiGe devices, with 0.5×2.5 μm^2 emitter areas, which have been previously described. The bias conditions for the microbeam experiments mirrored the two-photon absorption pulsed laser experiments with one addition. The devices were biased into four different configurations: Case 1 had $V_{\text{Sub}} = -4\,\text{V}$ and all other terminals grounded; Case 2 had $V_{\text{C}} = 3\,\text{V}$ and all other terminals grounded; Case 3 had $V_{\text{Sub}} = -3\,\text{V}$ and all other terminals grounded; and Case 4 had all four device terminals grounded.

Though the microbeam current transient measurement experiments are an exact analog of the two-photon absorption pulsed laser experiments just differing in the radiation source, that difference has a large impact on the way the results are interpreted. Pulsed laser testing, while more convenient and economical, produces results based on unknown inputs. Before the beam enters the device under test, it is well-defined and controlled, but after entering the device higher-order nonlinear effects can change the final irradiance at the beam waist, altering the assumed *a priori* generated

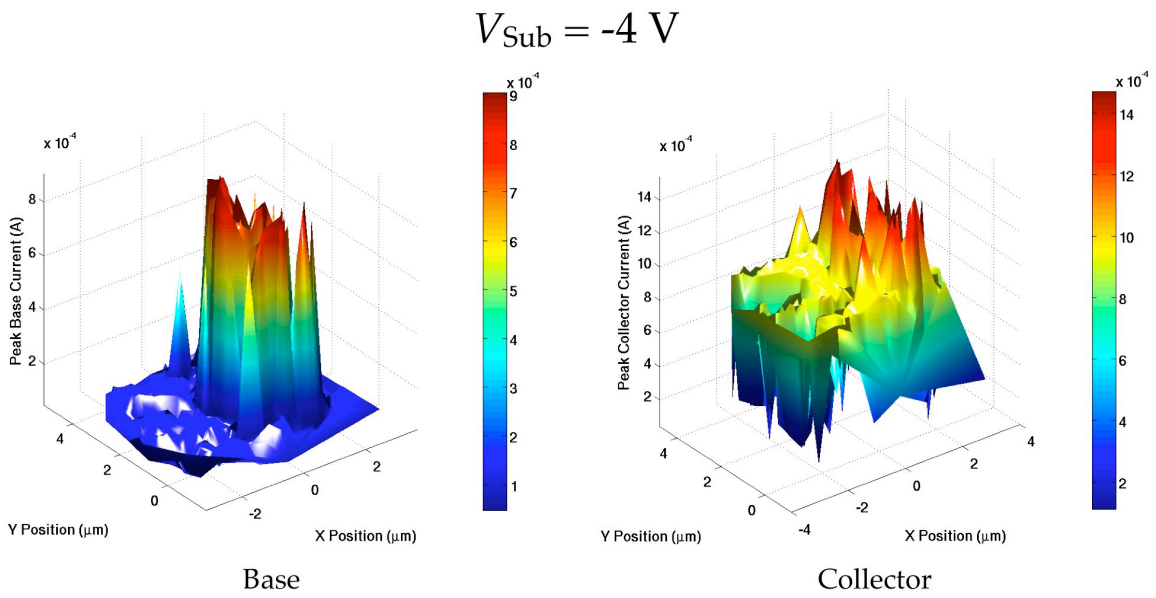

Fig. 39: 36 MeV ^{16}O TRIBIC scan on a 0.5×2.5 μm^2 IBM 5AM SiGe HBT with $V_{\text{Sub}} = -4$ V for the base and collector terminals. The peak current for each terminal is plotted. The current scaled is given in 10^{-4} A. The transients themselves were scaled by -1 to yield a positive scale.

carrier density. Comparison to broadbeam data is an effective way to remove systematic error, but that only works for circuit applications [Pea06]. However, microbeam current transient measurements present the ideal solution since the energy loss and interaction of heavy ions with materials are well-known [ZBL85, Zei04, ZB08].

Fig. 39 shows the results of a 36 MeV ^{16}O TRIBIC scan on a 0.5×2.5 μm^2 IBM 5AM SiGe HBT for the base and collector terminal under a substrate bias of -4 V. The $\mathrm{d}E/\mathrm{d}x$ curves for 36 MeV ^{16}O in silicon are shown in Fig. 48 in Appendix B. The scan area is 20 μm by 20 μm with 200 nm steps. The scan produced 384 data points based on a -4 mV trigger on the collector. As was observed with the laser testing results in Fig. 33, the base and peak collector responses are confined to the base-collector junction, which is located on the y-axis between 0 and 4 μm and between 0 and 2 μm on the x-axis. The collector response plateau at 0.9 mA is the response from the oxygen ion crossing the

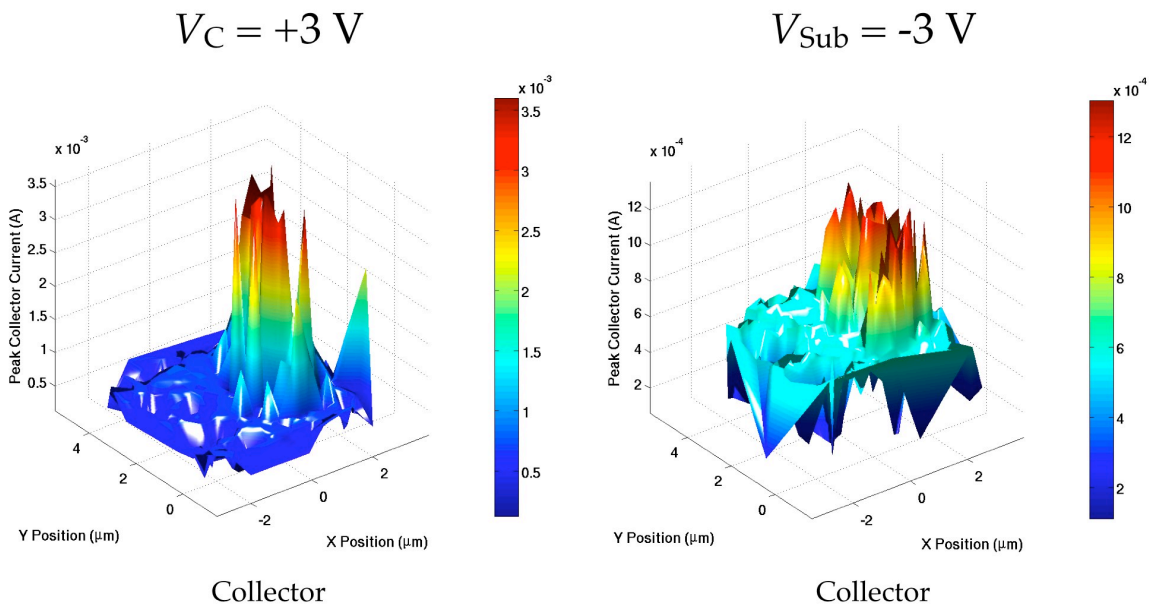

Fig. 40: 36 MeV ^{16}O TRIBIC scan on a 0.5×2.5 μm^2 IBM 5AM SiGe HBT with $V_C = +3$ V and $V_{Sub} = -3$ V for the collector terminal. The peak current for the collector terminal is plotted. Note the difference in the current magnitudes. The peak current magnitude outside of the base-collector junction is approximately the same at 0.5 mA. The transients themselves were scaled by -1 to yield a positive scale.

subcollector junction. The apparent gaps in the 3-D plots are due to the fact that the data points are not regularly spaced because each step of the electromagnetic lenses does not necessarily deposit an ion into the device. The delaunization creates valleys where the data points are missing.

Fig. 40 shows 36 MeV ^{16}O TRIBIC scans for the collector terminal under two different bias conditions: $V_C = +3$ V and $V_{Sub} = -3$ V. These data were gathered with the same scan parameters given in regard to Fig. 39. Again, these data parallel the pulsed laser results in Fig. 34. With the large positive bias on the collector, instead of a negative bias on the substrate, the collector current transients within the base-collector junction are magnified by more than a factor of two. The rest of the area within the deep trench isolation shows transients of approximately the same peak

magnitude at 0.5 mA, which occurs because the same potential is dropped across the subcollector/substrate junction. The magnification of the base-collector junction transients is due to a combination of the Early effect [Ear52] and avalanche multiplication [NCZ+99]. It is interesting to note that the collector response for $V_C = +3\,V$, qualitatively, looks very similar to the base response shown in Fig. 39.

The largest peak magnitude transients for the three bias conditions given so far for the base and collector are shown in Figs. 41(a) and 41(b). As shown in Fig. 40, biasing the collector at a large positive voltage, close to, but not exceeding BV_{CE0}, produces collector transients that are larger by more than a factor of two compared to the same (opposite polarity) bias on the substrate. This also introduces a lot of noise into both the base and collector waveforms. The base current waveforms are nearly independent of these three biasing schemes, which is consistent with the device physics of bipolar transistors.

It is clear from an inspection of the pulsed laser waveforms in Fig. 35 that the microbeam deposits less energy into the system than the majority of the pulsed laser data. The microbeam data shown in Fig. 41 suggests that an equivalent two-photon absorption pulse irradiance would be approximately 3 TW/cm^2, which is much lower than the 5 and 9 TW/cm^2 irradiances due to the fact that the generated carrier density in two-photon absorption goes as the square of the pulse irradiance. Nevertheless, both data sets provide valuable baselines for future device simulations and interpretation of measured broadbeam current transients.

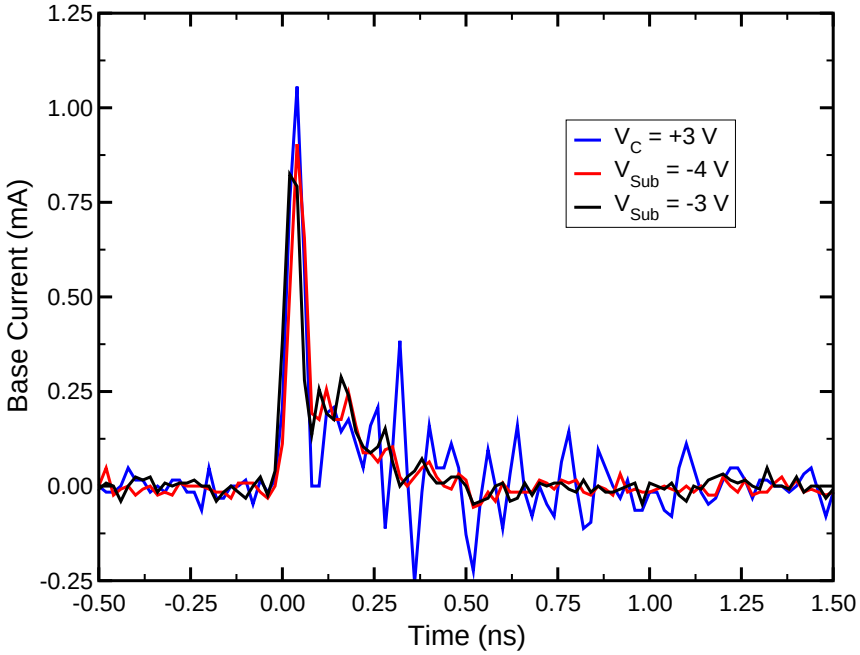

(a) TRIBIC waveforms for the base terminal

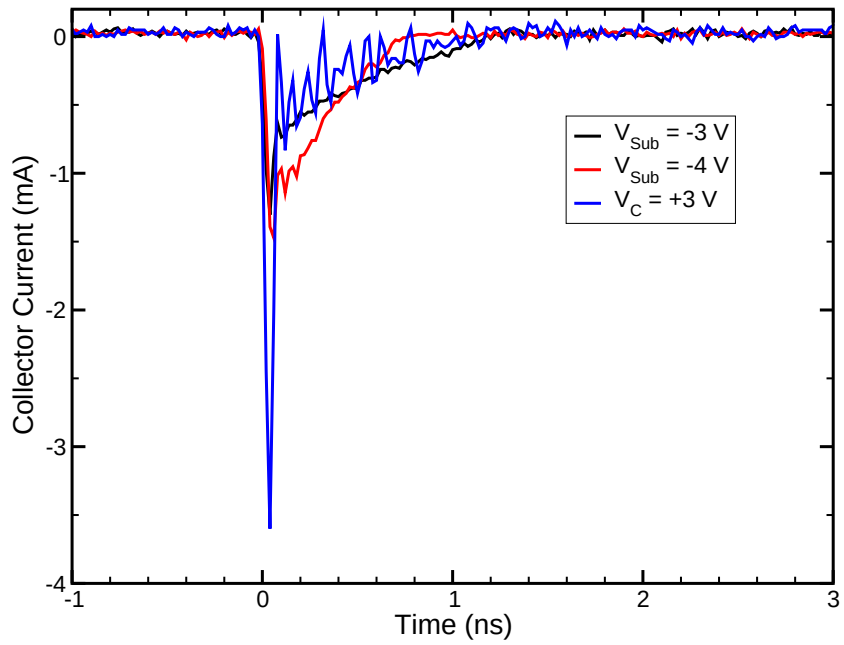

(b) TRIBIC waveforms for the collector terminal

Fig. 41: Peak magnitude TRIBIC waveforms for the base and collector terminals of a $0.5 \times 2.5\ \mu m^2$ IBM 5AM SiGe HBT as a function of bias. When the collector is biased to a large positive voltage it introduces much more noise into the base and collector waveforms. These are the peak magnitude waveforms from Figs. 39 and 40.

Table 4: JYFL Broadbeam Transient Experimental Summary

Ion	**LET $(\mathbf{MeV \cdot cm^2})/\mathbf{mg}$, Energy (MeV)**	**Angle**	**DUT Bias**
^{20}Ne	3.6, 186	0°	$V_{Sub} = -4\,V$, $V_C = +3\,V$
^{40}Ar	10.1, 372	0°, 60°	$V_{Sub} = -4\,V$, $V_C = +3\,V$
^{84}Kr	32.1, 768	0°	$V_{Sub} = -4\,V$, $V_C = +3\,V$
^{129}Xe	60, 1200	0°	$V_{Sub} = -4\,V$, $V_C = +3\,V$

Heavy Ion Broadbeam Current Transients

Broadbeam current transients were measured at the Jyväskylän Yliopisto cyclotron at the University of Jyväskylä, Finland (JYFL) with collaborators D. McMorrow of the Naval Research Laboratory and J. Baggio and O. Duhamel of the Commissariat à l'énergie atomique, France. These transient data were gathered on the same 0.5×2.5 μm^2 IBM 5AM SiGe HBT used in the pulsed laser and heavy ion microbeam experiments. This the first time these data have been measured for a SiGe HBT. Table 4 gives a summary of the completed experiments.

The exposures on the device under test were run to fluences between 3.9×10^7 cm^{-2} and 2.9×10^8 cm^{-2} over the course of ten experiments. Each exposure resulted in somewhere between 10 and 51 events captured on the base and collector channels. A Tektronix TDS6124C digital storage oscilloscope was used for capturing the transient waveforms. This is the same oscilloscope used for recording transients during the two-photon absorption pulsed laser experiments. The SiGe HBT device was packaged in the same high-speed fixture used for both the pulsed laser testing and microbeam testing. Neon events were captured with the base and collector oscilloscope channels set

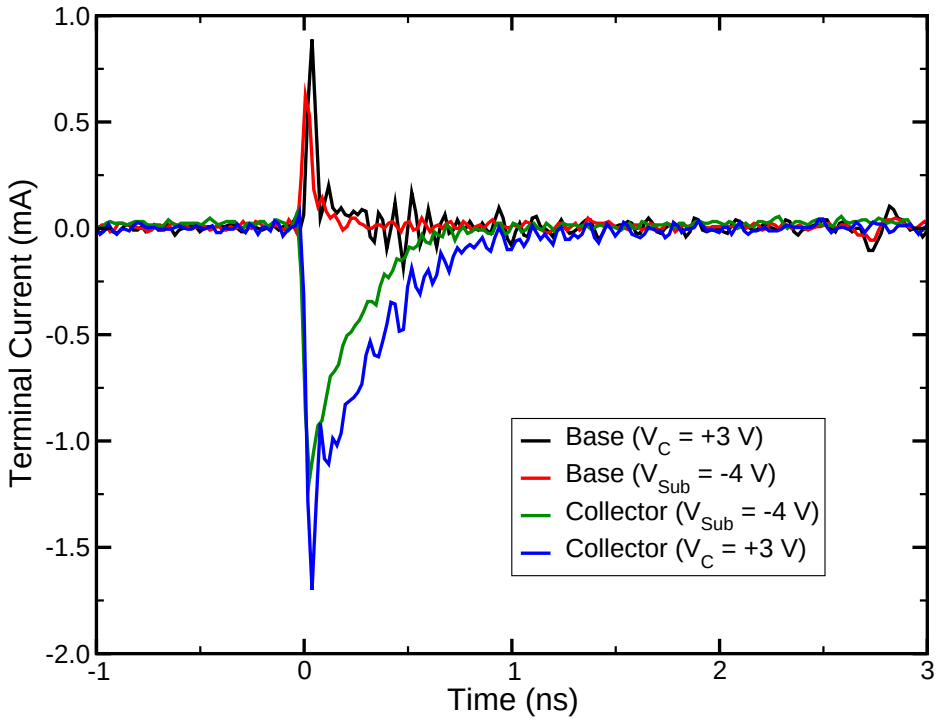

Fig. 42: Peak magnitude base and collector broadbeam current transients for normally-incident 186 MeV ^{20}Ne on a 0.5 $\times$ 2.5 μm^2 IBM 5AM SiGe HBT as a function of device bias.

to 10 mV/div. For all other exposures, the collector channel was set to 20 mV/div. The oscilloscope was set to trigger on the collector channel at a level of -15 mV, or 0.3 mA.

Fig. 42 shows normally-incident neon current transients for the base and collector terminals as a function of bias. As expected, reverse biasing the collector to a positive voltage results in larger collector transients than a nearly equal reverse bias on the substrate. The base current transients are not appreciably affected by the change in bias conditions. Based on the microbeam data presented in the previous section, these transients are probably from a direct strike to the active region of the device. Since broadbeam irradiation provides no spatial correlation with the induced current waveforms, this conclusion is derived from engineering judgment. The average cross section for these neon measurements is 1.2 $\times$ 10^{-7} cm^2, or about 12 μm^2, which

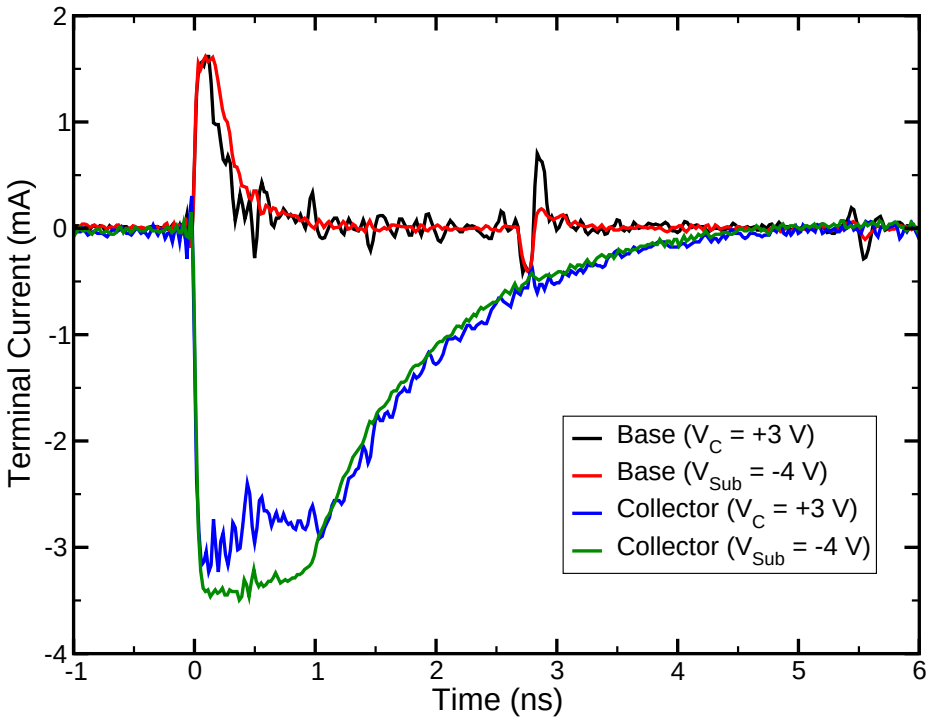

Fig. 43: Peak magnitude base and collector broadbeam current transients for normally-incident 1.2 GeV ^{129}Xe on a 0.5×2.5 μm^2 IBM 5AM SiGe HBT as a function of device bias. The bipolar glitch on the two base transients are believed to be systematic artifacts and not part of the actual device response.

is approximately the area of the active region enclosed by the deep trench isolation. Of course, this cross section depends on the trigger level of the oscilloscope. However, since 186 MeV ^{20}Ne has a low LET, broadbeam data [MCC$^+$00, MCC$^+$05], the event rate model presented in Chapter III, and microbeam data suggest that these transients would only be recorded for hits within the active region of the device.

The 1.2 GeV ^{129}Xe current transients shown in Fig. 43 show very different characteristics than the low LET neon data in Fig. 42. Contrary to previous cases, bias does not seem to have a significant impact on the magnitude of the collector current transients. The collector current transients are much longer, over 3 ns as opposed to the sub-1 ns transients observed for low-LET neon exposures. The plateau at the bottom

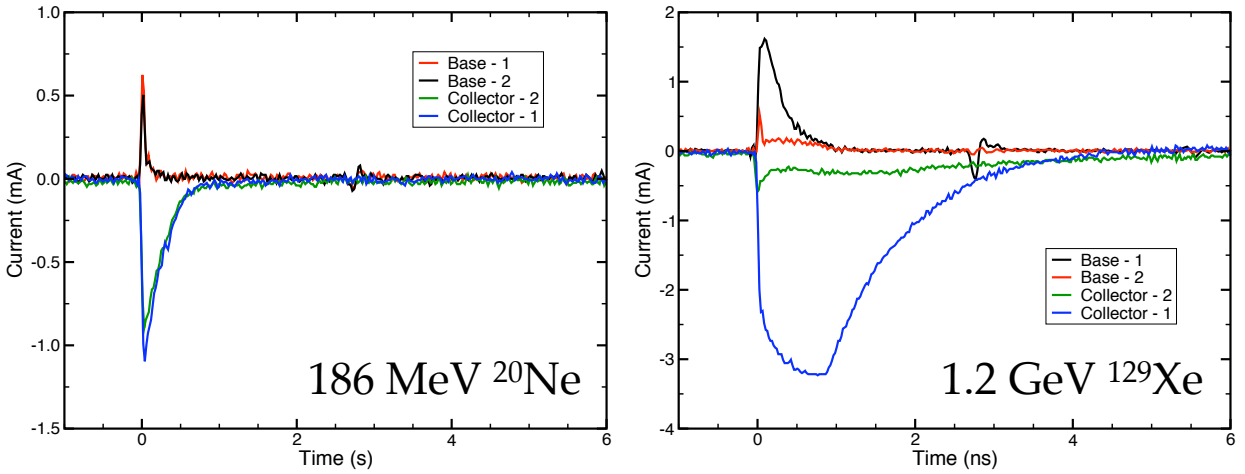

Fig. 44: Selection of base and collector transient waveforms for normally-incident neon and xenon exposures on a 0.5×2.5 μm^2 IBM 5AM SiGe HBT under a substrate bias of -4 V. The waveforms shown are not correlated to the same collector trigger; they are meant to give an idea of the range of possible events for a given particle and LET.

of the collector current transient implies prolonged potential drop and saturation. The average cross section for the xenon exposures, based on the collector channel trigger level of -15 mV, is 32 μm^2, which is larger than the active area of the device under test.

The figures shown so far have only included the maximum peak magnitude transients. However, transients with different morphologies were recorded. Fig. 44 shows a sample of measured waveforms from the normally-incident neon and xenon exposures. Though the waveforms are not correlated to the same collector trigger, they reveal important information about the effects of two extreme LETs. All of the recorded neon transients were approximately the same since all of the events most likely originated from within the active region of the device. However, xenon events covered a wider range due to the fact that events occurring outside the deep trench isolation, which are probably the origin of the Base-2 and Collector-2 waveforms in the xenon data in Fig. 44.

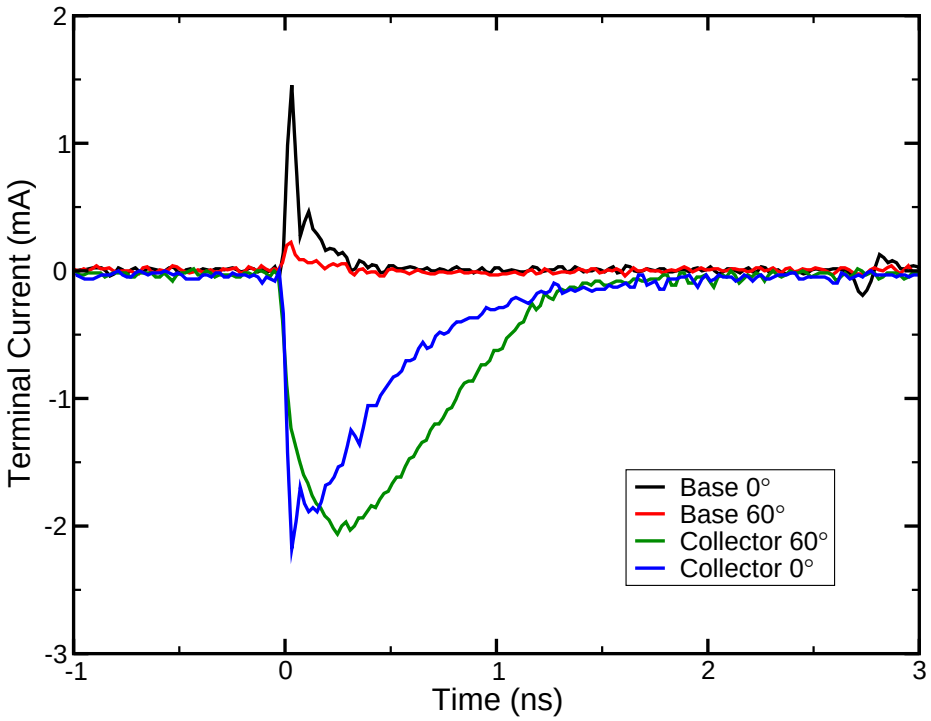

Fig. 45: Peak magnitude base and collector broadbeam current transients for normally-incident 372 MeV ^{40}Ar on a 0.5 × 2.5 μm^2 IBM 5AM SiGe HBT as a function of angle of incidence.

Finally, the argon data in Fig. 45 show the effect of angle of incidence on current transient waveforms for the IBM 5AM SiGe HBT. The device orientation relative to the beam was not recorded, so it is impossible to tell if the ions' velocity was parallel or perpendicular to the emitter length. The dynamics of the collector response are different, though the pulse widths are approximately the same. The base transients show a large change depending on angle of incidence, but this could be due to the fact that the 60° strike passed through the heavily doped extrinsic base and not through the more responsive base-collector junction. The most encouraging result from the angled argon irradiation is the change in cross section. The normally-incident exposure resulted in a cross section of 130 μm^2, whereas the angled irradiation had a cross section of 8 μm^2 – dropping by a factor of sixteen. This is direct evidence of the cross section roll-off

at low LET observed by Marshall, Reed, and other in 2000, 2003, and again in 2005 [MCC+00, RMP+03, MCC+05]. The event cross section decreases due to ion interactions with the deep trench isolation, covered in Chapter III [PRS+07].

The heavy ion broadbeam current transients, in conjunction with the pulsed laser and heavy ion microbeam results, support and explain many aspects of the earlier SiGe HBT shift register testing [MCC+00, MCC+05, SKM+06]. Taken by themselves, these transient data reveal details about the underlying charge collection and single-event mechanisms in SiGe HBTs. Each of the three transient data sets builds on the others. Pulsed laser testing showed the effects of transverse and vertical charge generation location on transients, revealing non-local substrate potential modulation and the sensitivity to bias conditions. Microbeam testing supported the conclusions of the pulsed laser testing while providing a simpler and better-understood radiation source, a key benefit for future modeling efforts. The broadbeam heavy ion current transient measurements provide the best approximation to the space environment. The ions have high LETs and long ranges, which is something microbeam irradiation lacks. Depth of penetration is an important detail to cover for SiGe HBTs due to the lightly-doped substrate and large sensitive volumes. However, the broadbeam measurements rely on the pulsed laser and microbeam measurements to infer event location since the broadbeam data lack spatial correlation. Taken together, these data sets form a complete experimental picture of charge collection processes and single-event mechanisms in SiGe HBTs.

CHAPTER V

CONCLUSION

This dissertation work, in conjunction with earlier charge collection studies [Pel06], presents a comprehensive description of single-event mechanisms for bulk SiGe HBTs. This work developed the first event rate calculation model for SiGe HBTs that incorporated single-event-critical process features. It also presented the first experimentally-measured IBM 5AM SiGe HBT pulsed laser current transients and the first SiGe HBT current transients for heavy ion microbeam and heavy ion broadbeam radiation sources.

The measured transients presented here proved the efficacy of experiments in a region normally dominated by mixed-mode technology computer-aided design simulations. To this point, the only way to derive applicable single event SiGe HBT current transients was to simulate them. However, since mixed-mode simulation of SiGe HBT netlists is hindered by the lack of advanced compact models compatible with commercial device simulators, the results of those simulations lack realistic feedback. These experimental data will provide that necessary feedback.

The pulsed laser, heavy ion microbeam, and heavy ion broadbeam transient data contain direct evidence of non-local substrate potential modulation. This potential push-out from the subcollector junction into the substrate is simultaneously responsible for increased transient magnitude and increased sensitivity to events occurring outside of the deep trench isolation, away from the active region of the device. This is manifested in SiGe HBT circuit applications as a low single-event threshold and a large saturated single-event cross section. The broadbeam argon ion transients demonstrate, with a

single device, the effect of cross section roll-off resulting from ion-deep trench isolation interactions, an effect inferred for the event rate model, now proven.

Future single-event effects work on SiGe HBTs, as well as CMOS and SOI technologies for that matter, should continue to explore and embrace experimental current transient measurements. Accurate measurement of such a fundamental result can be used to build realistic device simulations and thereby contribute to higher quality single-event effects studies at the circuit and system levels.

APPENDIX A

EFFECTIVE LINEAR ENERGY TRANSFER AND FLUENCE

Linear energy transfer (LET), also known as mass stopping power, is the stopping power normalized by the material density. LET $= (d\mathrm{E}/d\mathrm{x})/\rho = (\mathrm{MeV}\cdot\mathrm{cm}^2)/\mathrm{mg}$ in conventional units. Sometimes it is given as $(\mathrm{MeV}\cdot\mathrm{cm}^2)/\mathrm{g}$, making the quantity larger by 10^3. The stopping power of a given ion depends on the energy and mass of the particle in addition to the atomic density of the target material. The matter is further complicated in the radiation effects community because of geometrical corrections related to single-event upset (SEU) rate calculations.

The integrated rectangular parallelepiped (IRPP) model [PPAS92, Pet08] is based on the path length of heavy ions traversing a RPP sensitive volume. A particular single-event effect (SEE) depends on device thickness and the total amount of charge generated in that device thickness. This in turn depends on the ion's total path length through the device sensitive volume. In early radiation effects testing, the idea of linear charge deposition was introduced by Koga in 1984 [KK84].

Since the charge generated in a thin lamina depends on the ion's angle of incidence, it is possible to measure a range of charge generation by varying the angle of the beam relative to the face of the device under test (DUT). The results need to be normalized to the effects of the beam at normal incidence, which is where the geometrical corrections enter. Linear charge deposition is defined as

$$L_0 \sec(\theta)\,, \tag{22}$$

where L_0 is the LET of the incident ion and θ is the angle relative to the surface normal of the DUT. As the angle of incidence is increased, the effective LET also increases due to the longer path length through the lamina. This idea has developed into the concept of effective LET.

There is an associated concept, called effective fluence. While the ideal heavy ion experiment would allow for the continual change of LET at normal incidence, this is not usually feasible due to time and cost constraints. So, the DUT is rotated in front of the beam to increase the effective LET for a given ion at a specific energy. However, rotating the DUT causes an apparent decrease in the fluence observed at normal incidence – or conversely an increase in the measured single-event cross section. This is shown schematically in Fig. 46. To normalize the results to the measurements at normal incidence, the fluence is scaled by $\cos(\theta)$. Instead of that, the number of upsets is sometimes scaled by $\sec(\theta)$. In either case, the result is the same.

While these changes seem purely mathematical, they imply specific methodologies related to the IRPP model for single-event rate calculations. In cases where nuclear reactions, small volumes, thick volumes, or small-geometry effects in deep sub-micrometer CMOS dominate event rates these concepts may be invalid. When interpreting measured single-event cross sections, it is often best to remove any IRPP corrections or plot the data as a function of incident ion angle [RWS$^+$06, RWM$^+$07, PRS$^+$07] to avoid confusion and misinterpretation.

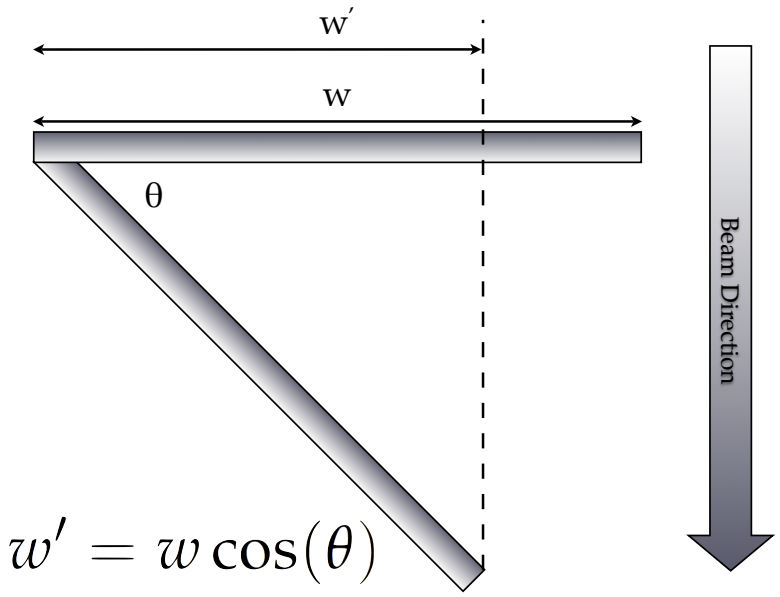

Fig. 46: Diagram showing the concept of effective fluence. This is the same principle applied to effective LET, but in that case $\cos(\theta)$ is in the denominator. The DUT area at normal incidence appears to decrease with increasing angle. The normalization of this effect relative to the situation at normal incidence results in the introduction of the geometrical correction.

APPENDIX B

ION BEAM INDUCED CHARGE MICROSCOPY

There are two classes of ground-based ion testing for radiation effects: broadbeam and focused heavy ion microbeam. Reed, *et al.* [RKP+03] reviewed the present condition of ground-based testing in 2003, which included both broadbeam and microbeam techniques. Microbeam irradiation involves accelerating a low flux of heavy ions and focusing them with electromagnetic lenses to a small rectangle, of order 1 μm in both x- and y-dimensions. This rectangular event window is swept across the surface of the target in question, which is a single SiGe HBT in this case. A diagram of the basic ion beam induced charge (IBIC) process is shown in Fig. 47.

IBIC microscopy uses a beam current of 0.1-10 fA, which is between 1 and 10^4 ions/s. These ions are typically light and have energies from several megaelectron volts to tens of megaelectron volts. The technique measures the individual current pulses from each of these ions and tags them with a specific xy-position. This is not broadbeam irradiation, so ions are not distributed uniformly throughout the rectangular event window. Instead, ions, one at a time, pass through somewhere within the event window, leading to positional uncertainty for each recorded xy-location. The necessary condition for this setup is that each ion must produce enough electron-hole pairs to generate a current pulse that exceeds the device noise level. For silicon, it takes 3.6 eV to generate a single electron-hole pair [Kle68, AB78]; this translates to 22.5 MeV/pC, or, in terms of linear energy transfer, 97 $(\text{MeV}\cdot\text{cm}^2)/\text{mg} = 1$ pC/μm. Since SiGe HBTs respond to deeply penetrating ions due to the lightly doped substrate, IBIC microscopy

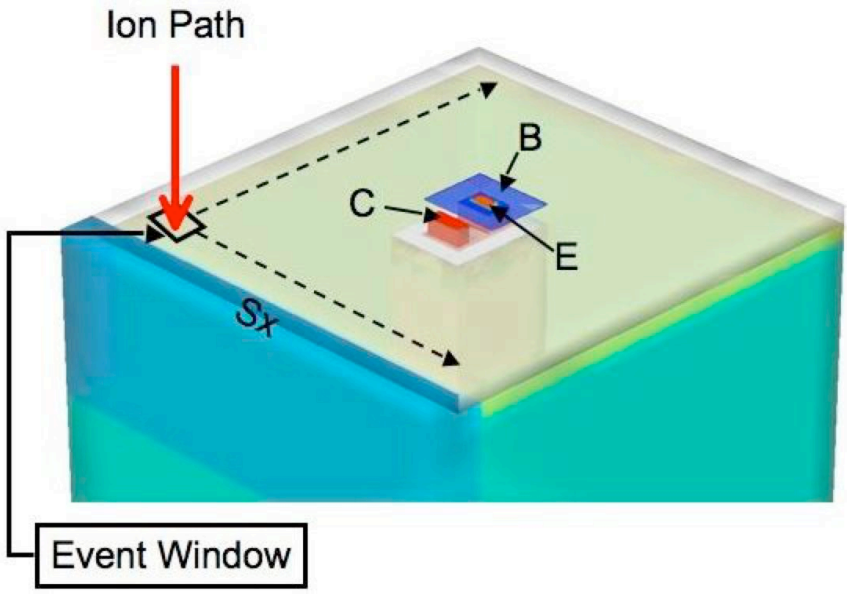

Fig. 47: Graphical depiction of ion beam induced charge microscopy on the IBM 5HP SiGe HBT process. The event window, which scans over the device surface in small steps, deposits single heavy ions at known xy-coordinates. The relevant device terminals are labeled.

becomes a trade between ion range and linear energy transfer. The ion of choice for this work has been 36 MeV ^{16}O. It has a range just over 25 μm in silicon and a peak LET of approximately 7 $(\text{MeV} \cdot \text{cm}^2)/\text{mg}$. The detail for the two curves is shown in Fig. 48.

There are many models that describe the induction of charge on sensing electrodes due to the drift of charge carriers generated by ionization. Some of the earliest work was completed by Von Karl Hecht in the early 1930s [Hec32], which was done to optimize radiation detectors. This work was followed by the efforts of Shockley [Sho38] and Ramo [Ram39]. As implied by its name, the IBIC signal is not due to the collection of electrons or holes on the sensing electrode, but is the charge resulting from the integration of the instantaneous current transferred to a charge controlled amplifying device and generated by the motion of the free carriers subject to an electric field [BVVS07]. This conclusion is based on the following assumptions:

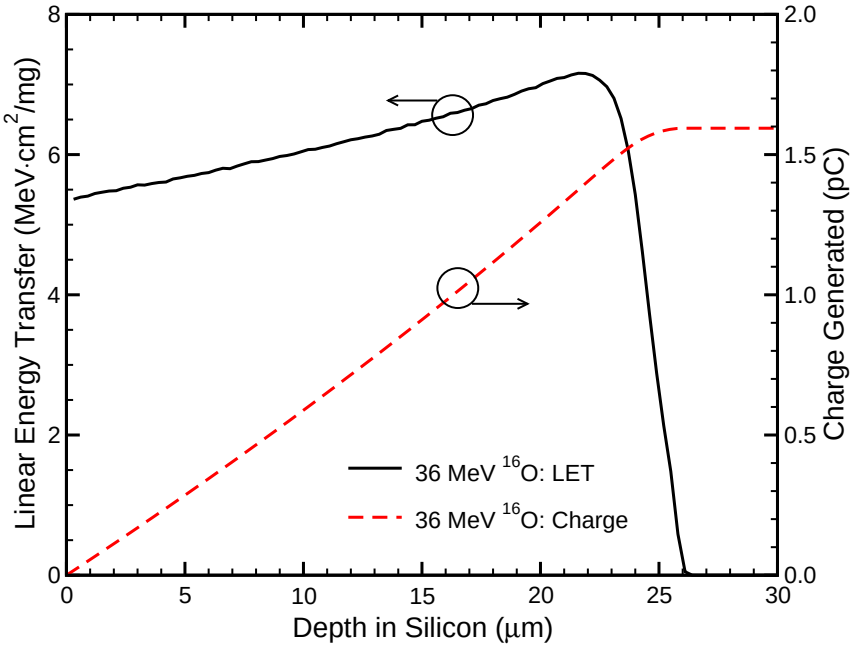

Fig. 48: Energy loss and charge generation curves for 36 MeV ^{16}O in silicon. The results are provided by MRED [RWM+07] and SRIM [ZB08].

1. A negligible perturbation of the field within the semiconductor due to the excess charge produced by ionization;
2. An instantaneous propagation of the electromagnetic field;
3. Electrodes connected to ideal voltage sources of DC potentials, so that the motion of charge carriers does not affect the electrode potentials.

This induction mechanism is connected to the evaluation of the transport mechanism in semiconductors. In the 1-D case of two parallel plate electrodes separated by d with a moving point charge q between two points Δx apart, the Shockley-Ramo theorem [Sho38, Ram39, BVVS07] states that the induced charge ΔQ is given by

$$\Delta Q = q \cdot \frac{\Delta x}{d} . \tag{23}$$

Therefore, measurement of ΔQ constitutes a measurement of the mean free path of the

charge carriers. From Eq. 23, the induced current $I(t)$ can be calculated:

$$I(t) = q \cdot \frac{v[x(t)]}{d}, \tag{24}$$

where v is the carrier velocity.

In 1964, Gunn proposed a general expression for electrostatic induction for any arrangement of conductors and charges [Gun64]. In this formulation, the induced current due to the motion of a charge q along a line segment $\mathrm{d}l$ with a velocity $\mathrm{d}l/\mathrm{d}t$ is:

$$I(t) = -q \cdot \frac{\mathrm{d}l}{\mathrm{d}t} \cdot \left.\frac{\mathrm{d}E}{\mathrm{d}V}\right|_V, \tag{25}$$

where $\left.\frac{\mathrm{d}E}{\mathrm{d}V}\right|_V$ is "Gunn's weighting field", which is defined as the derivative of the electric field due to the bias voltage V applied at the sensing electrode. All other potentials are held constant during differentiation. If the electric field is constant, Eq. 25 converges to Eq. 24.

Despite being able to provide unique single-event information not available from broadbeam testing, IBIC suffers from several complications. The low beam flux means that many scans over the area of interest are required since the beam does not deposit a single ion for every step of the event window. The testing has to be done in a high vacuum. Scans are completed until a sufficient data cube is built up. Though the beam flux is low, the ions are confined to a small area, increasing the fluence (Φ) and the possibility of beam-induced damage [BGD93]. This damage comes in the form of displacements and the creation of vacancy-hole pairs, such as Frenkel defects. IBIC data are often collected in list-mode [BSS$^+$95] so that the data files can be read top-to-bottom in order of increasing fluence. If beam damage is present, the charge pulse

height is modulated. The systematically altered data can be identified and accounted for in subsequent analyses.

The devices under test cannot have electrostatic discharge protection diodes on the terminals being evaluated for IBIC. Furthermore, the device under test must be biased in such a way that the quiescent currents are small, which precludes active operation. Electrostatic protection, while convenient for handling devices, interferes with the IBIC signal since induced current cannot flow freely and because the diode decouples the electric field from the applied potential (*i.e.*, Eq. 25). Low quiescent currents are required because the device terminals are biased through charge-sensitive preamplifiers that contain a 50 or 100 MΩ resistor. Every 1 nA of leakage current drops 100 mV across a 100 MΩ resistor.

While reverse leakage current is not usually an issue for SiGe HBTs, damaged devices can leak through the base and collector, precluding measurement on those channels. This is strictly a DC current effect, but AC noise also matters. Analog-to-digital converters take the amplified and shaped voltage pulse and digitize it, which requires low- and high-level discriminators. If the discrimination window gets too small, valuable parts of the signal can be rejected. This is especially important for long-range charge induction from ion strikes outside the active region of the device under test.

REFERENCES

[AB78] R. C. Alig and S. Bloom. Secondary-electron-escape probabilities. *J. Appl. Phys.*, 49(6):3476–3480, Jun. 1978.

[AFS+97] D. C. Ahlgren, G. Freeman, S. Subbanna, R. Groves, J. Greenberg, J. Malinowski, D. Nguyen-Ngoc, S. J. Jeng, K. Stein, K. Schonenberg, D. Kiesling, B. Martin, S. Wu, D. L. Harame, and B. S. Meyerson. A SiGe HBT BiCMOS technology for mixed-signal RF applications. In *Bipolar/BiCMOS Circuits and Technology Meeting*, pages 195–198, Minneapolis, MN, 1997. IEEE.

[AMB+07] O. A. Amusan, L. W. Massengill, M. P. Baze, B. L. Bhuva, A. F. Witulski, S. DasGupta, A. L. Sternberg, P. R. Fleming, C. C. Heath, and M. L. Alles. Directional sensitivity of single event upsets in 90 nm cmos due to charge sharing. *IEEE Trans. Nucl. Sci.*, 54(6):2584–2589, Dec. 2007.

[AWM+06] O. A. Amusan, A. F. Witulski, L. W. Massengill, B. L. Bhuva, P. R. Fleming, M. L. Alles, A. L. Sternberg, J. D. Black, and R. D. Schrimpf. Charge collection and charge sharing in a 130 nm cmos technology. *IEEE Trans. Nucl. Sci.*, 53(6):3253–3258, Dec. 2006.

[Bar05] H. J. Barnaby. Total dose effects in modern integrated circuit technologies. In *Nuclear and Space Radiation Effects Conf. Short Course*, pages 1–112 Section III, Seattle, WA, 2005. IEEE.

[BB50] J. Bardeen and W. H. Brattain. Three-electrode circuit element utilizing semiconductive materials, 1950. US Patent 2,524,035, filed Jun. 17, 1948, and issued Oct. 10, 1950.

[BBM+86] T. Boggess, K. Bohnert, K. Mansour, S. Moss, I. Boyd, and A. Smirl. Simultaneous measurement of the two-photon coefficient and free-carrier cross section above the bandgap of crystalline silicon. *IEEE J. Quantum Electron.*, 22(2):360–368, Feb. 1986.

[BCV+95] J. A. Babcock, J. D. Cressler, L. S. Vempati, S. D. Clark, R. C. Jaeger, and D. L. Harame. Ionizing radiation tolerance of high-performance SiGe HBTs grown by UHV/CVD. *IEEE Trans. Nucl. Sci.*, 42(6):1558–1566, Dec. 1995.

[BGD93] M. B. H. Breese, G. W. Grime, and M. Dellith. The effect of ion induced damage on ibic images. *Nucl. Instr. and Meth. B.*, 77(1-4):332–338, May 1993.

[Bin88] D. Binder. Analytic seu rate calculation compared to space data. *IEEE Trans. Nucl. Sci.*, 35(6):1570–1572, Dec. 1988.

[BKK+93] S. Buchner, K. Kang, D. Krening, G. Lannan, and R. Scheiderwind. Dependence of the SEU window of vulnerability of a logic circuit on magnitude of deposited charge. *IEEE Trans. Nucl. Sci.*, 41(6):1853–1857, Dec. 1993.

[BMH58] R. Braunstein, A. R. Moore, and F. Herman. Intrinsic optical absorption in germanium-silicon alloys. *Phys. Rev.*, 109(3):695–710, Feb. 1958.

[BNC+99] G. Banerjee, G. Niu, J. D. Cressler, S. D. Clark, M. J. Palmer, and D. C. Ahlgren. Anomalous dose rate effects in gamma irradiated SiGe heterojunction bipolar transistors. *IEEE Trans. Nucl. Sci.*, 46(6):1620–1626, Dec. 1999.

[BSS+95] M. B. H. Breese, A. Saint, F. W. Sexton, K. M. Horn, H. Schöne, B. L. Doyle, J. S. Laird, and G. J. F. Legge. Optimization of ion-beam induced charge microscopy for the analysis of integrated circuits. *J. Appl. Phys.*, 77(8):3734–3741, Apr. 1995.

[BVVS07] M. B. H. Breese, E. Vittone, G. Vizkelethy, and P. J. Sellin. A review of ion beam induced charge microscopy. *Nucl. Instr. and Meth. B*, 264(2):345–360, Nov. 2007.

[BWW+06] D. R. Ball, K. M. Warren, R. A. Weller, R. A. Reed, A. S. Kobayashi, J. A. Pellish, M. H. Mendenhall, C. L. Howe, L. W. Massengill, R. D. Schrimpf, and N. F. Haddad. Simulating nuclear events in a TCAD model of a high-density SEU-hardened SRAM technology. *IEEE Trans. Nucl. Sci.*, 53(4):1794–1798, Aug. 2006.

[CHD+06] P. Chu, D. L. Hansen, B. L. Doyle, K. Jobe, R. Lopez-Aguado, M. Shoga, and D. S. Walsh. Ion-microbeam probe of high-speed shift registers for SEE analysis – part I: SiGe. *IEEE Trans. Nucl. Sci.*, 53(3):1574–1582, Jun. 2006.

[CHM+00] J. D. Cressler, M. C. Hamilton, G. S. Mullinax, Y. Li, G. Niu, C. J. Marshall, P. W. Marshall, H. S. Kim, M. J. Palmer, A. J. Joseph, and G. Freeman. The effects of proton irradiation on the lateral and vertical scaling of UHV/CVD SiGe HBT BiCMOS technology. *IEEE Trans. Nucl. Sci.*, 47(6):2515–2520, Dec. 2000.

[CKM+89] A. Campbell, A. Knudson, D. McMorrow, W. Anderson, J. Roussos, S. Espy, S. Buchner, K. Kang, D. Kerns, and S. Kerns. Ion induced charge collection in GaAs MESFETs. *IEEE Trans. Nucl. Sci.*, 36(6):2292–2299, Dec. 1989.

[CKS+06] J. P. Comeau, R. Krithivasan, A. K. Sutton, R. Diestelhorst, G. Espinel, A. P. Gnana Prakash, B. Jun, J. D. Cressler, M. Varadharajaperumal, G. Niu, J. A. Pellish, R. A. Reed, P. W. Marshall, and G. Vizkelethy. An investigation of transistor layout-based SEU hardening of SiGe HBTs. In *Proc. Radiation Effects on Components and Systems*, Athens, Greece, 2006. IEEE.

[CLP+08] M.-H. Cho, R. Lee, A.-S. Peng, D. Chen, C.-S. Yeh, and L.-K. Wu. Miniature RF test structure for on-wafer device testing and in-line process monitoring. *IEEE Trans. Electron Devices*, 55(1):462–465, Jan. 2008.

[CMM+97] M. A. Carts, P. W. Marshall, C. J. Marshall, K. A. LaBel, M. Flanegan, and J. Bretthauer. Single event test methodology and test results of commercial gigabit per second fiber channel hardware. *IEEE Trans. Nucl. Sci.*, 44(6):1878–1884, Dec. 1997.

[CN03] J. D. Cressler and G. Niu. *Silicon-Germanium Heterojunction Bipolar Transistors*. Artech House, Boston, MA, 2003.

[Cre98] J. D. Cressler. SiGe HBT technology: a new contender for Si-based RF and microwave circuit applications. *IEEE Trans. Microwave Theory Tech.*, 46(5):572–589, May 1998.

[Cre05] J. D. Cressler. On the potential of SiGe HBTs for extreme environment electronics. *Proc. IEEE*, 93(9):1559–1582, Sep. 2005.

[Cre06a] J. D. Cressler, editor. *The Silicon Heterostructure Handbook: materials, fabrication, devices, circuits, and applications of SiGe and Si strained-layer epitaxy*. CRC, Boca Raton, FL, 2006.

[Cre06b] J. D. Cressler, editor. *The Silicon Heterostructure Handbook: materials, fabrication, devices, circuits, and applications of SiGe and Si strained-layer epitaxy*, pages 782–792. CRC, Boca Raton, FL, 2006. Chapter title: Best Practice AC Measurement Techniques, By: R. A. Groves.

[Cre07] J. D. Cressler. SiGe BiCMOS technology: an IC design platform for extreme environment electronics applications. In 45th *Annu. Int. Reliability Physics Symp.*, pages 141–149, Phoenix, AZ, Apr. 2007. IEEE.

[DHWS92] B. L. Doyle, K. M. Horn, D. S. Walsh, and F. W. Sexton. Single event upset imaging with a nuclear microprobe. *Nucl. Instr. and Meth. B*, 64(1-4):313–320, Feb. 1992.

[Dod96] P. E. Dodd. Device simulation of charge collection and single-event upset. *IEEE Trans. Nucl. Sci.*, 43(3):561–565, Apr. 1996.

[Dod99] P. E. Dodd. Basic mechanisms for single-event effects. In *Nuclear and Space Radiation Effects Conf. Short Course*, pages 1–85 Section II, Norfolk, VA, 1999. IEEE.

[Ear52] J. M. Early. Effects of space-charge layer widening in junction transistors. *Proc. IRE*, 40(11):1401–1406, Nov. 1952.

[FCGM+02] V. Ferlet-Cavrois, G. Gasiot, C. Marcandella, C. D'Hose, O. Flament, O. Faynot, J. D. de Pontcharra, and C. Raynaud. Insights on the transient response of fully and partially depleted SOI technologies under heavy-ion and dose-rate irradiations. *IEEE Trans. Nucl. Sci.*, 49(6):2948–2956, Dec. 2002.

[FCPG+06] V. Ferlet-Cavrois, P. Paillet, M. Gaillardin, D. Lambert, J. Baggio, J. R. Schwank, G. Vizkelethy, M. R. Shaneyfelt, K. Hirose, E. W. Blackmore, O. Faynot, C. Jahan, and L. Tosti. Statistical analysis of the charge collected in SOI and bulk devices under heavy ion and proton irradiation – implications for digital SETs. *IEEE Trans. Nucl. Sci.*, 53(6):3242–3252, Dec. 2006.

[FCPM+05] V. Ferlet-Cavrois, P. Paillet, D. McMorrow, A. Torres, M. Gaillardin, J. S. Melinger, A. R. Knudson, A. B. Campbell, J. R. Schwank, G. Vizkelethy, M. R. Shaneyfelt, K. Hirose, O. Faynot, C. Jahan, and L. Tosti. Direct measurement of transient pulses induced by laser and heavy ion irradiation in deca-nanometer devices. *IEEE Trans. Nucl. Sci.*, 52(6):2104–2113, Dec. 2005.

[FCPM+06] V. Ferlet-Cavrois, R. Paillet, D. McMorrow, J. S. Melinger, A. B. Campbell, M. Gaillardin, O. Faynot, O. Thomas, G. Barna, and B. Giffard. Analysis of the transient response of high performance 50-nm partially depleted SOI transistors using a laser probing technique. *IEEE Trans. Nucl. Sci.*, 53(4):1825–1833, Aug. 2006.

[FIW04] G. Folger, V. N. Ivanchenko, and J. P. Wellisch. The binary cascade: nucleon nuclear reactions. *Eur. Phys. J. A*, 21(3):407–417, Sep. 2004.

[Fle85] L. D. Flesner. Gate charge collection and induced drain current in gaas fets. *IEEE Trans. Nucl. Sci.*, 32(6):4110–4114, Dec. 1985.

[GM31] M. Göppert-Mayer. Über Elementarakte mit zwei Quantensprüngen. *Ann. Phys.*, 401(3):273–294, 1931.

[GOSO84] R. M. Gilbert, G. K. Ovrebo, J. Schifano, and T. R. Oldham. Charge collection in n-type GaAs Schottky-barrier diodes struck by heavy energetic ions. *IEEE Trans. Nucl. Sci.*, 31(6):1570–1573, Dec. 1984.

[Gun64] J. B. Gunn. A general expression for electrostatic induction and its application to semiconductor devices. *Solid-State Electron.*, 7(10):739–742, Oct. 1964.

[HCJ+06] D. L. Hansen, P. Chu, K. Jobe, A. L. McKay, and H. P. Warren. SEU cross sections of hardened and unhardened SiGe circuits. *IEEE Trans. Nucl. Sci.*, 53(6):3579–3586, Dec. 2006.

[HDS92] K. M. Horn, B. L. Doyle, and F. W. Sexton. Nuclear microprobe imaging of single-event upsets. *IEEE Trans. Nucl. Sci.*, 39(1):7–12, Jan. 1992.

[HDS+93] K. M. Horn, B. L. Doyle, F. W. Sexton, J. S. Laird, A. Saint, M. Cholewa, and G. J. F. Legge. Ion beam induced charge collection (IBICC) microscopy of ICs: relation to single event upsets (SEU). *Nucl. Instr. and Meth. B*, 77(1-4):355–361, May 1993.

[Hec32] K. Hecht. Zum Mechanismus des lichtelektrischen Primärstromes in isolierenden Kristallen. *Z. Physik*, 77(3-4):235–245, Mar. 1932.

[HEF+89] S. J. Heileman, W. R. Eisenstadt, R. M. Fox, R. S. Wagner, N. Bordes, and J. M. Bradley. CMOS VLSI single event transient characterization. *IEEE Trans. Nucl. Sci.*, 36(6):2287–2291, Dec. 1989.

[HION01] T. Hirao, H. Itoh, S. Okada, and I. Nashiyama. Studies of single-event transient current induced in GaAs and Si diodes by energetic heavy ions. *Radiat. Phys. Chem.*, 60:269–272, Mar. 2001.

[HJWH92] B. Hughlock, A. Johnston, T. Williams, and J. Harrang. A comparison of charge collection effects between GaAs MESFETs and III-V HFETs. *IEEE Trans. Nucl. Sci.*, 39(6):1642–1646, Dec. 1992.

[HML+05] D. L. Hansen, P. W. Marshall, R. Lopez-Aguado, K. Jobe, M. A. Carts, C. J. Marshall, P. Chu, and S. F. Meyer. A study of the SEU performance of InP and SiGe shift registers. *IEEE Trans. Nucl. Sci.*, 52(4):1140–1147, Aug. 2005.

[HMO81a] C.-M. Hsieh, P. C. Murley, and R. R. O'Brien. Dynamics of charge collection from alpha-particle tracks in integrated circuits. In *Int. Reliability Physics Symp.*, volume 19, pages 38–42, Orlando, FL, Apr. 1981.

[HMO81b] C.-M. Hsieh, P. C. Murley, and R. R. O'Brien. A field-funneling effect on the collection of alpha-particle-generated carriers in silicon devices. *IEEE Electron Device Lett.*, EDL-2(4):103–105, Apr. 1981.

[HMO83] C.-M. Hsieh, P. C. Murley, and R. R. O'Brien. Collection of charge from alpha-particle tracks in silicon devices. *IEEE Trans. Electron Devices*, ED-30(6):686–693, Jun. 1983.

[How05] C. L. Howe. Radiation-Induced Energy Deposition and Single Event Upset Error Rates in Scaled Microelectronic Structures. Master's thesis, Vanderbilt University, Nashville, Tennessee USA, Nov. 2005.

[HPC+06] B. M. Haugerud, M. M. Pratapgarhwala, J. P. Comeau, A. K. Sutton, A. P. Gnana Prakash, J. D. Cressler, P. W. Marshall, C. J. Marshall, R. L. Ladbury, M. El-Diwany, C. Mitchell, L. Rockett, T. Bach, R. Lawrence, and N. Haddad. Proton and gamma radiation effects in a new first-generation SiGe HBT. *Solid-State Electron.*, 50(2):181–190, Feb. 2006.

[HS83] M. A. Hopkins and J. R. Srour. Measurements of alpha-particle-induced charge in GaAs devices. *IEEE Trans. Nucl. Sci.*, 30(6):4457–4463, Dec. 1983.

[HS84] M. A. Hopkins and J. R. Srour. Charge collection measurements on GaAs devices fabricated on semi-insulating substrates. *IEEE Trans. Nucl. Sci.*, 31(6):1116–1120, Dec. 1984.

[Hu82] C. Hu. Alpha-particle-induced field and enhanced collection of carriers. *IEEE Electron Device Lett.*, EDL-3(2):31–34, Feb. 1982.

[HWJP91] B. Hughlock, T. Williams, A. Johnston, and R Plaag. Ion induced charge collection in GaAs MESFETs and its effect on SEU vulnerability. *IEEE Trans. Nucl. Sci.*, 38(6):1442–1449, Dec. 1991.

[HWR+05] C. L. Howe, R. A. Weller, R. A. Reed, M. H. Mendenhall, R. D. Schrimpf, K. M. Warren, D. R. Ball, L. W. Massengill, K. A. LaBel, J. W. Howard, and N. F. Haddad. Role of heavy-ion nuclear reactions in determining on-orbit single event error rates. *IEEE Trans. Nucl. Sci.*, 52(6):2182–2188, Dec. 2005.

[IPD+87] S. S. Iyer, G. L. Patton, S. L. Delage, S. Tiwari, and J. M. C. Stork. Silicon-germanium base heterojunction bipolar transistors by molecular beam epitaxy. In *Tech. Dig. IEEE Int. Electron Devices Meeting*, pages 874–876, 1987.

[JG03] H. Johnson and M. Graham. *High-Speed Signal Propagation: Advanced Black Magic*. Prentice Hall, Upper Saddle River, NJ, 2003.

[JKP+02] B. Jagannathan, M. Khater, F. Pagette, J.-S. Rieh, D. Angell, H. Chen, J. Florkey, F. Golan, D. R. Greenberg, R. Groves, S. J. Jeng, J. Johnson, E. Mengistu, K. T. Schonenberg, C. M. Schnabel, P. Smith, A. Stricker, D. Ahlgren, G. Freeman, K. Stein, and S. Subbanna. Self-aligned SiGe NPN transistors with 285 GHz $f_{\max}$ and 207 GHz f_t in a manufacturable technology. *IEEE Electron Device Lett.*, 23(5):258–260, May 2002.

[JPF+08] P. Jaulent, V. Pouget, P. Fouillat, D. McMorrow, and F. Bezerra. SET sensitive volume imaging and measurement with two-photon absorption laser testing. In *Nuclear and Space Radiation Effects Conf.* IEEE, Jul. 2008. Paper A-10.

[KBW+05] A. S. Kobayashi, D. R. Ball, K. M. Warren, R. A. Reed, N. Haddad, M. H. Mendenhall, R. D. Schrimpf, and R. A. Weller. The effect of metallization layers on single event susceptibility. *IEEE Trans. Nucl. Sci.*, 52(6):2189–2193, Dec. 2005.

[KK84] R. Koga and W. A. Kolasinski. Heavy ion-induced single event upsets of microcircuits; a summary of the Aerospace Corporation test data. *IEEE Trans. Nucl. Sci.*, 31(6):1190–1195, Dec. 1984.

[Kle68] C. A. Klein. Bandgap dependence and related features of radiation ionization energies in semiconductors. *J. Appl. Phys.*, 39(4):2029–2038, Mar. 1968.

[KMN+06] R. Krithivasan, P. W. Marshall, M. Nayeem, A. K. Sutton, W.-M. Kuo, B. M. Haugerud, L. Najafizadeh, J. D. Cressler, M. A. Carts, C. J. Marshall, D. L. Hansen, K.-C. M. Jobe, A. L. McKay, G. Niu, R. Reed, B. A. Randall, C. A. Burfield, M. D. Lindberg, B. K. Gilbert, and E. S. Daniel. Application of

RHBD techniques to SEU hardening of third-generation SiGe HBT logic circuits. *IEEE Trans. Nucl. Sci.*, 53(6):3400–3407, Dec. 2006.

[KNC+03] R. Krithivasan, G. F. Niu, J. D. Cressler, S. M. Currie, K. E. Fritz, R. A. Reed, P. W. Marshall, P. A. Riggs, B. A. Randall, and B. Gilbert. An SEU hardening approach for high-speed SiGe HBT digital logic. *IEEE Trans. Nucl. Sci.*, 50(6):2126–2134, Dec. 2003.

[Kol00] T. E. Kolding. A four-step method for de-embedding gigahertz on-wafer CMOS measurements. *IEEE Trans. Electron Devices*, 47(4):734–740, Apr. 2000.

[Kro57a] H. Kroemer. Quasielectric and quasimagnetic fields in nonuniform semiconductors. *RCA Review*, 18:332–342, 1957.

[Kro57b] H. Kroemer. Theory of a wide-gap emitter for transistors. *Proc. IRE*, 45(11):1535–1537, Nov. 1957.

[Lac03] R. Lacoe. CMOS scaling, design principles and hardening-by-design methodologies. In *Nuclear and Space Radiation Effects Conf. Short Course*, pages 1–142 Section II, Monterey, CA, 2003. IEEE.

[LCS+08] J. S. Laird, Y. Chen, L. Scheick, T. Vo, and A. Johnston. Scanning picosecond tunable laser system for simulating MeV heavy ion-induced charge collection events as a function of temperature. *Rev. Sci. Instrum.*, 79(083705), Aug. 2008.

[LHO+02] J. S. Laird, T. Hirao, S. Onoda, H. Mori, and H. Itoh. Temperature dependence of heavy ion-induced current transients in si epilayer devices. *IEEE Trans. Nucl. Sci.*, 49(3):1389–1395, Jun. 2002.

[LHO+05] J. S. Laird, T. Hirao, S. Onoda, T. Wakasa, T. Yamakawa, H. Abe, and T. Kamiya. Investigating radiation effects on high-speed optoelectronic devices by combining time-resolved laser and ion microbeam studies. *Nucl. Instr. and Meth. B*, 231(1-4):476–481, Apr. 2005.

[LHOI05] J. S. Laird, T. Hirao, S. Onoda, and H. Itoh. High-injection carrier dynamics generated by mev heavy ions impacting high-speed photodetectors. *J. Appl. Phys.*, 98(1):013530, Jul. 2005.

[LMM07] W. T. Lotshaw, D. McMorrow, and J. S. Melinger. Measurement of nonlinear absorption and refraction in doped Si below the band edge. In *Nonlinear Optics: Materials, Fundamentals, and Applications*. OSA, 2007.

[LSV+07] J. S. Laird, L. Scheick, G. Vizkelethy, M. M. Mojarradi, T. Miyahira, Y. Chen, B. Blalock, R. Greenwell, S. Terry, and B. Doyle. Single event transient analysis of an SOI operational amplifier for use in low-temperature Martian exploration. *Nucl. Instr. and Meth. B*, 260(1):281–287, Jul. 2007.

[Mas54] S. J. Mason. Power gain in feedback amplifier. *IRE Trans. Circuit Theory*, 1(2):20–25, Jun. 1954.

[MBK+04] D. McMorrow, J. B. Boos, A. R. Knudson, W. T. Lotshaw, D. Park, J. S. Melinger, B. R. Bennett, A. Torres, V. Ferlet-Cavrois, J. E. Sauvestre, C. D'Hose, and O. Flament. Transient response of III-V field-effect transistors to heavy-ion irradiation. *IEEE Trans. Nucl. Sci.*, 51(6):3324–3331, Dec. 2004.

[MBM+94] J. S. Melinger, S. Buchner, D. McMorrow, W. J. Stapor, T. R. Weatherford, A. B. Campbell, and H. Eisen. Critical evaluation of pulsed laser method for single-event effects testing and fundamental studies. *IEEE Trans. Nucl. Sci.*, 41(6):2574–2584, Dec. 1994.

[MBM+07] D. McMorrow, J. Brad Boos, J. S. Melinger, V. Ferlet-Cavrois, P. Paillet, O. Duhamel, and J. Baggio. Measurement of the transient response of semiconductor devices to ionizing radiation. *Nucl. Instr. and Meth. B*, 261(1-2):1137–1141, Aug. 2007.

[MCC+00] P. W. Marshall, M. A. Carts, A. Campbell, D. McMorrow, S. Buchner, R. Stewart, B. Randall, B. Gilbert, and R. A. Reed. Single event effects in circuit-hardened SiGe HBT logic at gigabit per second data rates. *IEEE Trans. Nucl. Sci.*, 47(6):2669–2674, Dec. 2000.

[MCC+04] P. W. Marshall, M. Carts, A. Campbell, R. Ladbury, R. Reed, C. Marshall, S. Currie, D. McMorrow, S. Buchner, C. Seidleck, P. Riggs, K. Fritz, B. Randall, and B. Gilbert. A comparative study of heavy-ion and proton-induced bit-error sensitivity and complex burst-error modes in commercially available high-speed SiGe BiCMOS. *IEEE Trans. Nucl. Sci.*, 51(6):3457–3463, Dec. 2004.

[MCC+05] P. W. Marshall, M. Carts, S. M. Currie, R. A. Reed, B. Randall, K. Fritz, K. Kennedy, M. Berg, R. Krithivasan, and C. Siedleck. Autonomous bit error rate testing at multi-gbit/s rates implemented in a 5AM SiGe circuit for radiation effects self test (CREST). *IEEE Trans. Nucl. Sci.*, 52(6):2446–2454, Dec. 2005.

[MDW+95] P. W. Marshall, C. J. Dale, T. R. Weatherford, M. La Macchia, and K. A. LaBel. Particle-induced mitigation of SEU sensitivity in high data rate GaAs HIGFET technologies. *IEEE Trans. Nucl. Sci.*, 42(6):1844–1851, Dec. 1995.

[Mey86] B. S. Meyerson. Low temperature silicon epitaxy by ultra-high vacuum/chemical vapor deposition. *Appl. Phys. Lett.*, 48(12):797–799, Mar. 1986.

[MFCA+06] D. Munteanu, V. Ferlet-Cavrois, J. L. Autran, P. Paillet, J. Baggio, O. Faynot, C. Jahan, and L. Tosti. Investigation of quantum effects in ultra-thin body

single- and double-gate devices submitted to heavy ion irradiation. *IEEE Trans. Nucl. Sci.*, 53(6):3363–3371, Dec. 2006.

[MLM+02] D. McMorrow, W. T. Lotshaw, J. S. Melinger, S. Buchner, and R. L. Pease. Subbandgap laser-induced single event effects: carrier generation via two-photon absorption. *IEEE Trans. Nucl. Sci.*, 49(6):3002–3008, Dec. 2002.

[MMB+00] D. McMorrow, J. S. Melinger, S. Buchner, T. Scott, R. D. Brown, and N. F. Haddad. Application of a pulsed laser for evaluation and optimization of SEU-hard designs. *IEEE Trans. Nucl. Sci.*, 47(3):559–565, Jun. 2000.

[MMQR59] G. G. MacFarlane, T. P. McLean, J. E. Quarrington, and V. Roberts. Exciton and phonon effects in the absorption spectra of germanium and silicon. *J. Phys. Chem. Solids*, 8(1):388–392, Jan. 1959.

[MO82] F. B. McLean and T. R. Oldham. Charge funneling in N- and P-type Si substrates. *IEEE Trans. Nucl. Sci.*, 29(6):2018–2023, Dec. 1982.

[MRP+08] E. J. Montes, R. A. Reed, J. A. Pellish, M. L. Alles, R. D. Schrimpf, R. A. Weller, M. Varadharajaperumal, G. Niu, A. K. Sutton, R. Diestelhorst, G. Espinel, R. Krithivasan, J. P. Comeau, J. D. Cressler, P. W. Marshall, and G. Vizkelethy. Single event upset mechanisms for low-energy deposition events in SiGe HBTs. *IEEE Trans. Nucl. Sci.*, 55(3):1581–1586, Jun. 2008.

[MW91] M. H. Mendenhall and R. A. Weller. Algorithms for the rapid computation of classical cross sections for screened Coulomb collisions. *Nucl. Instr. and Meth. B*, 58(1):11–17, May 1991.

[MW05] M. H. Mendenhall and R. A. Weller. An algorithm for computing screened Coulomb scattering in GEANT4. *Nucl. Instr. and Meth. B*, 227(3):420–430, Jan. 2005.

[MWB+96] D. McMorrow, T. Weatherford, S. Buchner, A. Knudson, J. Melinger, and L. Tran. Single-event phenomena in GaAs devices and circuits. *IEEE Trans. Nucl. Sci.*, 43(2):628–644, Apr. 1996.

[MWK+93] D. McMorrow, T. Weatherford, A. R. Knudson, L. H. Tran, J. S. Melinger, and A. B. Campbell. Single-event dynamics of high-performance HBTs and GaAs MESFETs. *IEEE Trans. Nucl. Sci.*, 40(6):1858–1866, Dec. 1993.

[MWK+96] D. McMorrow, T. R. Weatherford, A. R. Knudson, S. Buchner, J. S. Melinger, L. H. Tran, A. B. Campbell, P. W. Marshall, C. J. Dale, A. Peczalski, and S. Baier. Charge collection characteristics of GaAs heterostructure FETs fabricated with a low-temperature grown GaAs buffer layer. *IEEE Trans. Nucl. Sci.*, 43(3):918–923, Jun. 1996.

[NBC+98] G. F. Niu, G. Banerjee, J. D. Cressler, J. Rolden, and S. D. Clark. Electrical probing of surface and bulk traps in proton-irradiated gate-assisted lateral PNP transistors. *IEEE Trans. Nucl. Sci.*, 45(6):2361–2365, Dec. 1998.

[NCS+00] G. Niu, J. D. Cressler, M. Shoga, K. Jobe, P. Chu, and D. L. Harame. Simulation of SEE-induced charge collection in UHV/CVD SiGe HBTs. *IEEE Trans. Nucl. Sci.*, 47(6):2682–2689, Dec. 2000.

[NCZ+99] G. Niu, J. D. Cressler, S. Zhang, U. Gogineni, and D. C. Ahlgren. Measurement of collector-base junction avalanche multiplication effects in advanced UHV/CVD SiGe HBTs. *IEEE Trans. Electron Devices*, 46(5):1007–1015, May 1999.

[NHM+95] D. Nguyen-Ngoc, D. L. Harame, J. C. Malinowski, S. J. Jeng, K. T. Schonenberg, M. M. Gilbert, G. D. Berg, S. Wu, M. Soyuer, K. A. Tallman, K. J. Stein, R. A. Groves, S. Subbanna, D. B. Colavito, D. A. Sunderland, and B. S. Meyerson. A 200 mm SiGe-HBT BiCMOS technology for mixed signal applications. In *Bipolar/BiCMOS Circuits and Technology Meeting*, pages 89–92, Minneapolis, MN, 1995. IEEE.

[NKC+01] G. Niu, R. Krithivasan, J. D. Cressler, P. Marshall, C. Marshall, R. Reed, and D. L. Harame. Modeling of single-event effects in circuit-hardened high-speed SiGe HBT logic. *IEEE Trans. Nucl. Sci.*, 48(6):1849–1854, Dec. 2001.

[NKC+02] G. Niu, R. Krithivasan, J. D. Cressler, P. A. Riggs, B. A. Randall, P. W. Marshall, R. A. Reed, and B. Gilbert. A comparison of SEU tolerance in high-speed SiGe HBT digital logic designed with multiple circuit architectures. *IEEE Trans. Nucl. Sci.*, 49(6):3107–3114, Dec. 2002.

[OHL+05] S. Onoda, T. Hirao, J. S. Laird, T. Okamoto, Y. Koizumi, and T. Kamiya. Analysis of transient ion beam induced current in Si PIN photodiode. *Nucl. Instr. and Meth. B*, 231(1-4):497–501, Apr. 2005.

[OL99] C. Odegard and C. Lambert. Comparative TDR analysis as a packaging FA tool. In *Proc. Int. Symp. Testing and Failure Analysis*, Santa Clara, CA, Nov. 1999.

[PCM+90] G. L. Patton, J. H. Comfort, B. S. Meyerson, E. F. Crabbé, G. J. Scilla, E. de Frésart, J. M. C. Stork, J. Y.-C. Sun, D. L. Harame, and J. Burghartz. 75 GHz f_T SiGe base heterojunction bipolar transistors. *IEEE Electron Device Lett.*, 11(4):171–173, Apr. 1990.

[Pea06] R. L. Pease. RHBD analog/mixed-signal devices and circuits. Technical report, RLP Reasearch, Inc. for ATK-Mission Research, Albuquerque, New Mexico USA, Mar. 2006. Under contract FA9453-04-C-0208, Subcontract SC-0208-04-0400.

[Pel06] J. A. Pellish. Substrate Engineering Techniques to Mitigate Radiation-Induced Charge Collection in Silicon-Germanium Heterojunction Bipolar Transistors. Master's thesis, Vanderbilt University, Nashville, Tennessee USA, Mar. 2006.

[Peo86] R. People. Physics and applications of Ge_xSi_{1-x}/Si strained-layer heterostructures. *IEEE J. Quantum Electron.*, 22(9):1696–1710, Sep. 1986.

[Pet95] E. L. Petersen. SEE rate calculations using the effective flux approach and a generalized figure of merit approximation. *IEEE Trans. Nucl. Sci.*, 42(6):1995–2003, Dec. 1995.

[Pet08] E. L. Petersen. Soft error results analysis and error rate prediction. In *Nuclear and Space Radiation Effects Conf. Short Course*, pages 1–303 Section III, Tucson, AZ, 2008. IEEE.

[PFL+00] V. Pouget, P. Fouillat, D. Lewis, H. Lapuyade, L. Sarger, F. M. Roche, S. Duzellier, and R. Ecoffet. An overview of the applications of a pulsed laser system for SEU testing. In *Proc. Int. On-Line Testing Workshop*, pages 52–57. IEEE, Jul. 2000.

[PFL07] V. Pouget, P. Fouillat, and D. Lewis. Using the seem software for laser set testing and analysis. In R. Velazco, P. Fouillat, and D. Lewis, editors, *Radiation Effects on Embedded Systems*, pages 259–268. Springer, Netherlands, 2007.

[Poz05] D. M. Pozar. *Microwave Engineering*. John Wiley and Sons, Hoboken, NJ, 3rd edition, 2005.

[PPAS92] E. L. Petersen, J. C. Pickel, J. H. Adams Jr., and E. C. Smith. Rate prediction for single event effects – a critique. *IEEE Trans. Nucl. Sci.*, 39(6):1577–1599, Dec. 1992.

[PPM+05] E. L. Petersen, V. Pouget, L. W. Massengill, S. P. Buchner, and D. McMorrow. Rate predictions for single-event effects – critique II. *IEEE Trans. Nucl. Sci.*, 52(6):2158–2167, Dec. 2005.

[PPS+93] E. L. Petersen, J. C. Pickel, E. C. Smith, P. J. Rudeck, and J. R. Letaw. Geometrical factors in SEE rate calculations. *IEEE Trans. Nucl. Sci.*, 40(6):1888–1909, Dec. 1993.

[PRM+08] J. A. Pellish, R. A. Reed, D. McMorrow, J. S. Melinger, P. Jenkins, A. K. Sutton, R. M. Diestelhorst, S. D. Phillips, J. D. Cressler, V Pouget, N. D. Pate, J. A. Kozub, R. A. Weller, R. D. Schrimpf, P. W. Marshall, A. D. Tipton, and G. Niu. Laser-induced current transients in SiGe HBTs. *IEEE Trans. Nucl. Sci.*, 55(6), Dec. 2008.

[PRS+06] J. A. Pellish, R. A. Reed, R. D. Schrimpf, M. L. Alles, M. Varadharajaperumal, G. Niu, A. K. Sutton, R. Diestelhorst, G. Espinel, R. Krithivasan, J. P. Comeau, J. D. Cressler, G. Vizkelethy, P. W. Marshall, R. A. Weller, M. H. Mendenhall, and E. J. Montes. Substrate engineering concepts to mitigate charge collection in deep trench isolation technologies. *IEEE Trans. Nucl. Sci.*, 53(6):3298–3305, Dec. 2006.

[PRS+07] J. A. Pellish, R. A. Reed, A. K. Sutton, R. A. Weller, M. A. Carts, P. W. Marshall, C. J. Marshall, R. Krithivasan, J. D. Cressler, M. H. Mendenhall, R. D. Schrimpf, K. M. Warren, B. D. Sierawski, and G. F. Niu. A generalized SiGe HBT single-event effects model for on-orbit event rate calculations. *IEEE Trans. Nucl. Sci.*, 54(6):2322–2329, Dec. 2007.

[PS91] E. J. Prinz and J. C. Sturm. Current gain-Early voltage products in heterojunction bipolar transistors with nonuniform base bandgaps. *IEEE Electron Device Lett.*, 12(12):661–663, Dec. 1991.

[Pyt] Python. Python Programming Language. `http://www.python.org/`.

[RAC+97] J. M. Roldan, W. E. Ansley, J. D. Cressler, S. D. Clark, and D. Nguyen-Ngoc. Neutron radiation tolerance of advanced UHV/CVD SiGe HBT BiCMOS technology. *IEEE Trans. Nucl. Sci.*, 44(6):1965–1973, Dec. 1997.

[Ram39] S. Ramo. Currents induced by electron motion. *Proc. IRE*, 27(9):584–585, Sep. 1939.

[RCM+96] R. A. Reed, M. A. Carts, P. W. Marshall, C. J. Marshall, S. Buchner, M. La Macchia, B. Mathes, and D. McMorrow. Single event upset cross sections at various data rates. *IEEE Trans. Nucl. Sci.*, 43(6):2862–2869, Dec. 1996.

[RK05] M. Racanelli and P. Kempf. SiGe BiCMOS technology for RF circuit applications. *IEEE Trans. Electron Devices*, 52(7):1259–1270, Jul. 2005.

[RKP+03] R. A. Reed, J. Kinnison, J. C. Pickel, S. Buchner, P. W. Marshall, S. Kniffin, and K. A. LaBel. Single-event effects ground testing and on-orbit rate prediction methods: the past, present, and future. *IEEE Trans. Nucl. Sci.*, 50(3):622–634, Jun. 2003.

[RMP+03] R. A. Reed, P. W. Marshall, J. C. Pickel, M. A. Carts, B. Fodness, G. F. Niu, K. Fritz, G. Vizkelethy, P. E. Dodd, T. Irwin, J. D. Cressler, R. Krithivasan, P. Riggs, J. Prairie, B. Randall, B. Gilbert, and K. A. LaBel. Heavy-ion broad-beam and microprobe studies of single-event upsets in 0.20 μm SiGe heterojunction bipolar transistors and circuits. *IEEE Trans. Nucl. Sci.*, 50(6):2184–2190, Dec. 2003.

[RNA+98] J. M. Roldan, G. Niu, W. E. Ansley, J. D. Cressler, S. D. Clark, and D. C. Ahlgren. An investigation of the spatial location of proton-induced traps in SiGe HBTs. *IEEE Trans. Nucl. Sci.*, 45(6):2424–2429, Dec. 1998.

[RVP+07] R. A. Reed, G. Vizkelethy, J. A. Pellish, B. D. Sierawski, K. M. Warren, M. Porter, J. Wilkinson, P. W. Marshall, G. Niu, J. D. Cressler, R. D. Schrimpf, A. D. Tipton, and R. A. Weller. Applications of heavy ion microprobe for single event effects analysis. *Nucl. Instr. and Meth. B*, 261(1-2):443–446, Aug. 2007.

[RWM+07] R. A. Reed, R. A. Weller, M. H. Mendenhall, J.-M. Lauenstein, K. M. Warren, J. A. Pellish, R. D. Schrimpf, B. D. Sierawski, L. W. Massengill, P. E. Dodd, N. F. Haddad, R. K. Lawrence, J. H. Bowman, and R. Conde. Impact of ion energy and species on single event effects analysis. *IEEE Trans. Nucl. Sci.*, 54(6), Dec. 2007.

[RWS+06] R. A. Reed, R. A. Weller, R. D. Schrimpf, M. H. Mendenhall, K. M. Warren, and L. W. Massengill. Implications of nuclear reactions for single event effects test methods and analysis. *IEEE Trans. Nucl. Sci.*, 53(6):3356–3362, Dec. 2006.

[SBC+07] A. K. Sutton, M. Bellini, J. D. Cressler, J. A. Pellish, R. A. Reed, P. W. Marshall, G. Niu, G. Vizkelethy, M. Turowski, and A. Raman. An evaluation of transistor-layout RHBD techniques for SEE mitigation in SiGe HBTs. *IEEE Trans. Nucl. Sci.*, 54(6):2044–2052, Dec. 2007.

[Sch81] P. E. Schmid. Optical absorption in heavily doped silicon. *Phys. Rev. B*, 23(10):5531–5536, May 1981.

[SF04] R. D. Schrimpf and D. M. Fleetwood, editors. *Radiation Effects and Soft Errors in Integrated Circuits and Electronic Devices*. World Scientific, 2004.

[SGJ+06] A. K. Sutton, A. P. Gnana Prakash, B. Jun, E. Zhao, M. Bellini, J. Pellish, R. M. Diestelhorst, M. A. Carts, A. Phan, R. Ladbury, J. D. Cressler, P. W. Marshall, C. J. Marshal, R. A. Reed, R. D. Schrimpf, and D. M. Fleetwood. An investigation of dose rate and source dependent effects in 200 GHz SiGe HBTs. *IEEE Trans. Nucl. Sci.*, 53(6):3166–3174, Dec. 2006.

[SHL+04] A. K. Sutton, B. M. Haugerud, Y. Lu, W. M. L. Kuo, J. D. Cressler, P. W. Marshall, R. A. Reed, J. S. Rieh, G. Freeman, and D. Ahlgren. Proton tolerance of fourth-generation 350 GHz UHV/CVD SiGe HBTs. *IEEE Trans. Nucl. Sci.*, 51(6):3736–3742, Dec. 2004.

[Sho38] W. Shockley. Currents to conductors induced by a moving point charge. *J. Appl. Phys.*, 9(10):635–636, Oct. 1938.

[Sho50] W. Shockley. Semiconductor amplifier, 1950. US Patent 2,502,488, filed Sep. 24, 1948, and issued Apr. 4, 1950.

[Sho51] W. Shockley. Circuit element utilizing semiconductive material, 1951. US Patent 2,569,347, filed Jun. 26, 1948, and issued Sep. 25, 1951.

[SKM+06] A. K. Sutton, R. Krithivasan, P. W. Marshall, M. A. Carts, C. Siedleck, R. Ladbury, J. D. Cressler, C. J. Marshall, S. Currie, R. A. Reed, G. Niu, B. Randall, K. Fritz, D. McMorrow, and B. Gilbert. SEU error signature analysis of Gbit/s SiGe logic circuits using a pulsed laser microprobe. *IEEE Trans. Nucl. Sci.*, 53(6):3277–3284, Dec. 2006.

[SMD+85] Z. Shanfield, M. M. Moriwaki, W. M. Digby, J. R. Srour, and D. E. Campbell. Characteristics of SEU current transients and collected charge in GaAs and Si devices. *IEEE Trans. Nucl. Sci.*, 32(6):4104–4109, Dec. 1985.

[SSH+91] M. Sheik-Bahae, A. A. Said, D. J. Hagan, M. J. Soileau, and E. W. Van-Stryland. Nonlinear refraction and optical limiting in thick media. *Opt. Eng.*, 30(1):1228–1235, Aug. 1991.

[Sum92] G. P. Summers. Displacement damage: mechanisms and measurements. In *Nuclear and Space Radiation Effects Conf. Short Course*, pages 1–58 Section IV, New Orleans, LA, 1992. IEEE.

[SWS+98] H. Schöne, D. S. Walsh, F. W. Sexton, B. L. Doyle, P. E. Dodd, J. F. Aurand, R. S. Flores, and N. Wing. Time-resolved ion beam induced charge collection (TRIBICC) in micro-electronics. *IEEE Trans. Nucl. Sci.*, 45(6):2544–2549, Dec. 1998.

[SWS+99] H. Schöne, D. S. Walsh, F. W. Sexton, B. L. Doyle, P. E. Dodd, J. F. Aurand, and N. Wing. Time-resolved ion beam induced charge collection (TRIBICC) in micro-electronics. *Nucl. Instr. and Meth. B*, 158(1-4):424–431, Sep. 1999.

[TAJB+97a] A. J. Tylka, J. H. Adams Jr, P. R. Boberg, B. Brownstein, W. F. Dietrich, E. O. Flueckiger, E. L. Petersen, M. A. Shea, D. F. Smart, and E. C. Smith. Creme96, 1997. Online: `https://creme96.nrl.navy.mil/`.

[TAJB+97b] A. J. Tylka, J. H. Adams Jr, P. R. Boberg, B. Brownstein, W. F. Dietrich, E. O. Flueckiger, E. L. Petersen, M. A. Shea, D. F. Smart, and E. C. Smith. CREME96: a revision of the Cosmic Ray Effects on Micro-Electronics Code. *IEEE Trans. Nucl. Sci.*, 44(6):2150–2160, Dec. 1997.

[TR07] M. Turowski and A. Raman. Improved mixed-mode simulation tools for radiation hardening of nanoscale semiconductor integrated circuits. Technical report, CFD Research Corp., Huntsville, Alabama USA, Jun. 2007. DTRA SBIR Phase II, Contract No. HDTRA1-07-C-0037.

[Tre89] R. L. Treadway. DC analysis of current mode logic. *IEEE Circuits Devices Mag.*, 5(2):21–35, Mar. 1989.

[VDP+05] G. Vizkelethy, B. L. Doyle, D. K. Price, P. E. Dodd, M. R. Shaneyfelt, and J. R. Schwank. Radiation effects microscopy for failure analysis of microelectronic devices. *Nucl. Instr. and Meth. B*, 231(1-4):467–475, Apr. 2005.

[VLT99] N. Van Vonno, R. Lucas, and D. Thornberry. Total dose hardness of a commercial SiGe BiCMOS technology. In *Proc.* 5th *European Conf. on Radiation and its Effects on Components and Systems*, pages K21–K22, Abbaye de Fontevraud, France, Sep. 1999.

[VNK+03] M. Varadharajaperumal, G. F. Niu, R. Krithivasan, J. D. Cressler, R. A. Reed, P. W. Marshall, G. Vizkelethy, P. E. Dodd, and A. J. Joseph. 3-D simulation of heavy-ion induced charge collection in SiGe HBTs. *IEEE Trans. Nucl. Sci.*, 50(6):2191–2198, Dec. 2003.

[VRMP07] G. Vizkelethy, R. A. Reed, P. W. Marshall, and J. A. Pellish. Ion beam induced charge (IBIC) studies of silicon germanium heterojunction bipolar transistors (HBTs). *Nucl. Instr. and Meth. B*, 260(1):264–269, Jul. 2007.

[VVW+85] E. W. Van Stryland, H. Vanherzeele, M. A. Woodall, M. J. Soileau, A. L. Smirl, S. Guha, and T. F. Boggess. Two photon absorption, non-linear refraction and optical limiting. *Opt. Eng.*, 24(4):613–623, Jul./Aug. 1985.

[WBB+87] R. S. Wagner, J. M. Bradley, N. Bordes, C. J. Maggiore, D. N. Sinha, and R. B. Hammond. Transient measurements of ultrafast charge collection in semiconductor diodes. *IEEE Trans. Nucl. Sci.*, 34(6):1240–1245, Dec. 1987.

[WBB+88] R. S. Wagner, N. Bordes, J. M. Bradley, C. J. Maggiore, A. R. Knudson, and A. B. Campbell. Alpha-, boron-, silicon- and iron- ion-induced current transients in low-capacitance silicon GaAs diodes. *IEEE Trans. Nucl. Sci.*, 35(6):1578–1584, Dec. 1988.

[WBM+86] R. S. Wagner, J. M. Bradley, C. J. Maggiore, J. G. Beery, and R. B. Hammond. An approach to measure ultrafast-funneling-current transients. *IEEE Trans. Nucl. Sci.*, 33(6):1651–1655, Dec. 1986.

[Wil90] G. R. Wilson. Advances in bipolar VLSI. *Proc. IEEE*, 78(11):1707–1719, Nov. 1990.

[WSW+07] K. M. Warren, B. D. Sierawski, R. A. Weller, R. A. Reed, M. H. Mendenhall, J. A. Pellish, and R. D. Schrimpf. Predicting thermal neutron induced soft errors in static memories using TCAD and physics-based Monte-Carlo simulation tools. *IEEE Electron Device Lett.*, 28(2):180–182, Feb. 2007.

[WWM+05] K. M. Warren, R. A. Weller, M. H. Mendenhall, R. A. Reed, D. R. Ball, C. L. Howe, B. D. Olson, M. L. Alles, L. W. Massengill, R. D. Schrimpf, N. F. Haddad, S. E. Doyle, D. McMorrow, J. S. Melinger, and W. T. Lotshaw. The contribution of nuclear reactions to heavy ion single event upset cross-section measurements in a high-density SEU hardened SRAM. *IEEE Trans. Nucl. Sci.*, 52(6):2125–2131, Dec. 2005.

[WWS+07] K. M. Warren, R. A. Weller, B. D. Sierawski, R. A. Reed, M. H. Mendenhall, R. D. Schrimpf, L. W. Massengill, M. Porter, J. Wilkinson, K. A. LaBel, and J. H. Adams Jr. Application of radsafe to model single event upset response of 0.25 μm CMOS SRAM. *IEEE Trans. Nucl. Sci.*, 54(4):898–903, Aug. 2007.

[Yar75] A. Yariv. *Quantum Electronics*. John Wiley and Sons, New York, NY, 1975.

[ZB08] J. F. Zeigler and J. P. Biersack. Stopping and range of ions in matter, 2008. Online: `http://www.srim.org/`.

[ZBL85] J. F. Zeigler, J. P. Biersack, and U. Littmark. *The Stopping and Range of Ions in Solids*. Pergamon, New York, 1985.

[Zei04] J. F. Zeigler. SRIM-2003. *Nucl. Instr. and Meth. B*, 219-220:1027–1036, Jun. 2004.

[ZNC+99] S. Zhang, G. Niu, J. D. Cressler, S. D. Clark, and D. C. Ahlgren. The effects of proton irradiation on the RF performance of SiGe HBTs. *IEEE Trans. Nucl. Sci.*, 46(6):1716–1721, Dec. 1999.